



Università degli Studi di Catania
Dipartimento di Scienze Chimiche

PhD Course in Materials Science and Nanotechnology
XXXV cycle

Metal nanoparticle decoration of nanostructures

Luca Bruno

Tutors:
Prof. S. Mirabella
Prof. F. Priolo

Academic Year 2021-2022

To my mom

Cover

Plan-view SEM image of Au nanoparticle decorated Ni-based nanowalls obtained by chemical bath deposition method. More details can be found within the Contents of this thesis.

Printed in Catania, 2022

*The Road goes ever on and on,
Down from the door where it began.
Now far ahead the Road has gone,
And I must follow, if I can,
Pursuing it with eager feet,
Until it joins some larger way
Where many paths and errands meet.
And whither then? I cannot say.*

*(J.R.R. Tolkien, *The Lord of the Rings*)*

Contents

Preface	1
CHAPTER 1: Metal nanoparticles: properties, interaction, and applications	3
There's plenty of Room at the Bottom	5
Nanostructures: basic properties	7
Metal nanoparticles	12
Importance of metal nanoparticles		12
Impact of nanoparticle–support interaction		12
Bimetallic nanoparticles	14
Structural features of bimetallic nanoparticles		14
Electronic Properties and Catalytic Activity of Bimetallic nanoparticles		16

Applications of metal nanoparticles	. . .	21
Conclusion	23
References		24

CHAPTER 2: Synthesis of mono- and bi-metallic

nanoparticles	33
Chemical reduction of noble metal nanoparticles		35
Au nanoparticles synthesis with trisodium citrate		35
Au, Pd and Pt monometallic nanoparticles with ascorbic acid		37
Au@Pd (core@shell) bimetallic nanoparticles		40
Conclusions	42
References	43

CHAPTER 3: Localized energy band bending in Au

decorated ZnO nanorods	45
Au nanoparticle decoration of ZnO nanorods	. . .	47
Materials and Methods	49
Synthesis and decoration of ZnO nanorods		49
Characterization		49
Materials characterization	50

Photoluminescence and Cathodoluminescence	52
Mott-Schottky analysis	57
Modeling the Au NP decoration effect	58
Conclusions	61
References	62

CHAPTER 4: Bare and Pt decorated NiO

microflowers for overall water splitting	71
---	-----------

Part 1: Enhanced Electrocatalytic Activity of low cost NiO Microflowers on Graphene Paper for

Oxygen Evolution Reaction	74
----------------------------------	-----------

Experimental	76
---------------------	-----------

Synthesis of NiO microflowers	76
-------------------------------	----

Preparation of the electrode	76
------------------------------	----

Characterization of NiO microflowers on graphene paper	77
--	----

electrodes

Materials Characterization	78
-----------------------------------	-----------

Electrochemical characterization – OER	80
---	-----------

OER performance evaluation	84
-----------------------------------	-----------

Part 2: Physical Insights into Alkaline overall water splitting with NiO Microflowers Electrodes with ultra-low amount of Pt catalyst 91

Experimental 93

Preparation of the electrode **93**

Characterization of Pt decorated NiO microflowers **94**

Morphological and elemental characterization 95

Electrochemical characterization – HER . . . 97

Overall water splitting 105

Conclusions 106

References 107

CHAPTER 5: Enlightening the Bimetallic Effect of Au@Pd nanoparticles on Ni oxide nanostructures . 119

Bimetallic nanoparticle decoration 121

Methods 123

Colloidal Au, Pd, and Au@Pd dispersion **123**

Decorate Ni oxide electrode (NOE) **123**

Analytical Techniques **123**

Morphological and elemental characterization . 125

Electrochemical modification and characterization . 126

Modeling the bimetallic decoration effect	130
Glucose and H₂O₂ sensing test	136
Conclusions	139
References	140
CONCLUSIONS	151
Appendix A	153
Appendix B	157
Appendix C	161
Curriculum Vitae	165
List of Publications	169

This Page Intentionally Left Blank

Preface

The design, fabrication and application of nanostructures or nanomaterials cannot leave aside the fundamental understanding of the relationships between physical properties or phenomena and materials size.

Nanotechnology deals with materials or structures in nanometer scales, typically ranging from sub-nanometers to several hundred nanometers. On nanometer scale, materials and structures possess new physical properties and exhibit new physical phenomena. Some of these properties are already known (for example, band gaps of semiconductors can be tuned by varying materials size). There may be many more properties not yet known, allowing further advancement in technology.

Nanotechnology has a broad range of potential applications spanning from electronics and optics to catalysis and energy storage and production.

Only when the desired size, morphology and chemical composition are obtained is possible to investigate the eventual new physical properties and applications of nanomaterials and nanostructures.

It was also shown that decorating materials with other nanostructures enormously enhances the properties of the nanomaterial.

Heterostructures consisting of nanostructures distributed on the surface of a substrate could potentially display not only unique properties of nanostructures, but also additional novel functionalities and properties due to the interaction between them.

The aim of this thesis was the controlled synthesis of mono- and bi-metallic nanoparticles for application in sensing and energy production.

The dissertation is structured as follows:

Chapter 1: a brief introduction to the world of nanotechnology and nanostructures is presented, with a focus on nano-fabrication techniques. The second part describes the importance of mono- and bi-metallic nanoparticles, with a particular attention of the interaction with a conductive support, the theoretical background, and different applications.

Chapter 2: the synthesis and characterization of mono- and bi-metallic nanoparticles with different solution-based techniques are presented. In particular, chemical reduction of Au, Pd, Pt and Au@Pd (core@shell) nanoparticles is deeply described.

Chapter 3: the decoration of ZnO nanorods with Au nanoparticles is investigated in terms of energy band modification of the semiconductor and modulation of the built-in electric field. Photoluminescence and Cathodoluminescence analyses (supported by Montecarlo and COMSOL simulation) provide a solid basis for the comprehension of the effect of the formation of a nano Schottky junction at the metal-semiconductor interface.

Chapter 4: a new synthesis procedure of NiO microflowers is described. Electrocatalytic intrinsic activity of nanostructures decorated graphene paper is evaluated during oxygen evolution reaction. After decoration of NiO microflowers with Pt nanoparticles, the nanostructures are use as anode electrode for hydrogen evolution reaction. Moreover, A full cell for alkaline electrochemical water splitting has been built, composed of Pt decorated NiO microflowers as cathode and bare NiO microflowers as anode

Chapter 5: the decoration of a Ni oxide nanostructure with NPs of Au, Pd and Au@Pd (Au core, Pd shell) is experimentally investigated. Electrochemical measurements quantitatively elucidate the effect of decoration with mono or bimetallic nanoparticles. The presence of bimetallic nanoparticles enhances enormously the electrochemical performances of the material in terms of sensitivity, catalytic activity, and electrical transport. The modification of energy band diagram in semiconductor is analyzed and discussed also in terms of electron transfer during redox reactions.

Chapter 1

Metal nanoparticles: properties, interactions, and applications

Content

There's plenty of Room at the Bottom	5
Nanostructures: basic properties	7
Metal nanoparticles	12
Importance of metal nanoparticles	12
Impact of nanoparticle–support interaction	12
Bimetallic nanoparticles	14
Structural features of bimetallic nanoparticles	14
Electronic Properties and Catalytic Activity of Bimetallic nanoparticles	16
Applications of metal nanoparticles	21
Conclusions	23
References	24

Summary

Nanoparticles are nanostructures with at least one dimension at the nanoscale level (few nanometers). The optical, electrical, mechanical, magnetic, and catalytic properties of nanoparticles are significantly different from their bulk counterparts due to quantum size effect, surface effect, and dielectric confinement effect.

In this introductory chapter, after a brief historical excursus on nanotechnology, we will focus our attention on basic properties of nanostructures, especially metal nanoparticles. The role of support is introduced and schematized.

Particular attention will be paid to the study of a particular case of metal nanostructures: bimetallic nanoparticles. The presence of two different metals in the same structure can strongly modify the electrical and catalytic properties of the bimetallic nanoparticles. A theoretical approach explaining the enhancement of catalytic properties of bimetallic nanoparticles is presented and detailed. Finally, some examples of application of bimetallic nanoparticles will be provided.

This chapter represents a starting point for developing the key concepts presented in the experimental chapters of this thesis

1.1 There's Plenty of Room at the Bottom

“What could we do with layered structures with just the right layers? What would the properties of materials be if we could really arrange the atoms the way we want them? They would be very interesting to investigate theoretically. I can't see exactly what would happen, but I can hardly doubt that when we have some control of the arrangement of things on a small scale, we will get an enormously greater range of possible properties that substances can have, and of different things that we can do. [...] There's Plenty of Room at the Bottom. I will not now discuss how we are going to do it, but only what is possible in principle - in other words, what is possible according to the laws of physics.”

In his lecture at Caltech, in 1959, Richard P. Feynman predicted the enormous potential of manipulating matter at the atomic scale [1]. It is possible, he proposed, for scientists to assemble new materials at the level of single atoms and molecules, where there are “new kinds of forces and new kinds of possibilities, new kinds of effects”. It is generally accepted that Feynman's words constituted the starting point for the nanotechnology.

Nanotechnology is the ability to build materials, devices, and systems with atomic precision. A brief and general definition of nanotechnology is the statement by the US National Science and Technology Council [2], which states:

“The essence of nanotechnology is the ability to work at the molecular level, atom by atom, to create large structures with fundamentally new molecular organization. The aim is to exploit these properties by gaining control of structures and devices at atomic, molecular, and supramolecular levels and to learn to efficiently manufacture and use these devices”.

Nanotechnology received its greatest momentum with the invention of scanning tunneling microscope (STM) in 1981 by Gerd K. Binnig and Heinrich Rohrer, staff scientists at IBM's Zürich Research Laboratory.

That happened 22 years after Feynman's predictions (Figure 1.1).

The Nobel Prize award in 1986 to Binnig and Rohrer for the discovery of STM was quickly followed by the development of a family of related techniques which, together with STM, may be classified in the general category of Scanning Probe Microscopy (SPM) techniques. Of the latter technologies, the most important is undoubtedly the atomic force microscope (AFM) developed in 1986 by Binnig, Quate, and Gerber.

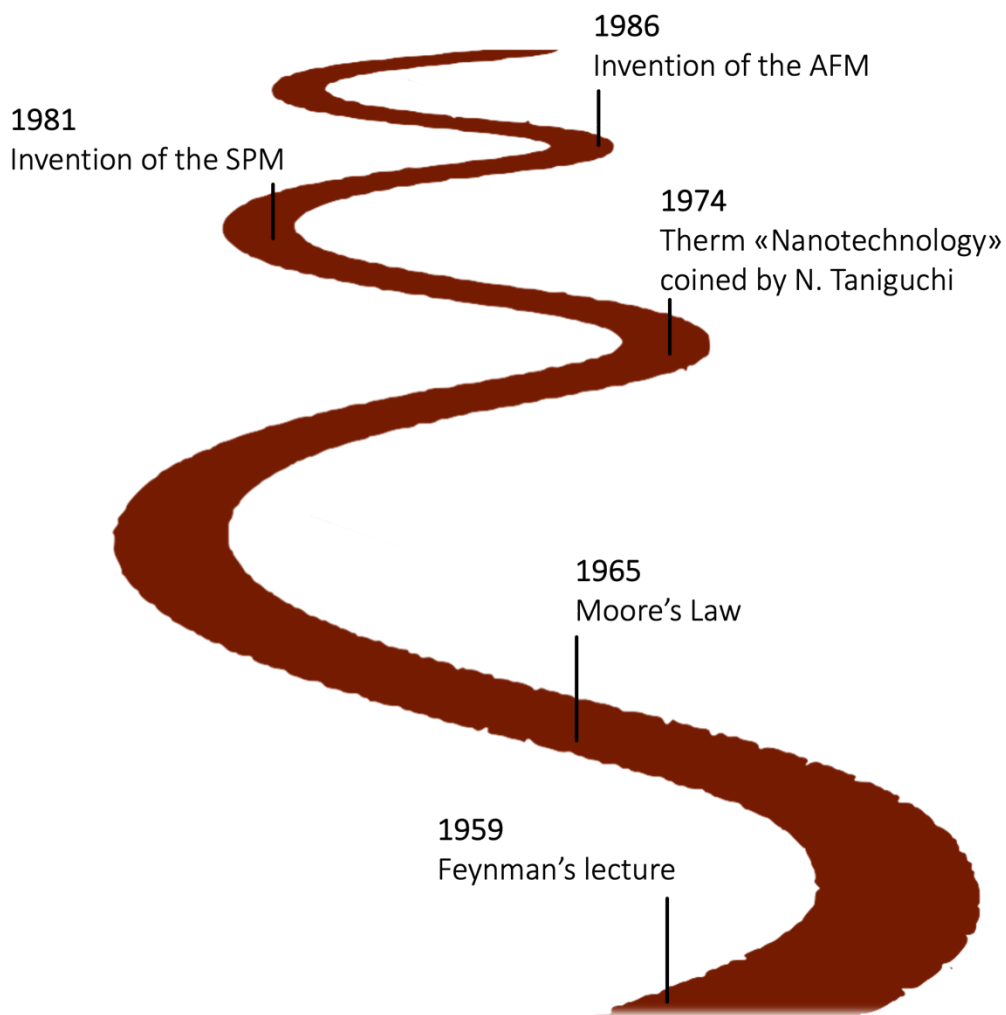


Figure 1.1: Nanotechnology timeline.

1.2 Nanostructures: basic properties

When the size of materials is reduced to nanoscale, the physical and chemical properties change drastically.

As the size of the material reduces from the bulk to nanosize (10^{-9} m), the surface area increases drastically for the same volume of a given material (Figure 1.2(a)). As a result, the nanoparticles exhibit interesting physical and chemical properties, initially unseen in the bulk material.

The chemical reactivity increases as the size of the reactants decreases, particularly at the nano-level. Nanoparticles of materials are highly unstable compared to the corresponding bulk material. The surface atoms are less coordinated to their neighboring atoms, compared to the internal atoms. This implies that the surface atoms have higher energies. For a nanostructure, the number of surface atoms is large (if compared to the total number of atoms), which increases the chemical reactivity of the nanomaterials. The higher surface-to-volume ratio of nanostructures is widely used in many applications, like chemical catalysis, storage devices, solar cells, etc. [3].

In nanomaterials, the electrons are confined to regions having one, two or three dimensions (Figure 1.2(b)) when the relative size is comparable with the de Broglie wavelength.

Nanostructures with one direction below this critical value (thin film, layer structure, quantum well) are defined as 2D nanostructures. When two dimensions are below this critical value (linear chain structure, quantum wire) the nanostructures are defined as 1D and when all the dimensions are also below this threshold (cluster, colloid, nanocrystal, quantum dot) it is referred to as 0D.

In a structure of size similar to the electron de Broglie wavelength, the behavior of the electron should be described quantum mechanically, i.e., by using Schrödinger equation.

The density of states, DOS (number of electronic states per unit volume and energy), is greatly modified for different types of nanostructures depending on the degree of confinement as shown in Figure 1.2(b).

For bulk materials, the DOS has a square root dependence on energy. However, this dependence changes accordingly with the dimensionality of the structures. The variation in DOS with dimensionality results in outstanding optical and electrical properties for realizing advanced nanodevices.

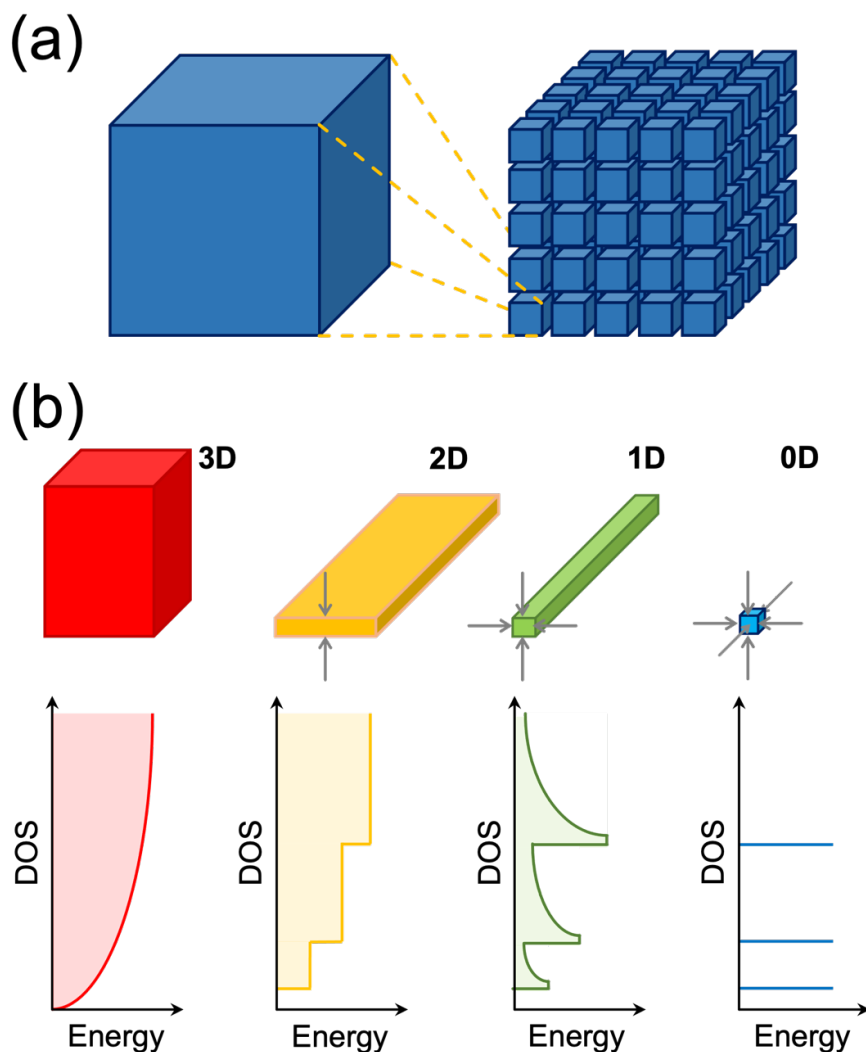


Figure 1.2: (a) a cartoon showing the variations in the surface-to-volume ratio of bulk vs. nano; (b) schematic drawing to show the concept of system dimensionality and the corresponding density of states (DOS) versus energy (E) diagram (for ideal cases) [adapted from 4].

The interest in nanomaterials is driven by their many desirable properties. In particular, the ability to tailor the size and structure provides excellent prospects for designing novel nanodevices.

Numerous nanofabrication methods in nanotechnology have been used successfully. As the technology develops further, new approaches will emerge [5].

In general, two major strategies are used to produce nanostructured materials: the “bottom-up” and “top-down” method, as shown schematically in Figure 1.3.

The top-down approach is based on the assembly of structures by manipulating components of larger volume using lithographic and non-lithographic fabrication technologies in order to fabricate micro- and nano-system components.

On the other hand, the bottom-up approach, arranging atoms or molecules in nanostructures, involves the manufacture of device structures through the systematic assembly of molecules, atoms, or other basic units of matter. In the bottom-up approach, nanoscale features are mainly built up from their elemental constituents.

Elemental constituents are combined using various nanomanufacturing processes including self-assembly, chemical synthesis, molecular beam epitaxy, nano-imprint lithography, roll-to-roll processing, and dip pen lithography [6].

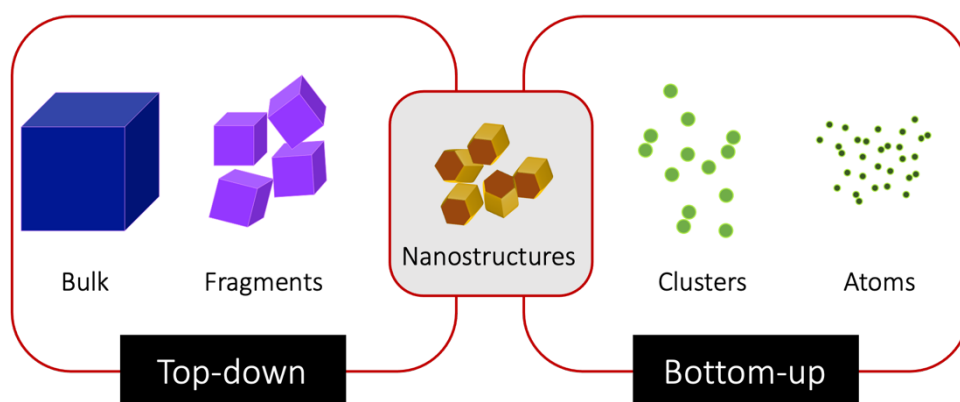


Figure 1.3: Schematic representation of top-down or bottom-up synthesis roots.

One important issue is the availability of raw materials for the synthesis of different types of nanostructures. The increasing need for advanced materials and components that enable certain functions for a variety of important applications, a growing world population and the fact that our earth’s resources are limited raise the question of future material supply. Although their significant economic importance for key sectors in the global economy, most of elements have a high-supply risk and there is a lack of substitutes. Figure 1.4(a) represents a particular periodic table in which the size of each square is proportional to the relative abundance of

each chemical element. Moreover, the color of the squares indicates the availability of these elements in the next years.

The development of new non-precious metal nanostructures is essential for rationally designing highly active low-cost materials as alternatives to state-of-the-art critical raw materials.

Transition non-critical raw materials (metal oxides, sulfides, and carbides) have been deeply explored for decades owing to their low cost, excellent durability, and electrical and physical properties.

Several materials exhibit high catalytic and electrocatalytic performances, mainly due to the presence of noble metals, such as Au, Pt, Pd, Ru, Ir [7]. The scarcity of these elements is easily understandable from Figure 1.4(b). Their amount is about 9 orders of magnitude less than elements such as oxygen, silicon, and iron.

Several strategies have been proposed to minimize the use of noble metals. One approach to overcome these challenges is to increase the surface to bulk atomic ratio of noble metal materials, thus allowing for a lower metal loading to be used without compromising their efficiency [8]. Another strategy is represented by the synthesis of noble metal nanoparticles and their incorporation (decoration) in other nanostructures in order to reduce the amount of critical. Metal decoration of nanostructures is emerging as a promising methodology for adding functionalities and developing materials properties, with applications to electronics, sensing, catalysis, and computing industries [9-15].

In the following sections the importance of nanoparticles (mono- or bi-metallic) will be highlighted. Particular attention will be paid to the effect of the support material and to the modifications of the physical, chemical and catalytic properties of the decorated nanostructures. Moreover, the effect of alloying different metals will be investigated presenting some theoretical backgrounds for the description of the enhancement of the catalytic properties of bimetallic system (*d*-band model). Finally, some example of application in different fields will be described, focusing the attention on catalysis and sensing.

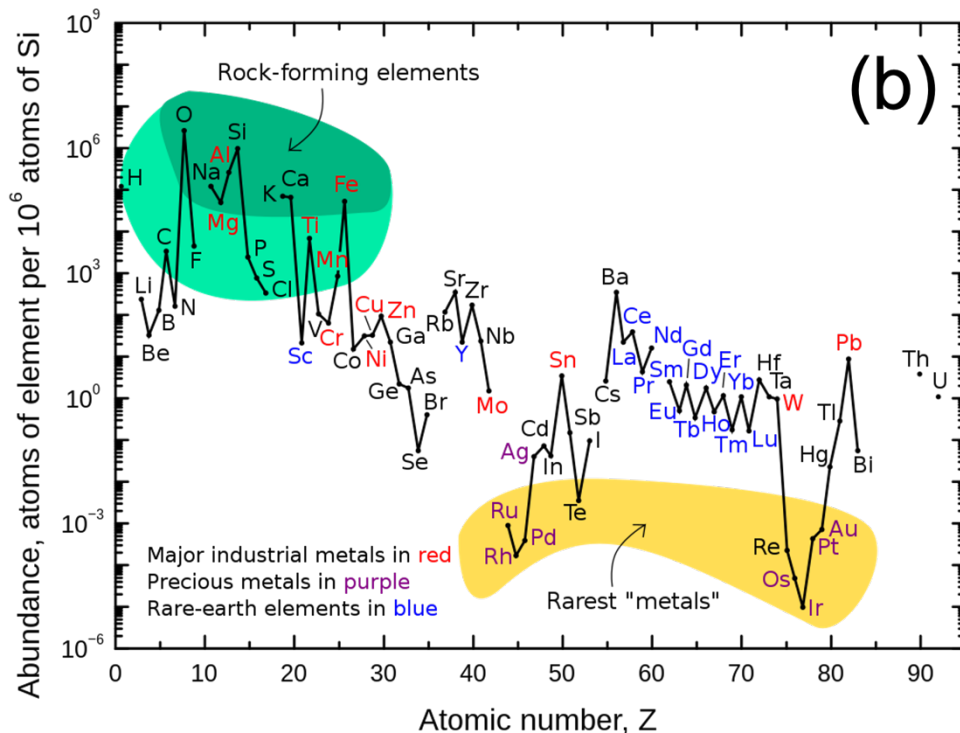
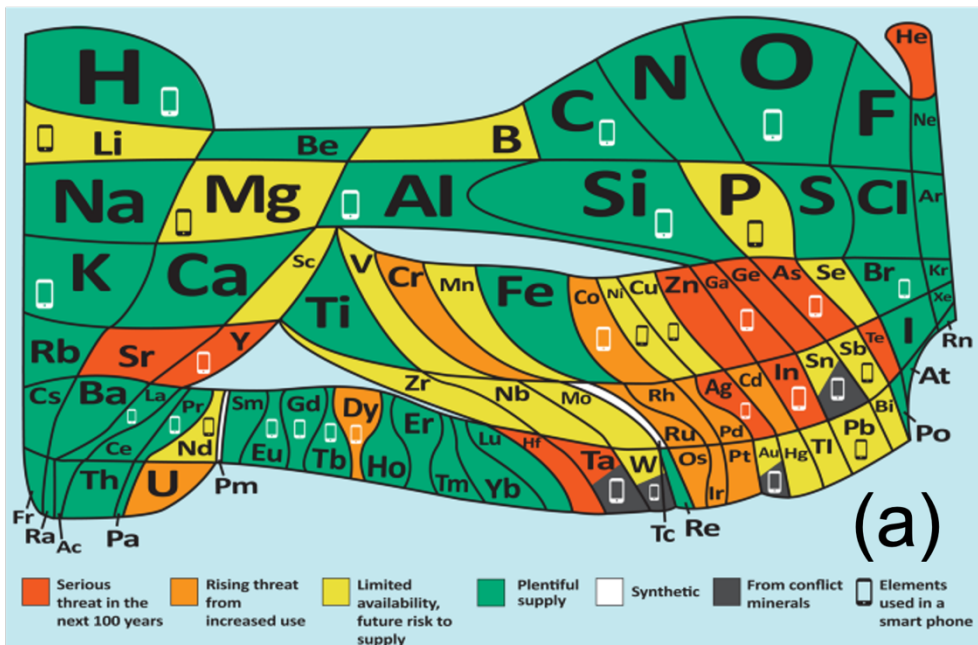


Figure 1.4: (a) Periodic table of the abundance of the elements [16]; (b) Abundance (atom fraction) of the chemical elements in Earth's upper continental crust as a function of atomic number [17].

1.3 Metal nanoparticles

1.3.1 Importance of metal nanoparticles

Nanoparticles (NPs) are of high scientific interest as they show unusual properties compared to their bulk counterparts [18]. As previously remarked, at the nanoscale the properties of the materials change. As the size of a material decreases, the percentage of atoms at its surface becomes substantial. Therefore, the surface-to-volume ratio increases substantially influencing the surface-related properties of the material. In general, the main properties and the advantageous characteristics of NPs are:

- High surface-to-volume ratio[19];
- Higher zeta potential [20];
- Possible separation and recyclability [21].

1.3.2 Impact of nanoparticle–support interaction

Because of their small size and probable solubility in reaction media, it is not always easy to separate metal nanoparticles from the solution. To overcome this problem, NPs are usually anchored onto a solid support [22-27]. There is a large number of the studies reporting on NPs supported on a variety of metal oxides [28-36].

However, supports are typically not inert and the interaction with nanoparticles gives rise to new interface phenomena. Such metal-support interaction may have a profound impact on the resulting performance of the metal nanoparticles [37,38]. Impact on catalysis originates from interactions between metal nanoparticles and their supporting matrix (Figure 1.5(a)). Typical metal- support phenomena relate to five aspects:

1. charge transfer,
2. interfacial perimeter,
3. nanoparticle morphology,
4. chemical composition,
5. strong metal-support interaction (SMSI).

These phenomena are often entangled, and some will have a stronger influence than others, depending on the catalyst and the reaction.

Several synthetic strategies for the control of the metal-support interaction have been reported, which can be classified according to changes to the catalyst's components before and after assembly of the composite material.

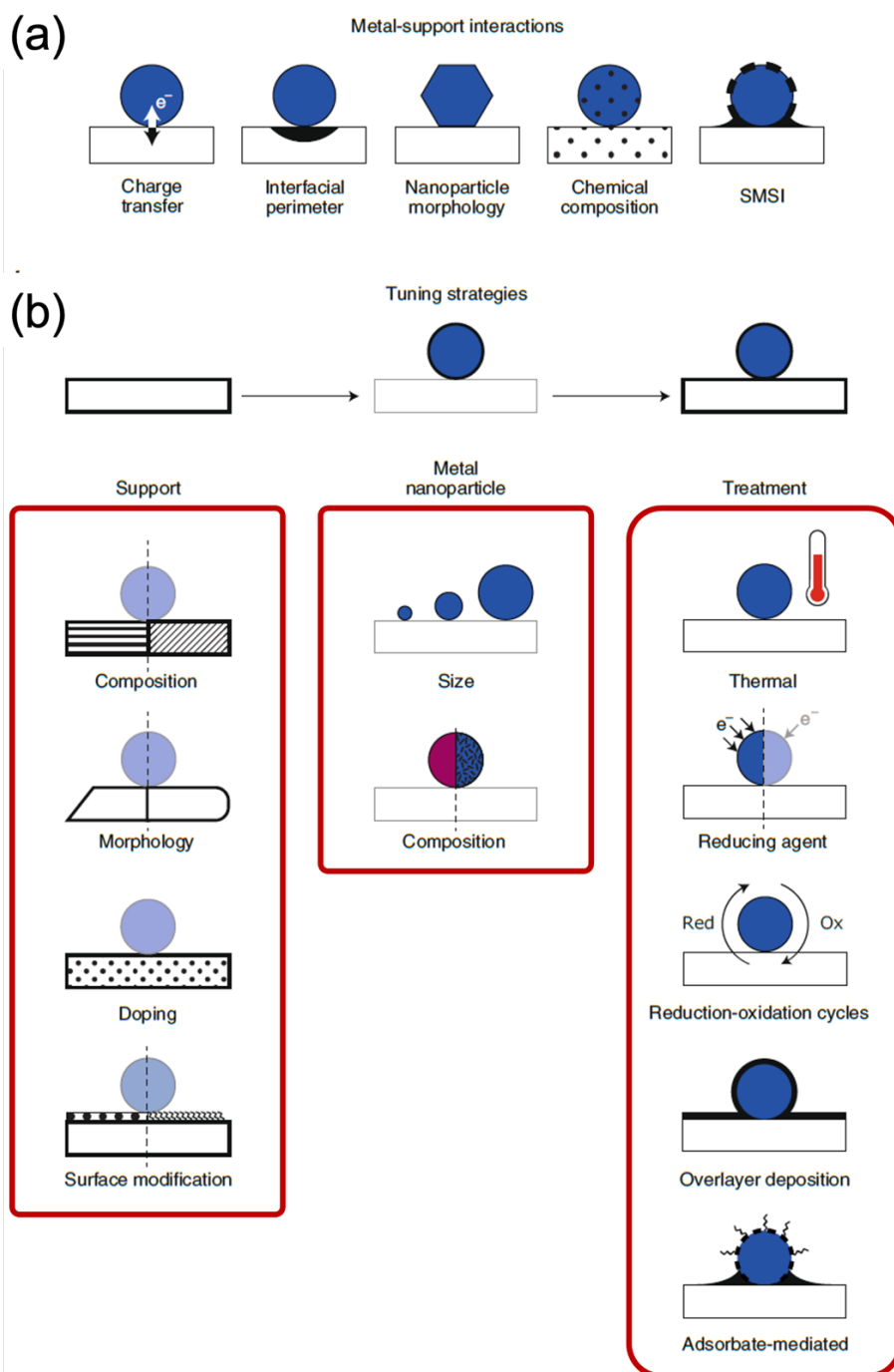


Figure 1.5: (a) The five main phenomena of metal-support interactions; (b) the approaches for tuning such interactions are divided after the different stages of catalyst modification (support, nanoparticle, treatments on the metal-support composite material) [Adapted from 39].

1.4 Bimetallic nanoparticles

Noble metals NPs have been prepared and studied since several years. They became valuable materials in various applications, such as homogeneous and heterogeneous catalysis, nanomedicine, and imaging [41]. Bimetallic NPs have been introduced later but now they represent an exciting area of research because they offer a new degree of freedom to vary the particle properties by blending two metals in one particle [42].

1.4.1 Structural features of bimetallic nanoparticles

In general, the average particle size and the size distribution are the most important properties of nanoparticles. However, these parameters are not always easy to outline and to determine, mainly due to absence of a uniformity in most of NP dispersions [41,43].

The architecture of bimetallic NPs can differ in terms of atomic ordering (alloyed or intermetallic), crystal structure, internal structure (with different numbers of twin defects and/or stacking faults), shape or type of facet, as well as configuration (dimeric, dendritic, or core–shell, including concentric/non-concentric) [44]. Figure 1.7 shows a summary of the major bimetallic architectures typically found in the literature.

Typically, NP can be divided into four main categories [43]:

- *Core-shell segregated NPs*: consist of a shell of one type of atom (B) surrounding a core of another (A). One kind of metal precursor is reduced first, and it gives rise to the generation of an inner core. Then the other kind of metal precursor is decomposed into metallic atoms and grows on the surface of the core.
- *Subcluster segregated NPs*: consist of A and B subclusters, which may share a mixed interface (left) or may only have a small number of A-B bonds (right).
- *Mixed A-B nanoalloys*: may be either ordered (left) or random (i.e., a solid solution, right).
- *Multishell nanoalloys*: may present layered or onion-like alternating -A-B-A- shells.

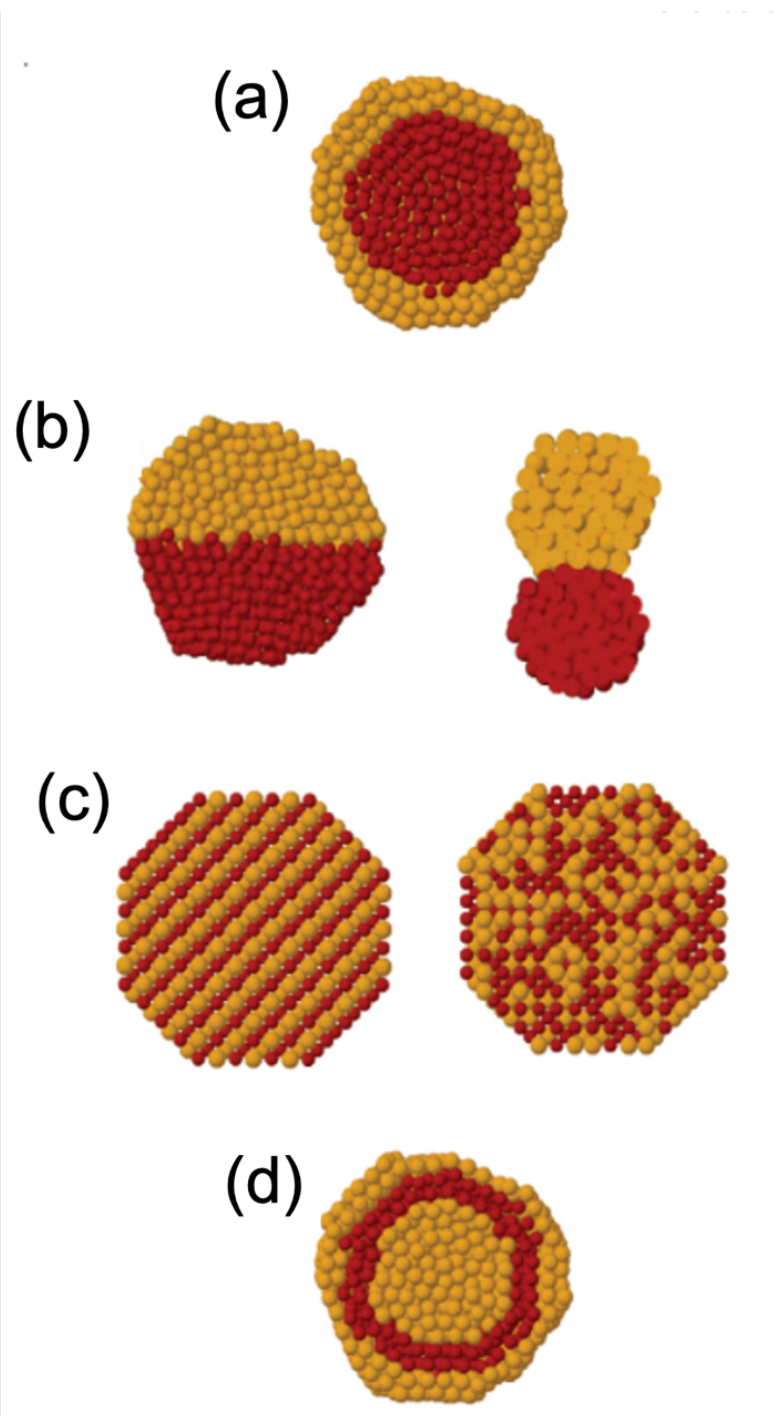


Figure 1.7: Schematic representation of some possible mixing patterns: core-shell (a), subcluster segregated (b), mixed (c), three shell (d). The pictures show cross sections of the clusters [Adapted from 43].

The degree of mixing and atomic ordering in NPs depends mainly on the following factors [42,43]:

1. Bond strengths of A-A, B-B, and A-B bonds.
2. Surface energies of bulk elements A and B.
3. Relative atomic sizes.
4. Charge transfer.
5. Size of single nanoparticles.
6. Specific electronic/magnetic effects.

In addition to being more complicated than their monometallic counterparts, bimetallic NPs are superior in many ways.

Independently of the ordering, a certain improvement of catalytic and sensing performance is observed and typically explained inferring a *synergistic effect* [45].

The property modulation of bimetallic nanoparticles is mainly dependent on these synergetic effects between two distinct elements, including electronic effect, lattice stress, bifunctional effect, and ensemble effect [42].

A clear example of this phenomenon will be deeply investigated in Chapter 5, in which the catalytic properties of supported Au@Pd bimetallic NPs were compared with those of monometallic Au and Pd NPs.

1.4.2 Electronic Properties and Catalytic Activity of Bimetallic nanoparticles

Experimental characterization of bimetallic nanoparticles, in terms of electrical, catalytic, optical properties, is quite limited despite recent developments. Most of the time the interpretation of experimental findings relies heavily on theoretical modeling, simulations, or statistical approaches. Most NPs properties fall in the nanoscale since they cannot be inferred by extrapolation of their bulk counterparts.

In this paragraph we want to give a theoretical perspective of electronic properties of bimetallic systems and their influences on catalytic activity [46,47].

The *d*-Band Model

The *d*-band model, developed by Hammer and Nørskov [42,45,48], has played a central role in understanding chemical reactivity and the adsorption on transition metal surfaces.

In these materials, the electronic states arising from s and p orbitals of transition metal atoms are delocalized and form wide energy bands. The overlap of d orbitals is much weaker, and therefore leads to narrow energy bands.

The different behaviors of sp and d orbitals heavily impact on chemical adsorption on transition metal surface. It can be decomposed into two steps, as illustrated in Figure 1.8 [45].

1. In the first step, the external orbitals of the adsorbate interact with the wide sp band of the metal surface. As a result, the energy level becomes a renormalized resonance peak (with an energy determined by the interaction strength and a position shifted towards lower energy).
2. In the second step, the renormalized molecular state interacts with the narrow d -band of the metal surface and splits into bonding and anti-bonding states.

The adsorption energy can therefore be written as

$$\Delta E_{ads} = \Delta E_{sp} + \Delta E_d \quad (1.1)$$

It includes the contribution of both sp and d states.

It has been well established that the magnitude of ΔE_d is strongly correlated to the d -band center with respect to the Fermi level (E_F) [45,48]. In general, the higher d -band center in energy leads to stronger adsorption [48].

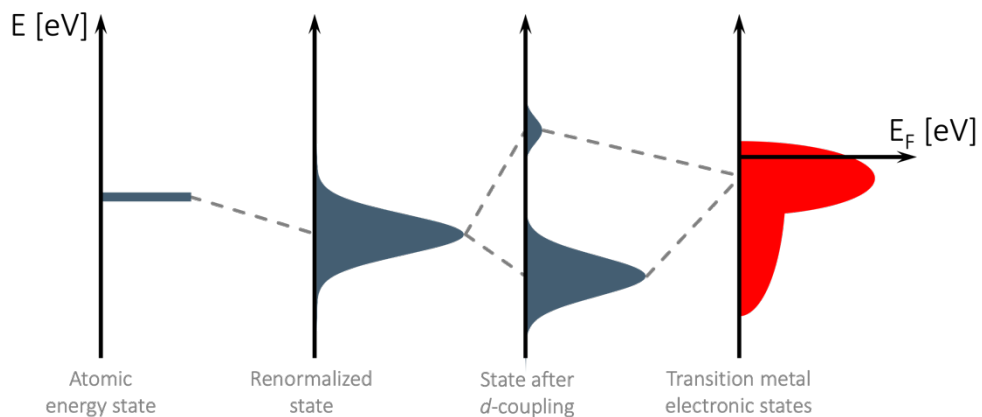


Figure 1.8: Illustration of the d-band model [adapted from [42].

The d -band model gives a connection between the intrinsic electronic properties and the catalytic activity of transition metals.

The d -band model can also be used to understand the variation of the catalytic activity when the transition metal is strained or compressed [128]. In the case of tensile strain, the d -band is narrowed because of reduced inter-atomic overlap and has to shift toward higher energy to maintain a constant number of d -electrons. An opposite process occurs if the transition metal surface is compressed.

Another theoretical approach to investigate the electronic and catalytic properties of bimetallic systems is the so-called monolayer bimetallic surfaces method (Figure 1.9) [49-52]. Different monolayer bimetallic surfaces can be considered:

- (a) a monolayer of the guest metal on top of the host metal;
- (b) the second layer of the host metal is replaced by the guest metal;
- (c) the alloyed (intermixed) surface with a pure metal substrate.

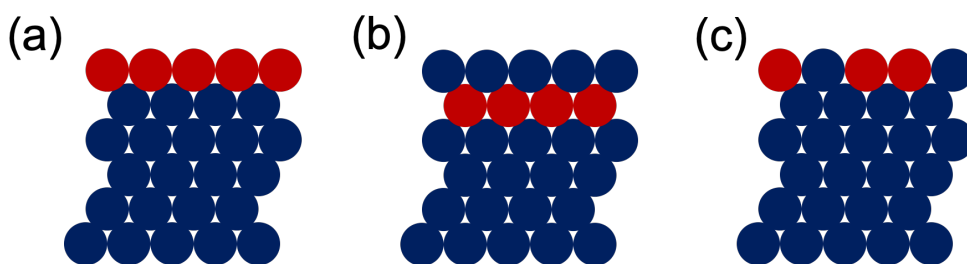


Figure 1.9: Monolayer bimetallic surfaces: (a) the overlayer structure; (b) the subsurface monolayer structure; and (c) the alloyed surface with a pure metal substrate.

Tuning the Reactivity of Bimetallic Surfaces

There are four main mechanisms (Figure 1,10) strictly related with the ability of the tuning of reactivity of transition metal surfaces with the introduction of a second metal [45-49]:

- strain effect
- ligand effect
- ensemble effect
- overlayering effect

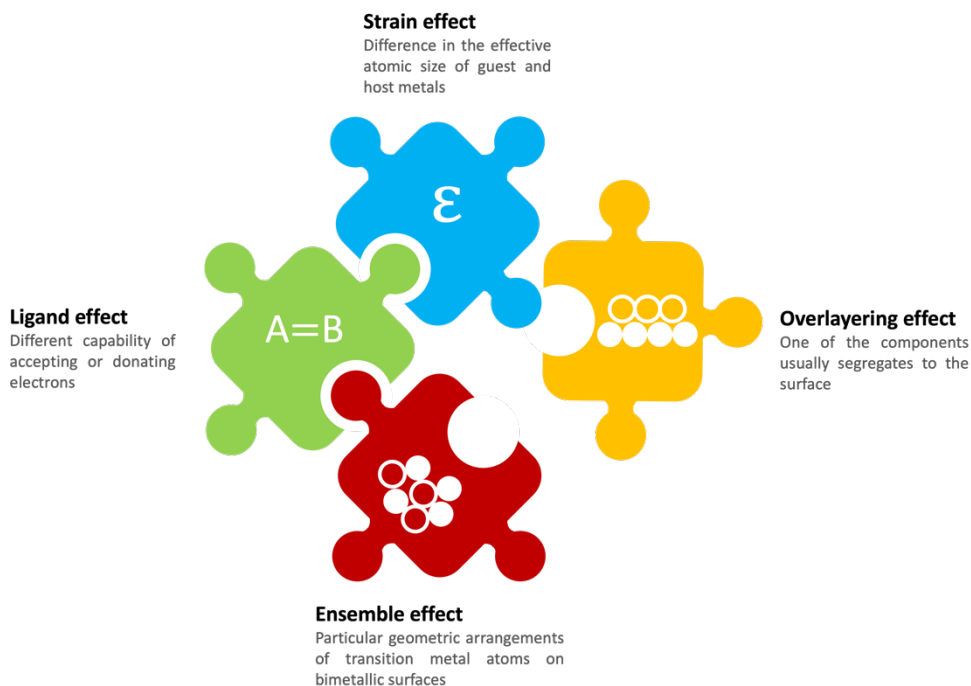


Figure 1.10: Schematic representation of the four mechanisms that affect the reactivity of bimetallic systems.

Strain Effect

The presence of an adlayer of a host material could cause a compressive or tensile strain due to the difference in the effective atomic size of guest and host metals, which can change the *d*-band width and position.

Ligand Effect

Two metals, with different capability of accepting or donating electrons, can form heteronuclear bonds that are significantly different from those in pure metals. This effect is often termed as the *ligand effect*[50].

Ensemble Effect

Also known as geometric effect, it refers to the effect related to particular geometric arrangements of transition metal atoms on bimetallic surfaces [53]. Adsorption energy depends sensitively on the ensemble configuration.

Overlayering effect

As discussed above, overlayer is one of the components of a bimetallic system that segregates to the surface [45]. In such systems, the overlayer atoms have ligand effects from the second layer, but they also have to adapt to the lattice constant of the host metals (strain effects).

Figure 1.11 shows a systematic theoretical study of shifts in d -band centers as different transition metals are deposited on host materials.

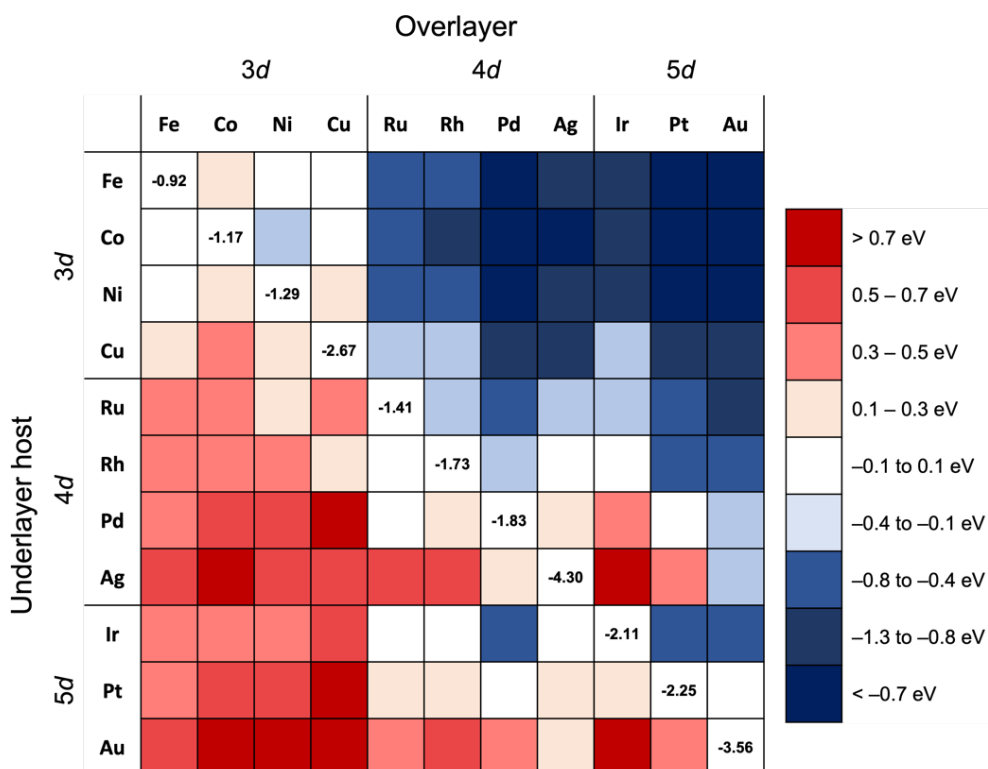


Figure 1.11: Calculated shifts in the d -band centers for several overlayer structures. The shifts are given relative to the d -band center for the pure metal surface. These shifts reflect the change in reactivity of the overlayer relative to the pure metal [Adapted from 45].

1.5 Applications of metal nanoparticles

Bimetallic nanostructures have been developed to minimize the utilization of precious metals or to exploit the secondary function to the primary metal surface. These features can affect the surface reaction with different activity, selectivity, and durability.

Four main applications can be recognized as illustrated by Figure 1.12.

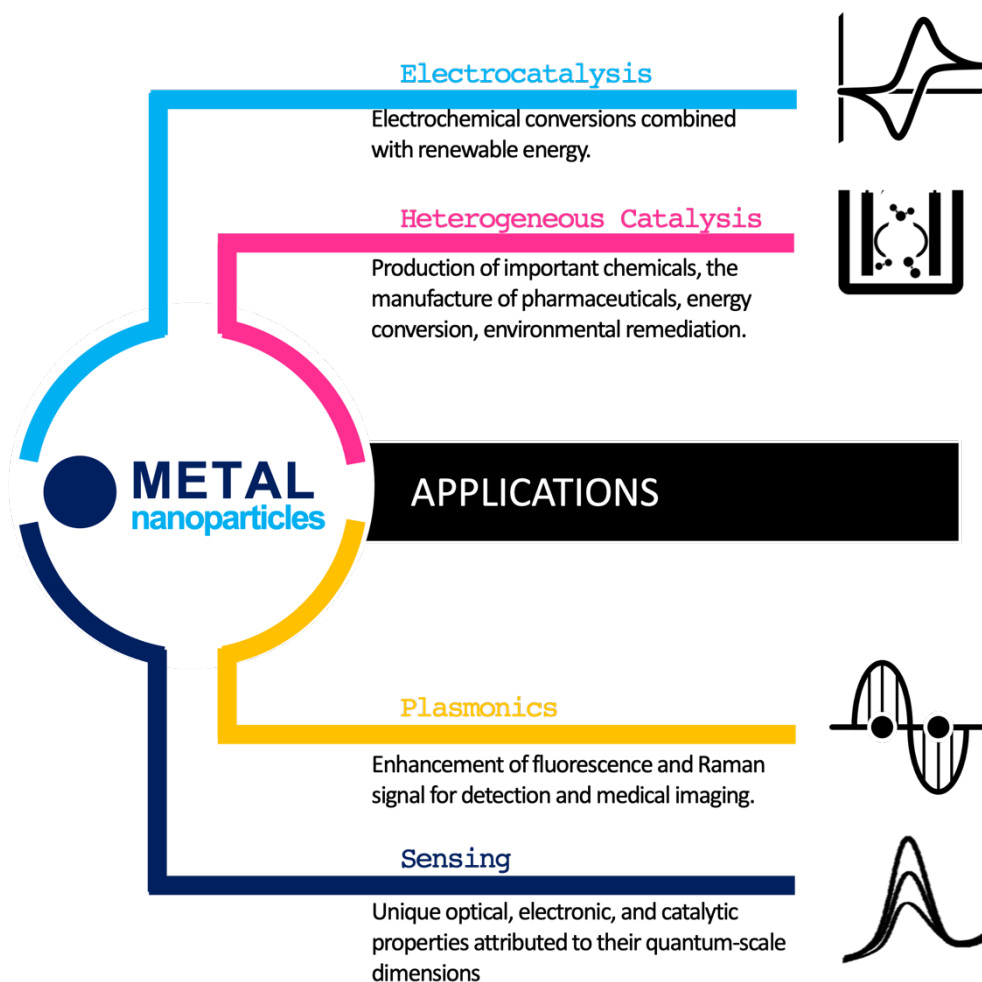


Figure 1.12: Schematic illustration of the four different categories of application of metal nanoparticles.

Electrocatalysis

Mono- and bi-metallic NPs have been widely used for various surface and electrochemical reactions [54]. For energy and environmental issues, there has been much attention to electrochemical conversions combined with renewable energy [55].

Some important reactions and corresponding mono- and bi-metallic nanostructured electrocatalysts are listed below:

- *Oxygen Reduction Reaction (ORR).*
- *Fuel Oxidation.*
- *Oxygen Evolution Reaction (OER).*

Heterogeneous catalysis

Heterogeneous catalysts have been widely used for the production of chemicals, energy conversion, and environmental remediation [59-78]. Bimetallic catalysts have also been developed with modified electronic and geometric structures that provide more control to tune reaction pathways [61,62].

Four categories of reactions can be distinguished:

- *CO Oxidation.*
- *Hydrogenation/Dehydrogenation.*
- *Hydrogen Evolution Reaction (HER).*
- *Coupling Reactions.*

Plasmonics

Surface Plasmon Resonance (SPR) is one of the most important properties of noble metals, which holds great promise for bio-imaging, molecular detecting, and solar cells [44].

Because of the synergistic effect, bimetallic NPs not only have properties of single component but also some extraordinary properties [79]. Bimetallic NPs (in particular, Au-Ag and Au-Pd) have received increasing attention in the past ten years [80].

Sensing

A sensor can selectively recognize the target analyte in a complex matrix and produce a measurable signal. Compared with bulk metals, metal NPs show unique optical, electronic, and catalytic properties attributed to their nanosize [44,81,82]. Moreover, bimetallic nanoparticles often provide

optimized chemical and physical properties than their monometallic counterpart with better sensitivity and selectivity.

Different types of sensors can be recognized [83-92]:

- *Plasmonic sensors.*
- *SERS-based sensors.*
- *Luminescence-based sensors.*
- *Electrochemical sensors.*
- *Gas sensors.*

1.6 Conclusions

In this chapter, the basic properties of mono- and bi-metallic nanoparticles were explored. The effect of the support was highlighted pointing out how it is fundamental in modify and determine the overall electrical and catalytic properties of the decorated materials. Particular importance was given to the theoretical description of the bimetallic effect and to the possible uses of metal nanoparticles in different applications. The Nørskov's d-band model was introduced as a possible theoretical description for the effect of alloying different transition metals on adsorption of molecules. What has just been described provides a background to the topics covered in the following chapters. The effect of the decoration of metal oxide nanostructures (ZnO, NiO) with Au, Pd, Pt and Au @ Pd (core-shell) NPs will be systematically investigated. The experimental results of the analyzes and the simulations will provide the working basis for developing simplified models to describe the NP-support interaction. Particular attention will be paid to the study of the modification of the electrical and electrochemical properties of the decorated nanostructures and to the variation in the position of the energy bands due the formation of a junction at the semiconductor metal interface.

References

- [1] R.P. Feynman, There's Plenty of Room at the Bottom (1960).
- [2] M. C. Roco, S. Williams, P. Alivisatos, Nanotechnology Research Directions: IWGN Workshop Report - Vision for Nanotechnology R&D in the Next Decade (1999).
- [3] K. G. Reddy, T. G. Deepak, G. S. Anjusree, S. Thomas, S. Vadukumpully, K. R. V. Subramanian, S. V. Nair and A. S. Nair, On global energy scenario, dye-sensitized solar cells and the promise of nanotechnology, *Phys.Chem.Chem.Phys.* (2014).
- [4] S. Suresh, Semiconductor Nanomaterials, Methods and Applications: A Review, *Nanoscience and Nanotechnology* (2013).
- [5] T. Tsakalakos, I. A. Ovid'ko, A. K. Vasudevan (ed.), *Nanostructures: Synthesis, Functional Properties and Applications*, Springer Science+Business Media (2001).
- [6] B. Bhushan, *Springer Handbook of Nanotechnology*, Springer-Verlag (2017).
- [7] Carollo, G., Garbujo, A., Mauvy, F. & Glisenti, A. Critical Raw Material-Free Catalysts and Electrocatalysts: Complementary Strategies to Activate Economic, Robust, and Ecofriendly SrTiO₃. *Energy and Fuels* (2020) doi:10.1021/acs.energyfuels.0c01678.
- [8] Esposito, D. V. et al. Low-cost hydrogen-evolution catalysts based on monolayer platinum on tungsten monocarbide substrates. *Angew. Chemie - Int. Ed.* (2010) doi:10.1002/anie.201004718.
- [9] Dai, S.; Chou, J.P.; Wang, K.W.; Hsu, Y.Y.; Hu, A.; Pan, X.; Chen, T.Y. Platinum-trimer decorated cobalt-palladium core-shell nanocatalyst with promising performance for oxygen reduction reaction. *Nat. Commun.* (2019), doi:10.1038/s41467-019-08323-w.
- [10] Ranjan, P.; Shankar, S.; Popovitz-Biro, R.; Cohen, S.R.; Kaplan-Ashiri, I.; Dadosh, T.; Shimon, L.J.W.; Višić, B.; Tenne, R.; Lahav, M.; et al. Decoration of Inorganic Nanostructures by Metallic Nanoparticles to Induce Fluorescence, Enhance Solubility, and Tune Band Gap. *J. Phys. Chem. C* (2018), doi:10.1021/acs.jpcc.8b00510.

- [11] Su, S.; Xu, Y.; Sun, Q.; Gu, X.; Weng, L.; Wang, L. Noble metal nanostructures-decorated molybdenum disulfide nanocomposites: synthesis and application, *J. Mater. Chem. B* (2018), doi:10.1039/C8TB01659C.
- [12] Bhardwaj, N.; Satpati, B.; Mohapatra, S. Plasmon-enhanced photoluminescence from SnO₂ nanostructures decorated with Au nanoparticles, *Appl. Surf. Sci.* (2020), doi:10.1016/j.apsusc.2019.14438.
- [13] Wang, C.; Wang, T.; Wang, B.; Zhou, X.; Cheng, X.; Sun, P.; Zheng, J.; Lu, G. Design of α -Fe₂O₃ nanorods functionalized tubular NiO nanostructure for discriminating toluene molecules. *Sci. Rep.* (2016), doi:10.1038/srep26432.
- [14] Shi, Y.; Huang, J.K.; Jin, L.; Hsu, Y. Te; Yu, S.F.; Li, L.J.; Yang, H.Y. Selective decoration of Au nanoparticles on monolayer MoS₂ single crystals. *Sci. Rep.* (2013), doi:10.1038/srep01839.
- [15] Walters, G.; Parkin, I.P. The incorporation of noble metal nanoparticles into host matrix thin films: Synthesis, characterisation and applications. *J. Mater. Chem.* (2009), doi:10.1039/b809646e.
- [16] <https://www.euchems.eu/euchems-periodic-table/>
- [17] <https://en.wikipedia.org>.
- [18] Ndolomingo, M. J., Bingwa, N. & Meijboom, R. Review of supported metal nanoparticles: synthesis methodologies, advantages and application as catalysts. *Journal of Materials Science* (2020) doi:10.1007/s10853-020-04415-x.
- [19] Astruc, D., Lu, F. & Aranzaes, J. R. Nanoparticles as recyclable catalysts: The frontier between homogeneous and heterogeneous catalysis. *Angewandte Chemie - International Edition* (2005) doi:10.1002/anie.200500766.
- [20] Thielbeer, F., Donaldson, K. & Bradley, M. Zeta potential mediated reaction monitoring on nano and microparticles. *Bioconjug. Chem.* (2011) doi:10.1021/bc1005015.
- [21] Polshettiwar, V. & Varma, R. S. Green chemistry by nanocatalysis. *Green Chem.* (2010) doi:10.1039/b921171c.

- [22] Gurav, J. L., Jung, I. K., Park, H. H., Kang, E. S. & Nadargi, D. Y. Silica aerogel: Synthesis and applications. *J. Nanomater.* (2010) doi:10.1155/2010/409310.
- [23] Jiang, Z. J., Liu, C. Y. & Sun, L. W. Catalytic properties of silver nanoparticles supported on silica spheres. *J. Phys. Chem. B* (2005) doi:10.1021/jp046032g.
- [24] Hori, K., Matsune, H., Takenaka, S. & Kishida, M. Preparation of silica-coated Pt metal nanoparticles using microemulsion and their catalytic performance. *Sci. Technol. Adv. Mater.* (2006) doi:10.1016/j.stam.2006.09.013.
- [25] He, L., Lin, Q., Liu, Y. & Huang, Y. Unique catalysis of Ni-Al hydrotalcite derived catalyst in CO₂ methanation: Cooperative effect between Ni nanoparticles and a basic support. *J. Energy Chem.* (2014) doi:10.1016/S2095-4956(14)60144-3.
- [26] Peng, X. et al. Impact of Hydrogenolysis on the Selectivity of the Fischer-Tropsch Synthesis: Diesel Fuel Production over Mesoporous Zeolite-Y-Supported Cobalt Nanoparticles. *Angew. Chemie - Int. Ed.* (2015) doi:10.1002/anie.201411708.
- [27] Cheng, D. G., Jin, W., Zhan, X. & Chen, F. Alumina membrane coated activated carbon: A novel strategy to enhance the mechanical properties of a solid catalyst. *RSC Adv.* (2016) doi:10.1039/c5ra23769f.
- [28] Raybaud, P. et al. From γ -alumina to supported platinum nanoclusters in reforming conditions: 10 years of DFT modeling and beyond. *J. Catal.* (2013) doi:10.1016/j.jcat.2013.08.015.
- [29] Bagheri, S., Muhd Julkapli, N. & Bee Abd Hamid, S. Titanium dioxide as a catalyst support in heterogeneous catalysis. *Scientific World Journal* (2014) doi:10.1155/2014/727496.
- [30] Ntais, S., Isaifan, R. J. & Baranova, E. A. An X-ray photoelectron spectroscopy study of platinum nanoparticles on yttria-stabilized zirconia ionic support: Insight into metal support interaction. *Mater. Chem. Phys.* (2014) doi:10.1016/j.matchemphys.2014.08.033.
- [31] Mori, K., Hara, T., Mizugaki, T., Ebitani, K. & Kaneda, K. Hydroxyapatite-supported palladium nanoclusters: A highly active heterogeneous catalyst for selective oxidation of alcohols by use of molecular oxygen. *J. Am. Chem. Soc.* (2004) doi:10.1021/ja0488683.

- [32] Kantam, M. L., Chakravarti, R., Pal, U., Sreedhar, B. & Bhargava, S. Nanocrystalline magnesium oxide-stabilized palladium(0): An efficient and reusable catalyst for selective reduction of nitro compounds. *Adv. Synth. Catal.* (2008) doi:10.1002/adsc.200800018.
- [33] Wang, L. C. et al. MnO₂ nanorod supported gold nanoparticles with enhanced activity for solvent-free aerobic alcohol oxidation. *J. Phys. Chem. C* (2008) doi:10.1021/jp711333t.
- [34] Wu, H., Wang, L., Zhang, J., Shen, Z. & Zhao, J. Catalytic oxidation of benzene, toluene and p-xylene over colloidal gold supported on zinc oxide catalyst. *Catal. Commun.* (2011) doi:10.1016/j.catcom.2011.02.012.
- [35] Yamada, Y., Yano, K., Xu, Q. & Fukuzumi, S. Cu/Co₃O₄ nanoparticles as catalysts for hydrogen evolution from ammonia borane by hydrolysis. *J. Phys. Chem. C* (2010) doi:10.1021/jp104291s.
- [36] Pérez-Mayoral, E., Calvino-Casilda, V. & Soriano, E. Metal-supported carbon-based materials: Opportunities and challenges in the synthesis of valuable products. *Catalysis Science and Technology* (2016) doi:10.1039/c5cy01437a.
- [37] Pacchioni, G. & Freund, H. J. Controlling the charge state of supported nanoparticles in catalysis: lessons from model systems. *Chemical Society Reviews* (2018) doi:10.1039/c8cs00152a.
- [38] Farmer, J. A. & Campbell, C. T. Ceria maintains smaller metal catalyst particles by strong metal-support bonding. *Science* (80-.). (2010) doi:10.1126/science.1191778.
- [39] van Deelen, T. W., Hernández Mejía, C. & de Jong, K. P. Control of metal-support interactions in heterogeneous catalysts to enhance activity and selectivity. *Nature Catalysis* (2019) doi:10.1038/s41929-019-0364-x.
- [40] Rodríguez-Gómez, A., Platero, F., Caballero, A. & Colón, G. Improving the direct synthesis of hydrogen peroxide from hydrogen and oxygen over Au-Pd/SBA-15 catalysts by selective functionalization. *Mol. Catal.* (2018) doi:10.1016/j.mcat.2017.10.034.
- [41] Loza, K., Heggen, M. & Epple, M. Synthesis, Structure, Properties, and Applications of Bimetallic Nanoparticles of Noble Metals. *Advanced Functional Materials* (2020) doi:10.1002/adfm.201909260.

- [42] Zhang, Y. W. *Bimetallic Nanostructures*. Wiley (2018). doi:10.1002/9781119214618.
- [43] Ferrando, R., Jellinek, J. & Johnston, R. L. *Nanoalloys: From theory to applications of alloy clusters and nanoparticles*. *Chemical Reviews* (2008) doi:10.1021/cr040090g.
- [44] Gilroy, K. D., Ruditskiy, A., Peng, H. C., Qin, D. & Xia, Y. *Bimetallic nanocrystals: Syntheses, properties, and applications*. *Chem. Rev.* (2016) doi:10.1021/acs.chemrev.6b00211.
- [45] Nørskov, J. K., Studt, F., Abild-Pedersen, F. & Bligaard, T. *Fundamental Concepts in Heterogeneous Catalysis*. Wiley (2014) doi:10.1002/9781118892114.
- [46] Bazin, D. et al. *Reactivity and catalysis by nanoalloys*. in *Nanoalloys* (2013). doi:10.1016/B978-0-12-394401-6.00009-6.
- [47] Piccolo, L. *Surface Studies of Catalysis by Metals: Nanosize and Alloying Effects*. in *Engineering Materials* (2012). doi:10.1007/978-1-4471-4014-6_11.
- [48] Hammer, B. & Nørskov, J. K. *Theoretical surface science and catalysis—calculations and concepts*. *Adv. Catal.* (2000) doi:10.1016/S0360-0564(02)45013-4.
- [49] Ruban, A., Hammer, B., Stoltze, P., Skriver, H. L. & Nørskov, J. K. *Surface electronic structure and reactivity of transition and noble metals*. in *Journal of Molecular Catalysis A: Chemical* (1997). doi:10.1016/S1381-1169(96)00348-2.
- [50] Rodriguez, J. A. & Goodman, D. W. *The nature of the metal-metal bond in bimetallic surfaces*. *Science* (1992) doi:10.1126/science.257.5072.897.
- [51] Chen, J. G., Menning, C. A. & Zellner, M. B. *Monolayer bimetallic surfaces: Experimental and theoretical studies of trends in electronic and chemical properties*. *Surface Science Reports* (2008) doi:10.1016/j.surfrep.2008.02.001.
- [52] Yu, W., Porosoff, M. D. & Chen, J. G. *Review of Pt-based bimetallic catalysis: From model surfaces to supported catalysts*. *Chemical Reviews* (2012) doi:10.1021/cr300096b.

- [53] Ponec, V. Alloy catalysts: The concepts. *Appl. Catal. A Gen.* (2001) doi:10.1016/S0926-860X(01)00828-6.
- [54] Peng, Z. & Yang, H. Designer platinum nanoparticles: Control of shape, composition in alloy, nanostructure and electrocatalytic property. *Nano Today* (2009) doi:10.1016/j.nantod.2008.10.010.
- [55] She, Z. W. et al. Combining theory and experiment in electrocatalysis: Insights into materials design. *Science* (2017) doi:10.1126/science.aad4998.
- [56] Antolini, E. Iridium as catalyst and cocatalyst for oxygen evolution/reduction in acidic polymer electrolyte membrane electrolyzers and fuel cells. *ACS Catalysis* (2014) doi:10.1021/cs4011875.
- [57] Danilovic, N. et al. Using surface segregation to design stable Ru-Ir oxides for the oxygen evolution reaction in acidic environments. *Angew. Chemie - Int. Ed.* (2014) doi:10.1002/anie.201406455.
- [58] Rossmeisl, J., Qu, Z. W., Zhu, H., Kroes, G. J. & Nørskov, J. K. Electrolysis of water on oxide surfaces. *J. Electroanal. Chem.* (2007) doi:10.1016/j.jelechem.2006.11.008.
- [59] An, K. & Somorjai, G. A. Nanocatalysis I: Synthesis of Metal and Bimetallic Nanoparticles and Porous Oxides and Their Catalytic Reaction Studies. *Catal. Letters* (2015) doi:10.1007/s10562-014-1399-x.
- [60] Narayanan, R. & El-Sayed, M. A. Catalysis with transition metal nanoparticles in colloidal solution: Nanoparticle shape dependence and stability. *J. Phys. Chem. B* (2005) doi:10.1021/jp051066p.
- [61] Greeley, J. & Mavrikakis, M. Alloy catalysts designed from first principles. *Nat. Mater.* (2004) doi:10.1038/nmat1223.
- [62] Yu, W., Porosoff, M. D. & Chen, J. G. Review of Pt-based bimetallic catalysis: From model surfaces to supported catalysts. *Chemical Reviews* (2012) doi:10.1021/cr300096b.
- [63] Campbell, C. T., Ertl, G., Kuipers, H. & Segner, J. A molecular beam study of the catalytic oxidation of CO on a Pt(111) surface. *J. Chem. Phys.* (1980) doi:10.1063/1.440029.
- [64] Park, J. Y., Zhang, Y., Grass, M., Zhang, T. & Somorjai, G. A. Tuning of catalytic CO oxidation by changing composition of Rh-Pt bimetallic nanoparticles. *Nano Lett.* (2008) doi:10.1021/nl073195i.

- [65] Tao, F. et al. Reaction-driven restructuring of Rh-Pd and Pt-Pd core-shell nanoparticles. *Science* (80-.). (2008) doi:10.1126/science.1164170.
- [66] Matar, S., Mirbach, M. J. & Tayim, H. A. Hydrogenation—Dehydrogenation Processes. in *Catalysis in Petrochemical Processes* (1989). doi:10.1007/978-94-009-1177-2_3.
- [67] Au, M., Meziani, M. J., Sun, Y. P. & Pinkerton, F. E. Synthesis and performance evaluation of bimetallic lithium borohydrides as hydrogen storage media. *J. Phys. Chem. C* (2011) doi:10.1021/jp2065776.
- [68] Singh, S. K., Singh, A. K., Aranishi, K. & Xu, Q. Noble-metal-free bimetallic nanoparticle-catalyzed selective hydrogen generation from hydrous hydrazine for chemical hydrogen storage. *J. Am. Chem. Soc.* (2011) doi:10.1021/ja208475y.
- [69] Yu, W. Y., Mullen, G. M., Flaherty, D. W. & Mullins, C. B. Selective hydrogen production from formic acid decomposition on Pd-Au bimetallic surfaces. *J. Am. Chem. Soc.* (2014) doi:10.1021/ja505192v.
- [70] Graetz, J. New approaches to hydrogen storage. *Chem. Soc. Rev.* (2009) doi:10.1039/b718842k.
- [71] Zhan, W. W., Zhu, Q. L. & Xu, Q. Dehydrogenation of Ammonia Borane by Metal Nanoparticle Catalysts. *ACS Catalysis* (2016) doi:10.1021/acscatal.6b02209.
- [72] Sun, Y. et al. Hydrogen Storage in Metal-Organic Frameworks. *Journal of Inorganic and Organometallic Polymers and Materials* (2013) doi:10.1007/s10904-012-9779-4.
- [73] Bruno, L., Battiato, S., Scuderi, M., Priolo, F., Terrasi, A., Mirabella, S., Physical insights into alkaline overall water splitting with NiO microflowers electrodes with ultra-low amount of Pt catalyst. *Int. J. Hydrogen Energy* (2022) doi:10.1016/j.ijhydene.2022.08.005.
- [74] Schmidt, N. G., Eger, E. & Kroutil, W. Building Bridges: Biocatalytic C-C-Bond Formation toward Multifunctional Products. *ACS Catalysis* (2016) doi:10.1021/acscatal.6b00758.
- [75] Partyka, D. V. Transmetalation of unsaturated carbon nucleophiles from boron-containing species to the mid to late d-block

metals of relevance to catalytic C-X coupling reactions (X = C, F, N, O, Pb, S, Se, Te). *Chemical Reviews* (2011) doi:10.1021/cr1002276.

[76] Ren, T. Peripheral covalent modification of inorganic and organometallic compounds through C-C bond formation reactions. *Chem. Rev.* (2008) doi:10.1021/cr8002592.

[77] Souillart, L. & Cramer, N. Catalytic C-C Bond Activations via Oxidative Addition to Transition Metals. *Chem. Rev.* (2015) doi:10.1021/acs.chemrev.5b00138.

[78] Negishi, E. I. & Anastasia, L. Palladium-catalyzed alkyne alkylation. *Chem. Rev.* (2003) doi:10.1021/cr020377i.

[79] Zhang, C., Chen, B. Q., Li, Z. Y., Xia, Y. & Chen, Y. G. Surface Plasmon Resonance in Bimetallic Core-Shell Nanoparticles. *J. Phys. Chem. C* (2015) doi:10.1021/acs.jpcc.5b04232.

[80] Lee, S., Jang, H. J., Jang, H. Y., Kim, S. K. & Park, S. Component conversion from pure Au nanorods to multiblock Ag-Au-Ag nanorods assisted by Pt nanoframe templates. *Nanoscale* (2016) doi:10.1039/c6nr03484e.

[81] Howes, P. D., Chandrawati, R. & Stevens, M. M. Colloidal nanoparticles as advanced biological sensors. *Science* (2014) doi:10.1126/science.1247390.

[82] Gu, J., Zhang, Y. W. & Tao, F. Shape control of bimetallic nanocatalysts through well-designed colloidal chemistry approaches. *Chem. Soc. Rev.* (2012) doi:10.1039/c2cs35184f.

[83] Cao, Y. W. C., Jin, R. & Mirkin, C. A. Nanoparticles with Raman spectroscopic fingerprints for DNA and RNA detection. *Science* (80-.). (2002) doi:10.1126/science.297.5586.1536.

[84] Cao, Y. C., Jin, R., Nam, J. M., Thaxton, C. S. & Mirkin, C. A. Raman Dye-Labeled Nanoparticle Probes for Proteins. *J. Am. Chem. Soc.* (2003) doi:10.1021/ja0366235.

[85] Yuan, X., Dou, X., Zheng, K. & Xie, J. Recent Advances in the Synthesis and Applications of Ultrasmall Bimetallic Nanoclusters. *Particle and Particle Systems Characterization* (2015) doi:10.1002/ppsc.201400212.

- [86] Shang, L., Dong, S. & Nienhaus, G. U. Ultra-small fluorescent metal nanoclusters: Synthesis and biological applications. *Nano Today* (2011) doi:10.1016/j.nantod.2011.06.004.
- [87] Ganguly, M., Jana, J., Pal, A. & Pal, T. Synergism of gold and silver invites enhanced fluorescence for practical applications. *RSC Advances* (2016) doi:10.1039/c5ra26430h.
- [88] Bruno, L.; Scuderi, M.; Priolo, F.; Falciola, L.; Mirabella, S. Enlightening the Bimetallic Effect of Au@Pd Nanoparticles on Ni Oxide Nanostructures with Enhanced Catalytic Activity. *Scientific Reports* (2023), doi: 10.1038/s41598-023-29679-6.
- [89] Park, S. et al. Enhanced H₂S gas sensing performance of networked CuO-ZnO composite nanoparticle sensor. *Mater. Res. Bull.* (2016) doi:10.1016/j.materresbull.2016.02.011.
- [90] Zhang, J. et al. Porous bimetallic Mo-W oxide nanofibers fabricated by electrospinning with enhanced acetone sensing performances. *J. Alloys Compd.* (2019) doi:10.1016/j.jallcom.2018.11.269.
- [91] Fan, F. et al. Hydrogen sensing properties of Pt-Au bimetallic nanoparticles loaded on ZnO nanorods. *Sensors Actuators, B Chem.* (2017) doi:10.1016/j.snb.2016.11.025.
- [92] Su, P. G. & Yu, J. H. Enhanced NO₂ gas-sensing properties of Au-Ag bimetal decorated MWCNTs/WO₃ composite sensor under UV-LED irradiation. *Sensors Actuators, A Phys.* (2020) doi:10.1016/j.sna.2019.111718.

Chapter 2

Synthesis of mono and bi-metallic nanoparticles

Content

Chemical reduction of noble metal nanoparticles	35
Au nanoparticles synthesis with trisodium citrate	35
Au, Pd and Pt monometallic nanoparticles with ascorbic acid	37
Au@Pd (core@shell) bimetallic nanoparticles	40
Conclusions	42
References	43

Summary

The concept of building up decorated systems is emerging as a methodology to add new functionalities maintaining the properties of the individual components. The surface of nanostructures has a crucial role in determining the electrical and optoelectronic properties of nano-devices. As the surface-to-volume ratio is very high, the surface states also play a key role on optical absorption, gas sensing, luminescence and other properties. Recently, heterostructures composed of different semiconductor oxides have been found to significantly enhance the response during sensing. In this regard, design, and preparation of composites with unique heterostructures will be increasingly important in the development of high performance nanodevices.

2.1 Chemical reduction of metal nanoparticles

In this section different synthesis methods for the preparation of mono- and bi-metallic NPs are proposed. The main advantage of these techniques is that it is not necessary to reach high temperatures (the process takes place at room temperature). Furthermore, the number of reactants is reduced to two, the metal precursor and the reducing agent (trisodium citrate and ascorbic acid in our case). The variation in concentration of one of these two parameters (dissolved in aqueous solution) has a strong impact on the average size of the NPs and, indirectly, on their physical and catalytic properties.

2.2.1 Au nanoparticles synthesis with trisodium citrate

A first method to synthesize Au NPs is the modified Turkevich method [22-25]. Through this procedure it is possible to obtain Au NPs at room temperature, without any correction of the pH of the solution (see Supplementary Information). Gold chloride trihydrate ($\text{HAuCl}_4 \cdot 3\text{H}_2\text{O}$, Sigma-Aldrich, St. Louis, MO, USA, $\geq 99.9\%$) and trisodium citrate ($\text{Na}_3\text{C}_6\text{H}_5\text{O}_7 \cdot \text{H}_2\text{O}$, Sigma-Aldrich St. Louis, MO, USA) are used without further purification.

The same quantities (50 mL) of 1mM gold chloride trihydrate and 3mM trisodium citrate are mixed in a beaker covered by a glass plate. During stirring the solution color shows a transient color change (from transparent to dark grey) and becomes stable in 2-3 h. After 24 hours, it shows the typical red wine color.

The solution is then stored at 4-8°C without any further preparation.

The NPs have a quite uniform diameter of about 20 ± 3 nm, as measured by SEM images on more than 200 NPs dispersed on a flat Si substrate. A STEM picture of a representative Au nanoparticle is shown in Figure 2.1(a). Each nanoparticle has a rounded-like shape with some bump due to the crystalline grains that make it up. STEM in Figure 2.2(b) shows that these AuNPs exhibit highly polycrystalline structures with grain size down to 10 nm. Indeed, the higher magnification insets of Figure 2.2(b) show different crystallographic orientations arising from different grains composing the NP.

The presence of Au nanoparticle within the colloidal solution produced with the modified-Turkevich method was checked with UV-vis spectroscopy (Figure 2.2(c)). Absorbance spectrum shows a narrow and sharp peak (centered at around 530 nm) which is a clear indication of the presence of NPs in colloidal form [24]. NPs solutions results stable over

prolonged time as confirmed by absorbance analyses performed on the as prepared solution and after two months from the preparation (dashed line in Figure 2.2(c)).

The main advantages of this synthesis method are:

- No temperature or pH dependence,
- High stability of the solution,
- Low toxicity of reagents,
- Uniform size of Au NPs,
- No influence of the substrate on the morphology

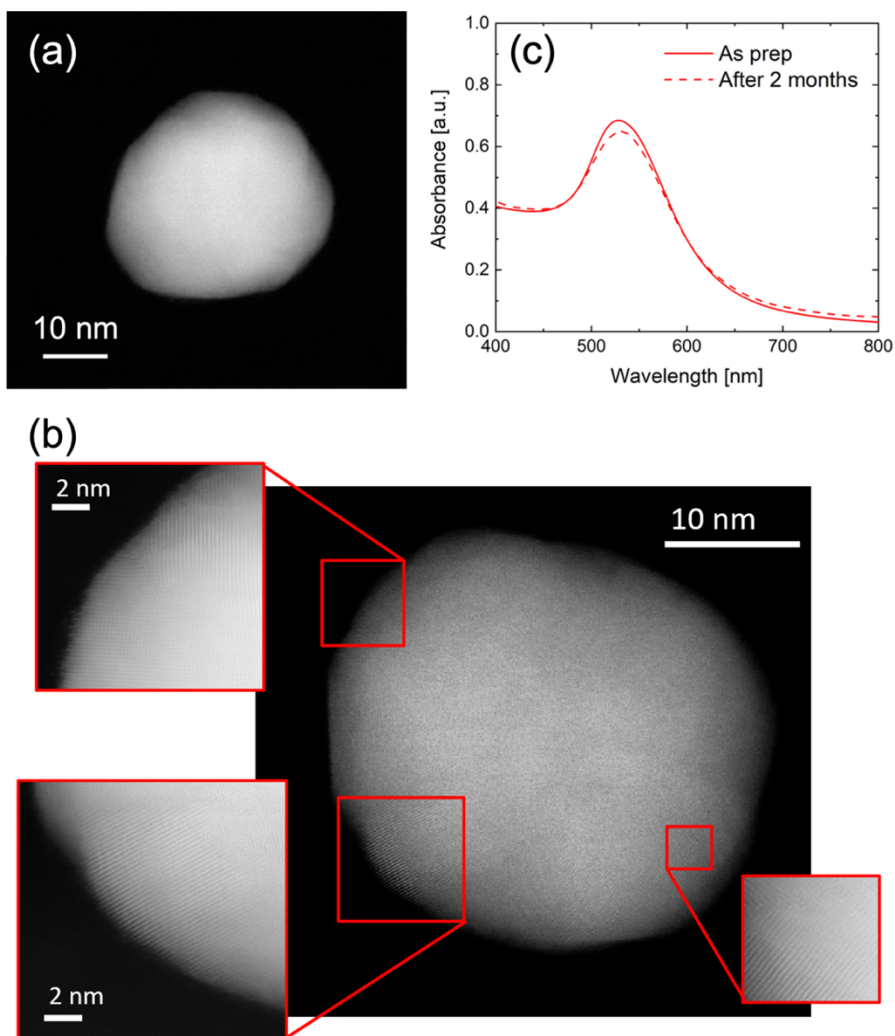


Figure 2.1: (a) STEM images of an Au NP; (b) STEM micrograph and high magnification insets of an isolated Au NP; (c) Absorbance spectrum of Au NPs solution as prepared (*As prep*) and after 2 months [25].

2.2.1 Au, Pd and Pt monometallic nanoparticles with ascorbic acid

Dispersions containing metal monometallic (Au, Pd, and Pt) NPs can be also produced through a green chemical reduction method at room temperature using ascorbic acid (AA) as reducing agent [26], instead of the most common trisodium citrate [1-4]. The use of AA is justified by its water solubility, biodegradability, and low toxicity compared with other reducing agents, looking for a method that generates a great variety of metal NPs [5]. However, the studies reported using ascorbic acid as reducing agent show no great control over the size or polydispersity of the obtained NPs. The aim of this research work was to synthesize and control, average size and morphology of Au, Pd and Pt, and bimetallic NPs with a core-shell structure, from aqueous solutions of Au(III), Pt(II), and Pd(II) species through a soft-chemistry green method using ascorbic acid as a reducing agent.

Monometallic Au and Pd NPs are synthesized by adding 30 μL of 33mM AA in 30 mL of 0.12 mM HAuCl_4 (Sigma-Aldrich, St. Louis, MO, USA, $\geq 99.9\%$) and 0.9 mM PdCl_2 (Sigma-Aldrich, St. Louis, MO, USA, $\geq 99.9\%$) aqueous solutions, respectively [6]. Pt NPs dispersion was produced by dispersing 30 μL of 33 mM AA in 30 mL of 0.2 mM H_2PtCl_6 (Sigma-Aldrich, St. Louis, MO, USA, $\geq 99.9\%$) aqueous solution [7,8]. The solutions were stirred for 5 minutes. All dispersions can be used without any further cleaning. The presence of NPs within the colloidal dispersion was checked with UV-vis spectroscopy.

Au nanoparticles

Scanning transmission electron microscopy (STEM) image and relative EDX spectrum of a metal NP dispersed on a TEM grid are shown in Figure 2.2(a-b). Au NPs have a rounded-like shape with a quite uniform diameter of about (20 ± 3) nm and a crystalline structure quite similar to that found on Au NPs synthesized with the modified Turkevich method, with some bumps all around the surface due to different grains composing the NP (inset of Figure 2.2(a)) [9]. Au absorbance spectrum (Figure 2.2(c)) shows a narrow and sharp plasmonic peak (530 nm) which is a clear indication of the presence of stable NPs in colloidal form [3].

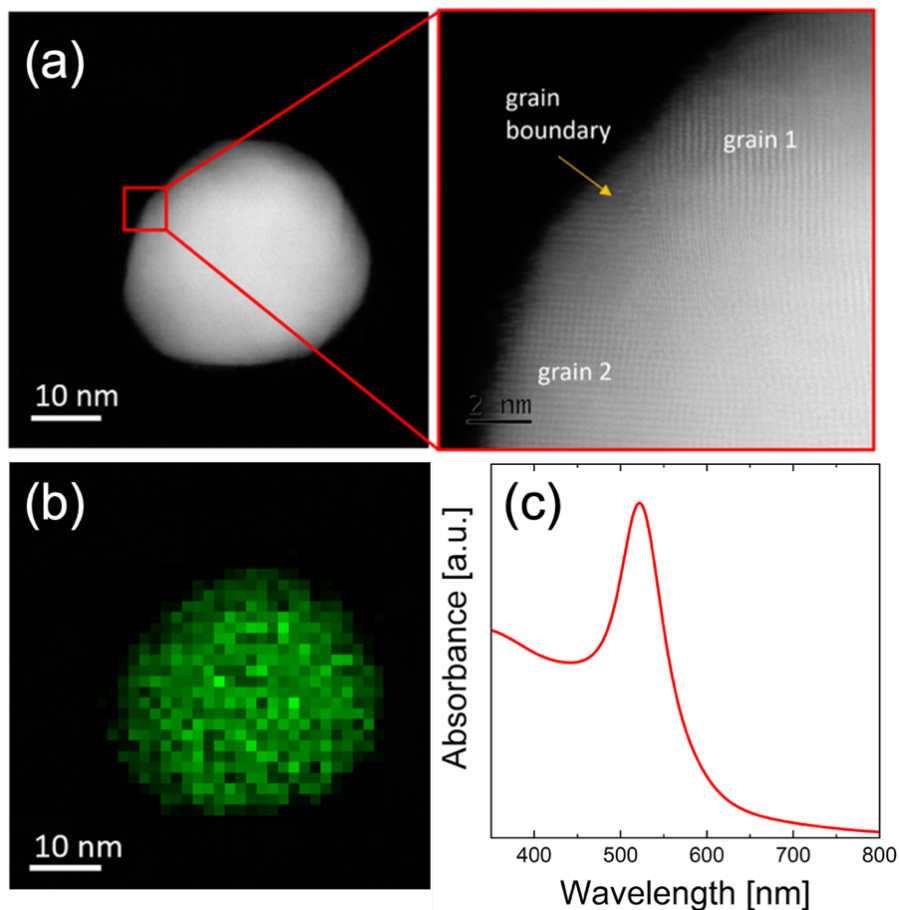


Figure 2.2: (a) STEM image and (b) EDX elemental map of a single Au NP dispersed on a TEM grid (grain boundary magnification in the inset); (c) absorbance spectrum of Au Pt colloidal dispersion obtained with trisodium citrate.

Pd nanoparticles

Pd NPs also show a spherical shape with size ranging from few to hundreds of nanometers (Figure 2.3(a)). Despite this shape, the clear and ubiquitous presence of small Pd grains (Figure 2.3(b)) tells us that Pd NPs are always composed of these very small grains. Also in this case, EDX elemental map (Figure 2.3(c)) and absorbance spectrum (Figure 2.3(d)) help us to univocally characterize our NPs and colloidal solution. No absorbance peak can be observed in the case of Pd colloidal solution: it is known that colloidal dispersions of Pd NPs synthesized with AA do not exhibit a well-defined absorption band [5].

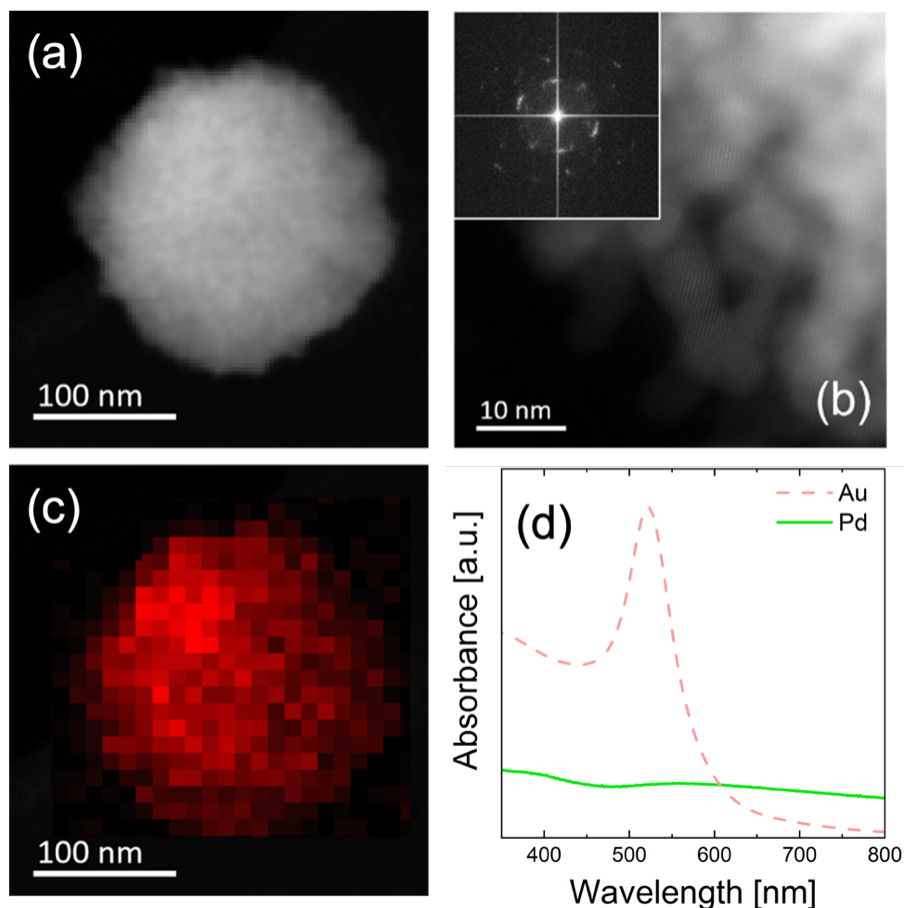


Figure 2.3: (a) STEM image, (b) small grains magnification, and (c) EDX elemental map of a single Pt NP dispersed on a TEM grid; (d) absorbance spectrum of Au Pt colloidal dispersion obtained with trisodium citrate.

Pt nanoparticles

Finally, Pt NPs synthesized with AA through our procedure show smaller mean size (2 nm) if compared with the other metal NPs obtained with the same procedure (Figure 2.4(a)). Also in this case, absorbance spectrum (Figure 2.4(b)) does not show any absorbance band, similarly to Pt NPs solution case [5,7,8].

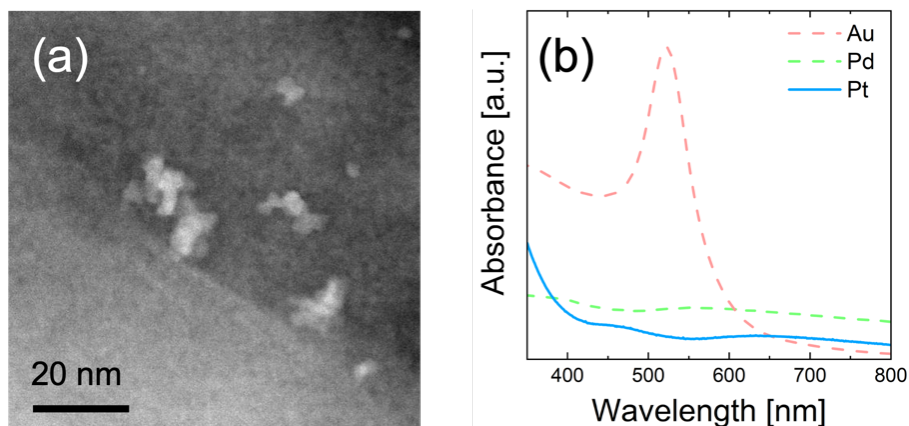


Figure 2.4: (a) STEM image Pt NPs; (d) absorbance spectra of Pt colloidal dispersion.

2.2.2 Au@Pd (core@shell) bimetallic nanoparticles

A similar method of what previously described can be used to synthesize bimetallic nanoparticles, only using ascorbic acid as reducing agent and the metal precursors.

The synthesis of bimetallic Au@Pd NPs is shown in Figure 2.5(a). 10 mL of Au NPs colloidal solution (obtained with the above-described method) and 30 mL of PdCl₂ aqueous solution were mixed with 50 μL of AA (Sigma-Aldrich, St. Louis, MO, USA) and stirred for 5 minutes [10]. The dispersions were used without any further cleaning.

The presence of Au@Pd NPs within the colloidal dispersion was checked with UV-vis spectroscopy (Figure 2.5(b)) [1,5,11]. The typical Au peak at 530 nm (Figure 2.1 and 2.2) is drastically reduced compared with the case of monometallic Au NPs because of the contemporary presence of both Au and Pd. This evidence remarks that Au atoms are confined in the core of the NPs whereas Pd atoms are on the surface [12,13].

RBS analyses (Figure 2.5(c)) confirm the presence of Au (peak at 1.8 MeV) and Pd (peak at 1.7 MeV) onto Si as expected. RBS was used to confirm the effective presence of bimetallic NPs after the decoration of a flat Si substrate, since Au and Pd amounts are proportional to the peak area [6] (RBS spectra of Au and Pd monometallic NPs on Si are reported for comparison). In the case of Au@Pd NPs, the amount of Au and Pd is $7.0 \cdot 10^{15}$ at cm⁻² and $1.6 \cdot 10^{15}$ at cm⁻², respectively. The spread in the width of the peaks indicates the presence of 3D agglomerates of NPs onto the surface with a NP mean size higher than those of mono-metallic case.

STEM pictures and EDX color maps of representative Au@Pd NP are shown in Figure 2.5(d-e). STEM image of Au@Pd NPs reveals a core-shell structure with a Au core (~ 25 nm) and Pd shell (~ 10 nm) made of smaller Pd clusters (Figure 2.5(d)). This result is confirmed with STEM EDX spectroscopy data. Indeed, the corresponding line-scan of Figure 2.5(f) shows clear evidence of the core-shell configuration.

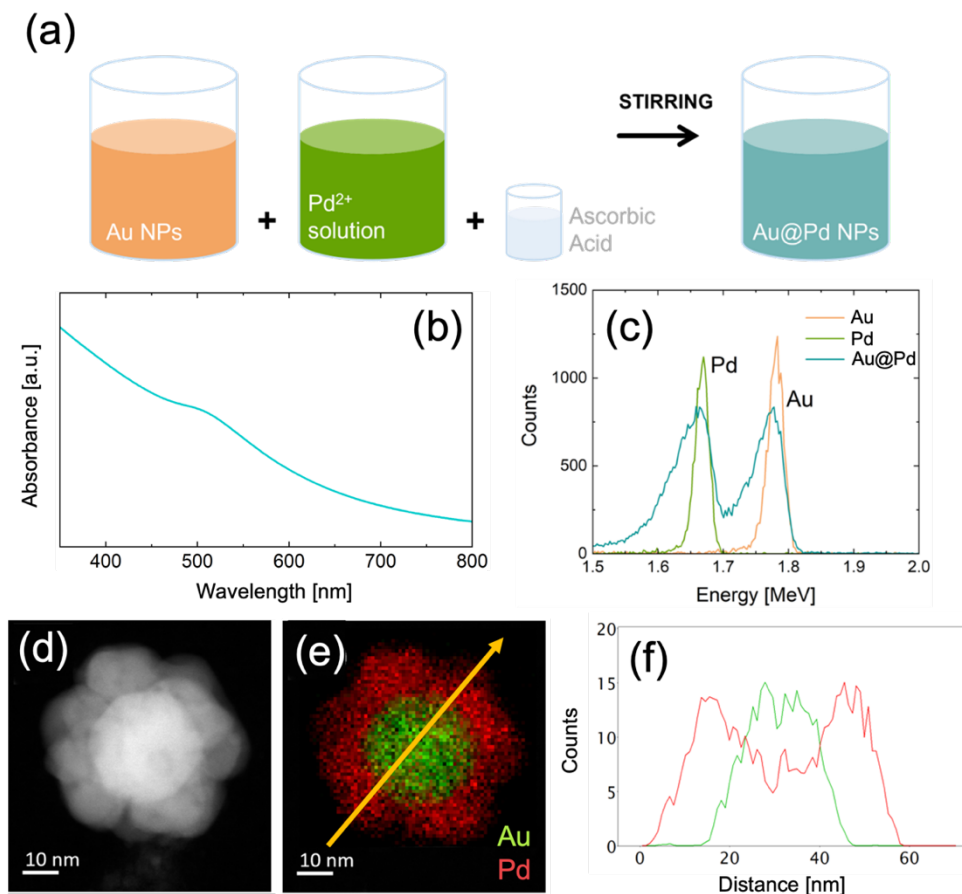


Figure 2.5: (a) Schematic representation of Au@Pd core-shell NPs synthesis; (b) absorbance spectrum of Au@Pd NPs dispersion; (c) RBS spectra of Au, Pd and Au@Pd NPs on Si substrate; (d) STEM image of an Au@Pd (core@shell) bimetallic nanoparticle; (e) EDX elemental maps of an Au@Pd NP with the corresponding (f) EDX lines scan (Pd red line and Au green line) showing the core shell structure [Adapted from 6].

3.4 Conclusions

In conclusion, we demonstrated reliable and cost-efficient methods for preparing mono- and bi-metallic nanoparticles. Nanoscale noble metal nanoparticles decorating the surfaces of the nanostructures significantly affect the electrocatalytic and electrical properties of the samples. In the next chapters we will see some examples of decorated nanostructures used for different applications. The effect of the decoration will be investigated in terms of carrier concentration, energy band bending of the supporting semiconductor and sensing properties of the electrodes.

References

- [1] Turkevich, J.; Stevenson, P.C.; Hillier, J. A study of the nucleation and growth processes in the synthesis of colloidal gold. *Discuss. Faraday Soc.* 1951.
- [2] Frens, G. Controlled Nucleation for the Regulation of the Particle Size in Monodisperse Gold Suspensions. *Nat. Phys. Sci.* 1973, doi:10.1038/physci241020a0.
- [3] Tyagi, H.; Kushwaha, A.; Kumar, A.; Aslam, M. A Facile pH Controlled Citrate-Based Reduction Method for Gold Nanoparticle Synthesis at Room Temperature. *Nanoscale Res. Lett.* 2016, doi:10.1186/s11671-016-1576-5.
- [4] Bruno, L.; Strano, V.; Scuderi, M.; Franzò, G.; Priolo, F.; Mirabella, S. Localized Energy Band Bending in ZnO Nanorods Decorated with Au Nanoparticles. *Nanomaterials* 2021, doi:10.3390/nano11102718.
- [5] Larios-Rodríguez, E. A., Castellón-Barraza, F. F., Borbón-González, D. J., Herrera-Urbina, R. & Posada-Amarillas, A. Green-Chemical Synthesis of Monodisperse Au, Pd and Bimetallic (Core–Shell) Au–Pd, Pd–Au Nanoparticles. *Adv. Sci. Eng. Med.* 5, 1-8 (2013) doi:10.1166/ asem.2013.1354.
- [6] Bruno, L.; Scuderi, M.; Priolo, F.; Falciola, L.; Mirabella, S. Enlightening the Bimetallic Effect of Au@Pd Nanoparticles on Ni Oxide Nanostructures with Enhanced Catalytic Activity. *Scientific Reports* 2023, doi:10.1038/s41598-023-29679-6.
- [7] Battiato S, Bruno L, Terrasi A, Mirabella S. Superior Performances of Electroless-Deposited Ni-P Films Decorated with an Ultralow Content of Pt for Water-Splitting Reactions. *ACS Appl Energy Mater* 2022. <https://doi.org/10.1021/acsaem.1c03880>.
- [8] Bruno, L.; Battiato, S.; Scuderi, M.; Priolo, Terrasi, A.; Mirabella, S. Physical Insights into Alkaline overall water splitting with NiO Microflowers Electrodes with ultra-low amount of Pt catalyst. *Int. J. of Hydr. En.* 2022, doi: 10.1016/j.ijhydene.2022.08.005.

- [9] Liu, W. *et al.* Pt and Au bimetallic and monometallic nanostructured amperometric sensors for direct detection of hydrogen peroxide: Influences of bimetallic effect and silica support. *Sensors Actuators, B Chem.* 2018, <https://doi.org/10.1016/j.snb.2017.08.123>.
- [10] Eteya, M. M., Rounaghi, G. H. & Deiminiat, B. Fabrication of a new electrochemical sensor based on Au–Pt bimetallic nanoparticles decorated multi-walled carbon nanotubes for determination of diclofenac. *Microchem. J.* 2019 <https://doi.org/10.1016/j.microc.2018.09.009>.
- [11] Dutta, S. *et al.* Facile Synthesis of Bimetallic Au-Pt, Pd-Pt, and Au-Pd Nanostructures: Enhanced Catalytic Performance of Pd-Pt Analogue towards Fuel Cell Application and Electrochemical Sensing. *Electrochim. Acta* 2015 <https://doi.org/10.1016/j.electacta.2015.09.062>.
- [12] Jiao, J. *et al.* An ultrasensitive non-enzymatic sensor for quantitation of anti-cancer substance chicoric acid based on bimetallic nanoalloy with polyetherimide-capped reduced graphene oxide. *Nanomaterials* 2020 <https://doi.org/10.3390/nano10030499>.
- [13] Chen, T. *et al.* Controlled synthesis of Au@Pd core-shell nanocomposites and their application for electrochemical sensing of hydroquinone. *Talanta* 2019, doi: 10.1016/j.talanta.2019.01.094.

Chapter 3

Localized energy band bending in Au decorated ZnO nanorods

Content

Au nanoparticle decoration of ZnO nanorods	47
Materials and Methods	49
Synthesis and decoration of ZnO nanorods	49
Characterization	49
Materials characterization	50
Photoluminescence and Cathodoluminescence	52
Mott-Schottky analysis	57
Modeling the Au NP decoration effect	58
Conclusions	61
References	62

Summary

In this chapter, the decoration of ZnO nanorods by means of Au nanoparticles is experimentally investigated and modelled in terms of energy band bending. ZnO nanorods were synthesized by chemical bath deposition. Photoluminescence and cathodoluminescence are used to exploit the decoration effect to different extents. Decoration with Au nanoparticles induces a 10 times reduction in free electrons below the surface of ZnO, together with a decrease in UV luminescence and an increase in visible-UV intensity ratio. Energy band modifications and carrier concentrations are also evaluated through electrochemical analyses and simulated using a multiphysics approach, revealing a noticeable halo effect in the electric field at the ZnO surface close to the edges of the Au NPs.

3.1 Au nanoparticle decoration of ZnO nanorods

Zinc oxide (ZnO) is an *n*-type semiconductor (band gap of 3.2–3.4 eV, large excitonic-binding energy of 60 meV) attracting great attention due to its physical and chemical properties [1,2]. One of the most intriguing aspects of ZnO is the possibility to easily grow many different nanoscale forms. Figure 3.1 (a-g) reports a collection of ZnO nanostructures: nanobelt, nanowires, nanotubes, nanopropellers, nanorods, and hierarchical nanostructures.

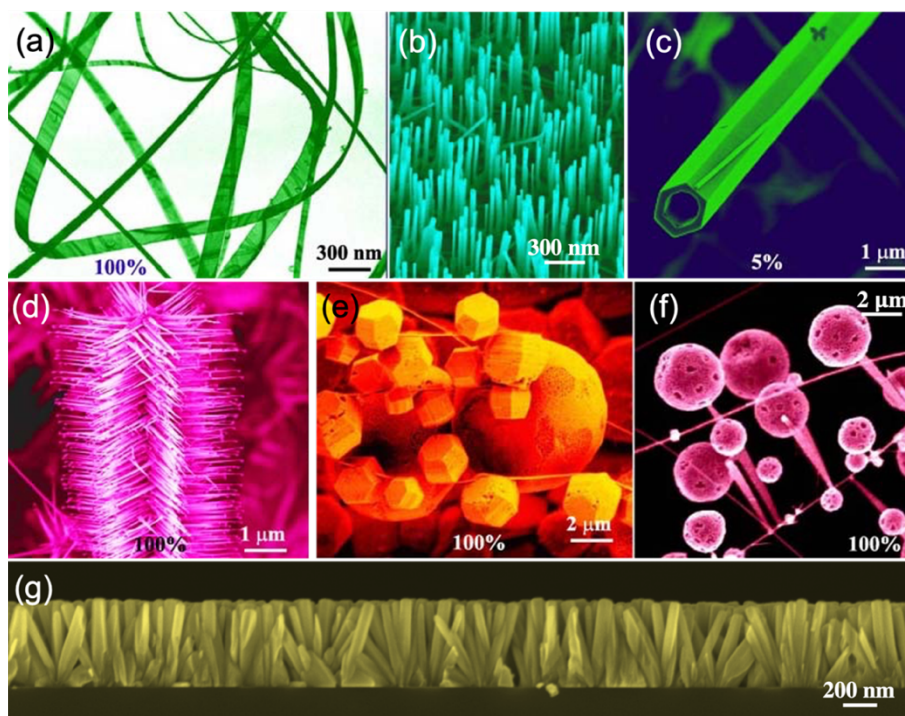


Figure 3.1: A collection of novel nanostructures of ZnO: (a) Nanobelt; (b) aligned nanowire arrays; (c) nanotubes; (c) array of propellers; (d) mesoporous nanowires; (e) cages and shell structures; (f) hierarchical shell; (g) nanorods [adapted from 2].

In particular, ZnO nanorods (NRs) have proven to be promising nanostructures for a wide range of applications, especially for photonics and optoelectronics in the UV or blue spectral range [3–9].

A controlled improvement of performance needs a microscopic understanding of ZnO surface states and deep levels, especially in low-dimensional nanostructures where the significant surface-to-bulk ratio significantly impacts electronic energy band bending.

The surface decoration of semiconductor nanostructures with metallic nanoparticles (NPs) usually leads to an improvement of their catalytic and electrical properties [10–14]. The formation of nano-Schottky junctions at the metal–semiconductor interface leads to the creation of a strong electric field directed toward the surface and to a significant modification of the ZnO NRs energy band profiles [15–19]. As a consequence, space charge regions and surface-localized electric fields promote a catalytic effect and modify the radiative recombination process.

Apart from near-band-edge emission, ZnO nanostructures may also exhibit luminescence in the visible range [1,20–27], as shown in Figure 3.2(a). There is a general consensus in attributing the UV emission to the radiative transition from the free donor exciton states below the conduction band minimum to the valence band maximum, while visible emission is ascribed to the transitions from defect states inside the energy band gap (Figure 3.2(b)).

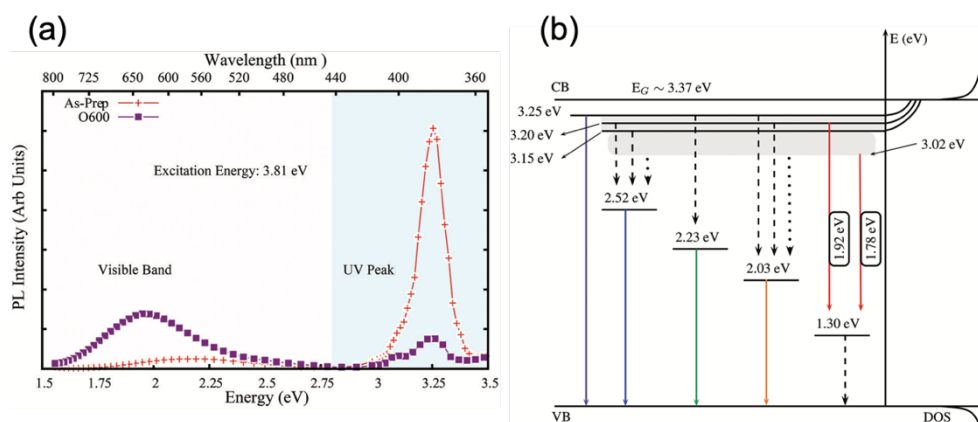


Figure 3.2: (a) Photoluminescence spectrum for ZnO NRs before and after thermal process (annealing in oxygen atmosphere); (b) Model for the photoluminescence emission of ZnO NRs with an excitation at 3.81 eV [adapted from 28].

When decorated, luminescence from ZnO NRs changes, with an enhancement of visible emission at the expense of UV emission [10,19,28,29]. Such a process could be the consequence of a significant bending of electronic energy bands into ZnO just below the metal nanoparticle, inducing free carrier depletion. Such an effect in decorated ZnO nanorods allows the application of these composite materials in UV sensing and light-induced catalysis [11,16,18,19,31,32].

3.2 Materials and Methods

3.2.1 Synthesis and decoration of ZnO nanorods

ZnO NRs used in our study have been previously synthesized through chemical bath deposition (CBD) on Si substrates cut by Czochozralski (Cz) wafers. Zinc nitrate hexahydrate and hexamethylenetetramine were used for the growth of ZnO NRs with concentrations of 25 mM and 50 mM, respectively [33].

Au NPs were synthesized through the modified Turkevich method [34–36] at room temperature, without any correction of the pH of the solution (see Chapter 2 for details).

ZnO NRs were decorated via dip coating by simply immersing different substrates in the Au NP colloidal solution. Decorated samples are labelled according to the number of immersions in the solution (e.g., Au₅-ZnO refers to a ZnO NR immersed 5 times into Au NP solution).

3.2.2 Characterization

UV-vis spectroscopy was performed on the Au solution using a Varian Cary 500 (Agilent Technologies, Santa Clara, CA, USA) double beam scanning UV/VIS/NIR spectrophotometer.

Surface morphology was analyzed by using a Scanning Electron Microscope (Gemini field emission SEM Carl Zeiss SUPRA 25, FEG-SEM, Carl Zeiss Microscopy GmbH, Jena, Germany). SEM images were analyzed using ImageJ software [37].

Transmission electron microscopy (TEM) analyses of Au NPs dispersed on a TEM grid were performed with a Cs-probe-corrected JEOL JEM ARM200F microscope at a primary beam energy of 200 keV operated in scanning TEM (STEM) mode.

The amount of Au loading onto ZnO NRs was evaluated by Rutherford backscattering spectrometry (RBS, 2.0 MeV He⁺ beam at normal incidence) with a 165° backscattering angle using a 3.5 MV HVEE Singletron accelerator system (High Voltage Engineering Europa, The Netherlands). RBS spectra were analyzed using XRump software [38].

Photoluminescence (PL) measurements were performed by pumping at ~0.7 mW the 325 nm (3.81 eV) line of a He–Cd laser chopped through an acousto-optic modulator at a frequency of 55 Hz. The PL signal was analyzed using a single grating monochromator, detected with a Hamamatsu visible photomultiplier, and recorded with a lock-in amplifier using the acousto-optic modulator frequency as a reference. PL spectra

were taken in air or vacuum within a cryostat ($\sim 10^{-6}$ mbar) to ascertain the role of atmospheric O₂. All PL spectra were converted by Jacobian transformation from wavelength to energy dispersion [39].

Cathodoluminescence (CL) measurements were performed using a Scanning Electron Microscope (Gemini field emission SEM Carl Zeiss SUPRA 25, FEG-SEM, Carl Zeiss Microscopy GmbH, Jena, Germany), equipped with a Gatan MonoCL3 CL spectroscopy/imaging system. The beam energy was varied between 2 and 20 keV, providing different probe depths below the surface as determined by *CASINO* simulations [40]. All CL spectra were corrected for the overall detection response of the system. Electrochemical measurements were carried out at room temperature by using a VersaSTAT 4 potentiostat (Princeton Applied Research, Oak Ridge, TN, USA) and a three- electrode setup with a platinum counter electrode, a saturated calomel electrode (SCE) as reference electrode, and the samples as working electrodes. An amount of 0.5 M Na₂SO₄ (Sigma Aldrich, St. Louis, MO, USA, $\geq 85\%$) was used as a supporting electrolyte. Mott– Schottky (M-S) analyses were conducted on bare and decorated ZnO NRs samples in the potential range $-1 \div 0$ V vs. SCE, at 1000 Hz frequency.

A simulation of the band position of the semiconductor and the electric field on the surface of ZnO NRs induced by the metal decoration has been carried out by *COMSOL Multiphysics® software* (v.5.0, COMSOL Inc., Stockholm, Sweden) [41].

3.3 Materials characterization

The CBD grown ZnO nanorods are shown in Figure 3.3(a-c). A uniform nanostructured film made of ZnO NRs onto Si can be seen in low magnification SEM image in Figure 3.3(a). ZnO NRs present a width of around 100 nm and a length of 700 nm (Figure 3.3(b-c)). The effective decoration of ZnO NRs with metal NPs can be appreciated in Figure 3.3(d), showing ZnO NRs with the surface densely decorated by Au NPs after 20 immersion (inset of Figure 3.3(d)).

RBS analyses (Figure 3.4(a)) confirm the presence of a small amount of Au (peak at 1.8 MeV) and Zn (large peak at 1.0-1.5 MeV) onto Si (signal from 0.6 MeV downward), as expected. RBS was used to perform a quantitative measurement of Au after multiple immersion, since the Au amount is proportional to the Au peak in the spectrum [19].

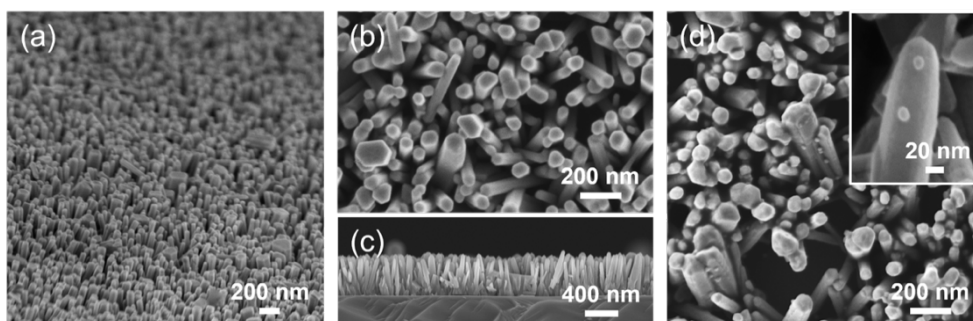


Figure 3.3: (a) Tilted SEM images of bare ZnO NRs; (b) magnified SEM image of ZnO NRs and (c) cross section SEM image of ZnO nanostructured film; (d) SEM images at different magnification of Au₂₀-ZnO.

Figure 3.4(b) shows the variation of Au amount with number of immersions, showing a fairly linear increase from 1.0×10^{14} at cm^{-2} (after 1 immersion) to 4.7×10^{15} at cm^{-2} (after 20 immersions). As expected, Au amount on ZnO NRs increases with the number of immersions, allowing to carefully monitor the extent of decoration. We verified that the size of Au NPs does not change with the number of immersions, confirming that the synthesis method produces highly stable suspension of Au NPs [34, 36]. Our decoration method effectively covers the ZnO NRs surface with a varying density of Au NPs.

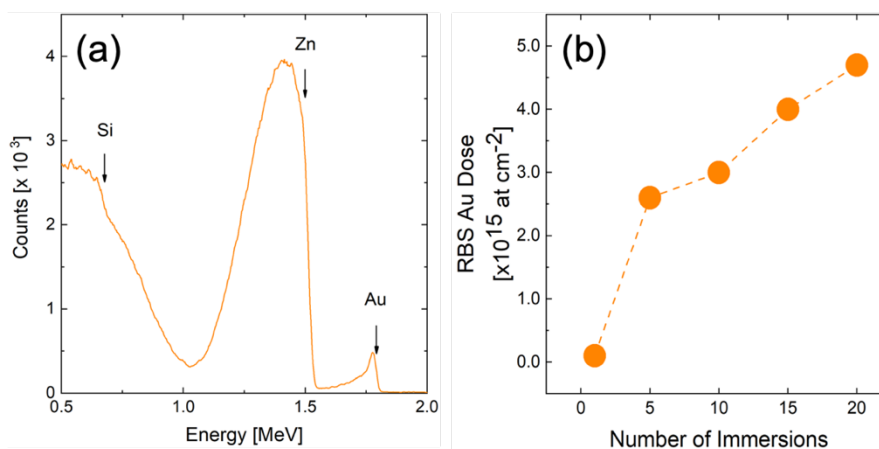


Figure 3.4: (a) RBS spectrum of the Au₂₀-ZnO sample; (b) variation of the Au loading on the surface of ZnO NRs as a function of the number of immersions.

The density of Au NP cannot be extracted by SEM analysis, because of the rough surface and shadowing effect.

Thus, the Au amount (D_{RBS} , obtained by RBS [42]) was joined with Au NP diameter to evaluate the density N of NPs decorating ZnO NRs, through the following relation:

$$D_{RBS} = N \rho_{at} V_{NP} \quad (3.1)$$

where ρ_{at} is the Au atomic bulk density ($5.9 \times 10^{22} \text{ at cm}^{-3}$) and V_{NP} is the volume of a single NP (cm^3) based on the measured size of NPs. The result of such an exercise shows that the NP density can be tuned from $1.0 \times 10^9 \text{ NPs cm}^{-2}$ to $4.5 \times 10^{10} \text{ NPs cm}^{-2}$ (from 1 up to 20 immersions).

3.4 Photoluminescence and Cathodoluminescence

PL spectra were acquired for both bare and decorated NRs in vacuum and in air (Figure 3.5). All the emission spectra (Figure 3.5(a)) consist of a narrow UV peak (2.7 – 3.5 eV) and a broader visible band (1.8 – 2.7 eV). Figure 3.5 reports the visible emission multiplied by a factor of 10 with respect to the UV emission. It is now well-assessed that UV peak arises from a very fast transition (timescale below 1 ns [42-49]) of free excitons from a donor state (FX-D) to valence band maximum (VBM) [51]. Visible emission is due to recombination between holes in VBM and electrons trapped at midgap levels induced by oxygen vacancy (V_o) or zinc vacancy (V_{zn}) [20, 51-54]. This process is much slower than that leading to UV emission, with characteristic time in the ns- μ s range [43, 45, 48, 50].

PL measurement in vacuum is aimed to disentangle the effect of atmospheric O_2 , as it is well assessed that oxygen adsorption onto ZnO NRs modifies the energy bands at surface [52]. Visible PL is scarcely affected by gold decoration or O_2 adsorption, still the UV radiative recombination of electron-hole in ZnO is clearly modified. The area of each peak in the PL spectra is related to the number of photons emitted in that energy range, so the ratio (N_{vis}/N_{UV}) between the areas of visible and UV peaks quantifies how many photons are emitted in the visible range per each photon emitted in the UV. Such a ratio indicates the relative probability of radiative recombination in the two channels, and its changes with surface condition are indicative of modification in the electron-hole recombination process. Figure 3.5(b) displays N_{vis}/N_{UV} increasing with Au NPs loading, both in air and in vacuum.

In addition, this ratio, as measured in air, is always higher than in vacuum. It is worth to note that Au decoration in vacuum gets the same effect (N_{vis}/N_{UV} increase from 0.11 to 0.13) of O_2 adsorption (without metal NPs). The largest visible-to-UV emission is got by joining the two effects on ZnO surface (O_2 adsorption and Au decoration). This unbalance between UV and visible emission will be later explained in terms of energy bands bending caused by nano Schottky junction at the metal-semiconductor interface.

The experimental results point out that Au NP decoration and O_2 surface adsorption show a similar effect on the radiative recombination, as they: (i) reduce the UV emission and slightly increase the visible one; (ii) produce a high energy tail in the visible emission spectrum.

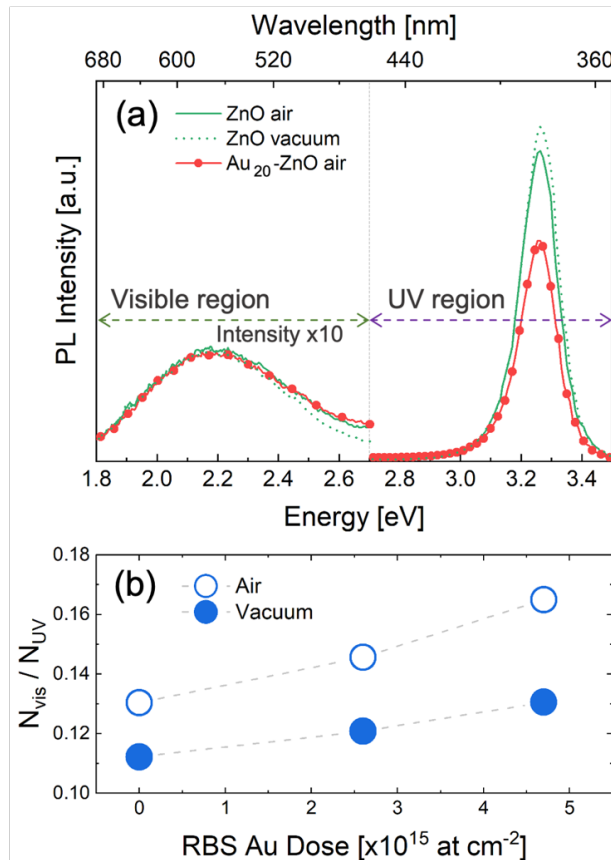


Figure 3.5: (a) PL spectra of bare ZnO (green continuous line) and Au₂₀-ZnO (red and dotter line) in air, and bare ZnO in vacuum (green dotted line), with visible emission multiplied by a factor of 10; (b) ratio between the intensity of visible (N_{vis}) and UV emission (N_{UV}) in air and in vacuum versus Au NPs decoration extent.

To further investigate the effect of ZnO NRs decoration with Au NPs, CL analyses were carried out on bare (ZnO) and decorated sample (Au₂₀-ZnO). CL spectra were acquired at different electron beam energies (E_0 , varied in the range 2-20 keV) and different beam current (using SEM aperture of 10, 30 and 60 μm).

CL spectra for bare ZnO and Au₂₀-ZnO at beam energy of 10 keV are reported in Figure 3.6(a). CL spectra show the emission from two different peaks, a sharp UV peak and a broad visible region (like in PL analysis). For Au₂₀-ZnO (red line in Figure 3.6), the absolute intensity of the two peaks significantly decreases compared to that of bare ZnO, probably because of shadowing effect by Au NPs in the decorated sample. CL spectra of bare ZnO acquired for different beam energy and current are reported in Figure 3.6(b). It is worth to note that as the beam energy increases both UV peaks and visible bands increase too.

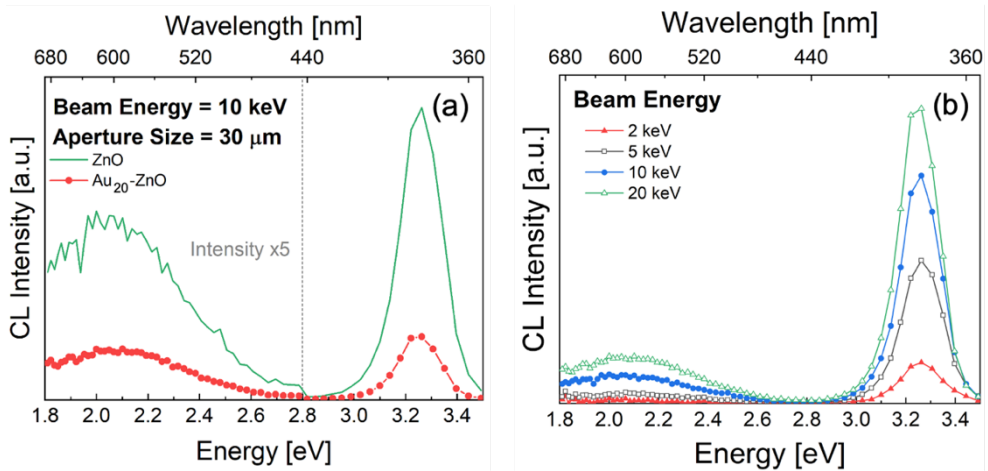


Figure 3.6: (a) CL spectra of bare ZnO (green) and Au₂₀-ZnO (red), with visible emission multiplied by a factor of 5; (b) CL spectra of bare ZnO at different electron beam energies.

The relationship between E_0 and the probe depth R is

$$R [\text{nm}] = \frac{27.6 A E_0^{1.67}}{\rho Z^{0.89}} \quad (3.2)$$

where ρ is the target material density (g cm^{-3}); Z and Z are, respectively, the target atomic number and atomic weight; and E_0 (keV) is the initial electron energy.

Information from CL at different energies can be calculated as a function of Kanaya-Okayama electron penetration depth [54] using Monte Carlo simulations of electron-solid interaction. As expected, when the beam energy is increased from 2 to 20 keV, the penetration depth (and so the probe depth) passes from few nm to around $2 \mu\text{m}$ [54-55].

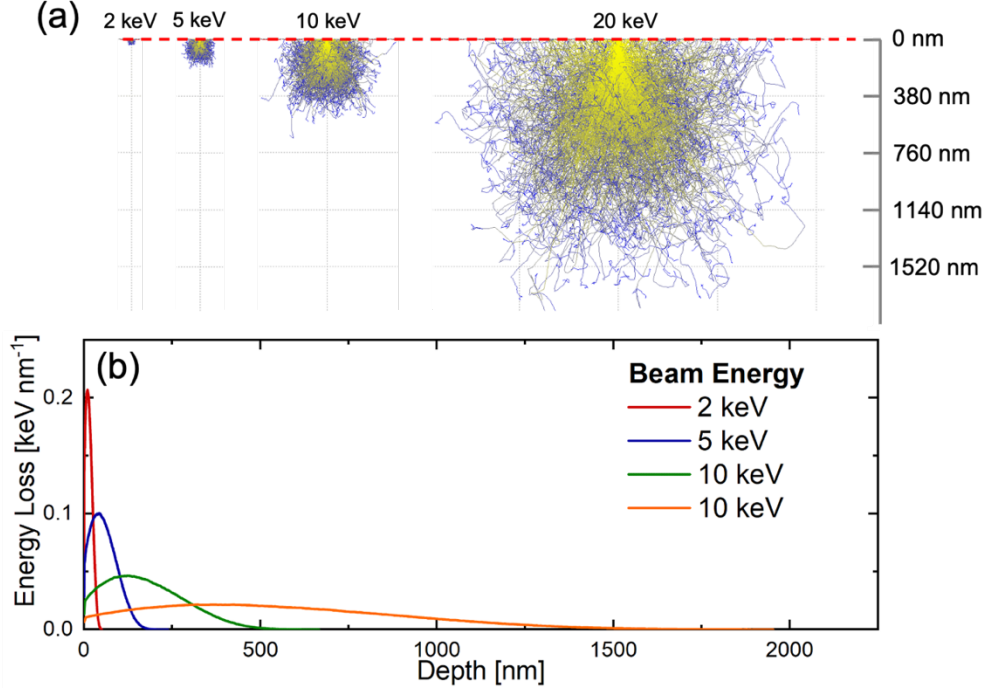


Figure 3.7: CASINO simulation of the variation of the (a) interaction volume and (b) energy loss in respect to beam energy variation.

Moreover, as the energy of the beam varies, it is possible to calculate the e-h generation rate (G_0) from the relationship [56]:

$$G_0 = 6.25 \times 10^{21} E_0 I_0 \frac{1 - \eta \bar{E}/E_0}{E_i} \quad (3.3)$$

where E_0 is the electron beam energy, I_0 is the electron beam current, η is the fraction of incident electron backscattered from Montecarlo simulations (~ 0.25), \bar{E} is the mean energy of backscattered electrons ($\sim 0.65 E_0$), and E_i is the ionization energy (related to the band gap of the material: $E_i = 2.8 E_g + M$, where $0 < M < 1$ depending on the material [56]).

As the beam energy increases, the probe depth increases too. The probe depths at different energies were simulated with Monte Carlo simulations through CASINO software [40, 57-59] (Figure 3.8), ranging from few tens of nanometers (at 2 keV) to 2 micrometers (at 20 keV). As a direct consequence, the generation of electron-hole pairs is diluted in a much larger volume, inducing a dramatic reduction of volumetric generation rate by 4 orders of magnitude.

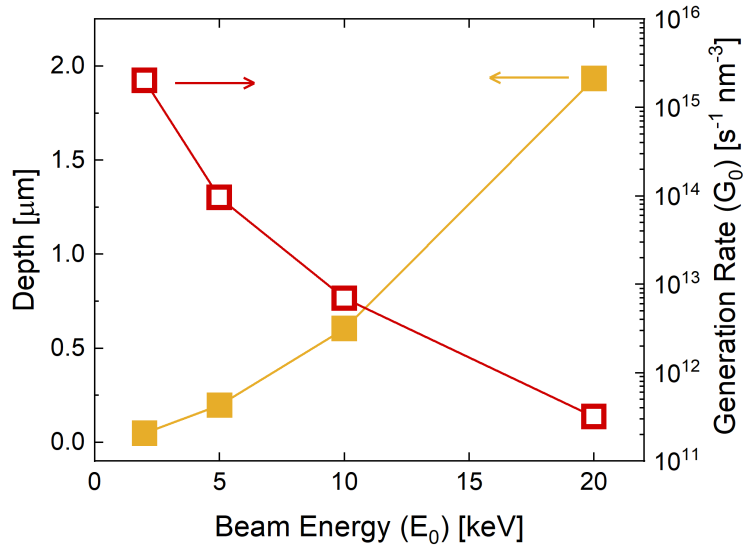


Figure 3.8: CASINO simulation of the probe depth (yellow) and e-h generation rate (red) of the electron beam at different beam energies.

Also in this case, as done for PL analysis, we evaluated the ratio between the visible and the UV emission. Figure 3.9(a-b) shows that N_{vis}/N_{UV} ratio increases with beam energy and decreases with beam current. As for PL, also in CL the presence of Au NPs gives a larger N_{vis}/N_{UV} ratio with respect to bare ZnO.

Moreover, N_{vis}/N_{UV} ratio increases at lower e-h pairs generation rates. Figure 3.9(b) clearly confirms this trend by varying the beam current without changing the probe depth. These results can be explained considering the different timescales of the two radiative recombination processes. The slow one (leading to visible emission) becomes weaker at high generation rate probably because the strong concentration gradient of e-h pairs induces a significant diffusion which reduces the recombination on long timescales.

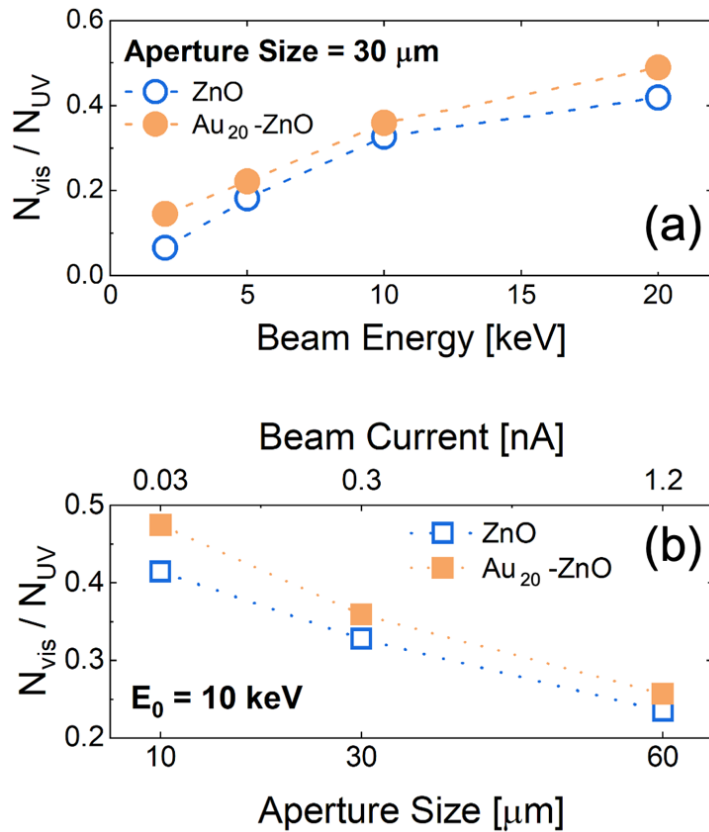


Figure 3.9: Ratio between the intensity of visible (N_{vis}) and UV emission (N_{UV}) as a function of the electron beam energy (b) and current (c).

3.5 Mott-Schottky analysis

In order to better understand the effect of Au decoration on energy bands and free carrier density, Mott-Schottky analysis was performed by immersing the bare and decorated ZnO NRs sample in an aqueous solution of Na_2SO_4 . Even if a liquid-semiconductor interface is now tested, we wish to extract information on the Au NPs decoration effects. ZnO and Au₂₀-ZnO samples have been characterized by measuring their capacitance as a function of electrode potential [60-65], and a typical result is shown in the Mott-Schottky plot (C^{-2} vs E) in Figure 3.10. The flat band potential E_{FB} and the donor density N_D can be obtained from the linear part of the plot as intercept with x -axis and slope, respectively (see Appendix A for details) [51-63, 65-68]. The plot appears to have a linear section in the potential range $-0.2 \div -0.45$ V vs SCE in the case of ZnO, and $-0.2 \div -0.6$ V vs SCE

for Au₂₀-ZnO sample. The flat band potentials obtained are -0.68 V and -0.85 V vs SCE for ZnO and Au₂₀-ZnO, respectively.

Concerning donor concentration, from Eq. (B3), we found values of $3.2 \times 10^{17} \text{ cm}^{-3}$ and $2.0 \times 10^{16} \text{ cm}^{-3}$ for bare and decorated samples, respectively. The flat band potential gives an indication of the band bending at liquid-semiconductor interface at equilibrium, and here we observe that such a bending is almost 0.2 eV larger in Au₂₀-ZnO and this is probably due to the Au NPs decoration. On the other hand, the reduction by one order of magnitude of the donor concentration in Au₂₀-ZnO confirms that Au NPs decoration effectively depletes the free carriers at the surface of the ZnO NRs.

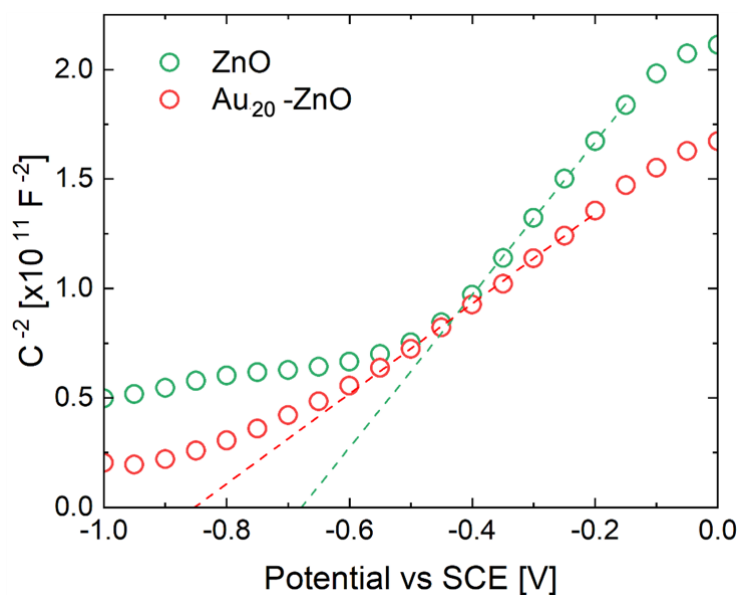


Figure 3.10: Mott-Schottky plot of ZnO and Au₂₀-ZnO in 0.5 M Na₂SO₄ (dashed lines represent the fits to linear regions).

3.6 Modeling the Au NP decoration effect

Au NPs decoration clearly affects the electronic energy band at ZnO, as largely shown in the previous section. We now try to quantify such an effect investigating the band bending at the metal-semiconductor interface through a Multiphysics approach.

To visualize the band modification in ZnO NRs decorated with metal NPs, *COMSOL* [40] simulations were performed assuming a single Au circular dot (20 nm large) placed onto ZnO in vacuum ambient (see Figure 3.11 for a scheme of simulation). The following parameters are used for ZnO [69]:

- relative dielectric permittivity $\epsilon_r = 8.3$;
- energy gap $E_g = 3.4$ eV;
- electron (hole) mobility $\mu_n = 0.01$ m²V⁻¹s⁻¹ ($\mu_p = 0.002$ m²V⁻¹s⁻¹);
- effective mass $m_{\text{eff,C}} = 0.28 m_0$ ($m_{\text{eff,V}} = 0.59 m_0$);
- electronic affinity $\chi_0 = 4.1$ eV;
- donor concentration $N_{D0} = 10^{18}$ cm⁻³.

At room temperature, the computed effective densities of states for electrons and holes are $N_C = 3.6 \times 10^{24}$ m⁻³ and $N_V = 1.1 \cdot 10^{25}$ m⁻³, while the effective Richardson constant for electrons is $A_n^* = 4\pi em_{\text{eff,C}} k^2/h^3 = 34$ A K⁻²cm⁻². At the unbiased Schottky contact the Fermi level of Au ($\Phi_{Au} = 4.8$ eV) and that of ZnO are aligned, leading to an energy barrier ($\Phi_B = 0.7$ eV) for electrons.

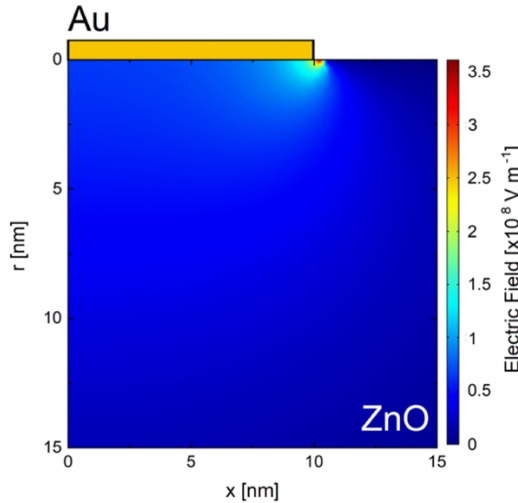


Figure 3.11: 2D *COMSOL* simulation of the electric field of a single ZnO NR in presence of a Au NP on its surface.

Band bending comes at metal-semiconductor junction because of different work functions. Au has a higher work function ($\Phi_{Au} = 4.8$ eV [70]) than that of ZnO ($\Phi_B = 4.2$ eV [71]), leading to a potential barrier for electrons and to a significant upwards bending of ZnO conduction and valence bands at the metal-semiconductor interface. The energy map of the conduction band minimum (CBM) as a function of depth and distance from NP center

is reported in Figure 3.12(a). The simulation neglects any surface defects or temperature dependence. The upward bending of CBM overcomes 0.6 eV beneath Au NP center and extends almost 20 nm within ZnO material. As a consequence, electron population in conduction band is largely affected. Moreover, a giant electric field arise under Au NP, pointing Au. The 2D map of electric field at ZnO surface below a circular Au dot is shown in Figure 3.12(b) showing intensity as high as 10^8 V m^{-1} with a characteristic halo effect beneath the Au NP circumference. The electric field is proportional to the spatial derivative of the CBM energy; thus, the highest electric field is found close to Au NP edges, creating this distinctive halo. Such a strong and localized electric field caused by Au decoration is extremely effective in modifying the band profile and carrier density close to the surface. Moreover, the halo effect can be responsible of catalytic effect at ZnO surface sites close to Au NP edges. To understand PL and CL data of ZnO NRs decorated with Au NPs, the radiative mechanism in ZnO NRs must be focused. As already said, UV emission is a fast process occurring a fraction of ns after the e-h generation, while visible emission involves mid-gap levels in a radiative recombination of e-h well slower than that causing UV one [43]. It has already been demonstrated that these levels are below the Fermi level [24, 72-73]. Thus, UV emission is expected to be affected by band bending much more than the visible one, as the first is related to shallow levels whose population largely depends on Fermi level position [19]. The presence of a high electric field caused by Au NP decoration (Figure 3.12(b)) could very effectively promote separation of generated charge carriers thus reducing the fast e-h recombination. This evidence could explain the increase of N_{vis}/N_{UV} ratio observed in the decorated samples (both in PL and in CL analyses).

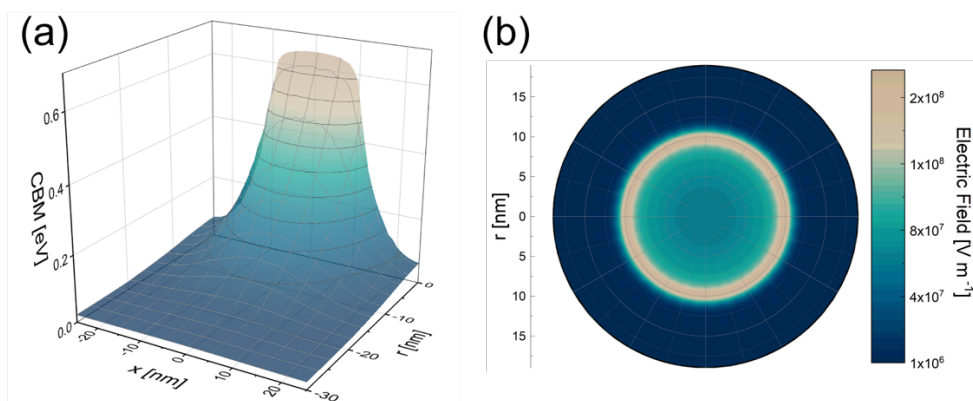


Figure 3.12: COMSOL simulations at the interface between Au and ZnO NR. (a) 3D plot showing CBM energy and (b) electric field map in ZnO 5 nm below a circular Au dot.

3.7 Conclusions

In conclusion, a simple procedure for ZnO NRs decoration with Au NPs is reported, and the effects on the position and population of electronic energy bands of ZnO are discussed and modelled. Surface decoration with 20 nm Au NPs is obtained by multiple immersion in a colloidal solution, leading to NPs density up to $4.5 \times 10^{10} \text{ NPs cm}^{-2}$. Au decoration significantly affects the radiative emission of ZnO, with different extents in the UV and visible emission processes. The Au decoration significantly reduces the UV radiative emission in comparison to the visible one, and such evidence is attributed to a noteworthy upwards band bending caused by nano Schottky junction formed at Au-ZnO interface. A strong electric field (up to 10^8 V m^{-1}) at ZnO surface results from multiphysics simulation, with a distinctive halo effect beneath the Au NP edges. The effect in photo- and cathodoluminescence analyses is discussed in terms of enhanced separation of generated e-h pairs.

References

- [1] Djurišić, A.B.; Leung, Y.H. Optical properties of ZnO nanostructures. *Small* 2006, doi:10.1002/smll.200600134.
- [2] Wang, Z.L. Nanostructures of zinc oxide. *Mater. Today* 2004, doi:10.1016/S1369-7021(04)00286-X.
- [3] Battaglia, C.; Escarré, J.; Söderström, K.; Charrière, M.; Despeisse, M.; Haug, F.J.; Ballif, C. Nanomoulding of transparent zinc oxide electrodes for efficient light trapping in solar cells. *Nat. Photonics* 2011, doi:10.1038/nphoton.2011.198.
- [4] Hu, L.; Yan, J.; Liao, M.; Xiang, H.; Gong, X.; Zhang, L.; Fang, X. An optimized ultraviolet-a light photodetector with wide-range photoresponse based on zns/zno biaxial nanobelt. *Adv. Mater.* 2012, doi:10.1002/adma.201200512.
- [5] Sergent, S.; Takiguchi, M.; Tsuchizawa, T.; Yokoo, A.; Taniyama, H.; Kuramochi, E.; Notomi, M. Nanomanipulating and Tuning Ultraviolet ZnO-Nanowire-Induced Photonic Crystal Nanocavities. *ACS Photonics* 2017, doi:10.1021/acsp Photonics.7b00116.
- [6] Sergent, S.; Takiguchi, M.; Tsuchizawa, T.; Taniyama, H.; Notomi, M. ZnO-Nanowire-Induced Nanocavities in Photonic Crystal Disks. *ACS Photonics* 2019, doi:10.1021/acsp Photonics.9b00286.
- [7] Akermi, M.; Jaballah, N.; Alarifi, I.M.; Rahimi-Gorji, M.; Chaabane, R. Ben; Ouada, H. Ben; Majdoub, M. Synthesis and characterization of a novel hydride polymer P-DSBT/ZnO nano-composite for optoelectronic applications. *J. Mol. Liq.* 2019, doi:10.1016/j.molliq.2019.110963.
- [8] Zhou, J.; Nomenyo, K.; Cesar, C.C.; Lussion, A.; Schwartzberg, A.; Yen, C.C.; Woon, W.Y.; Lerondel, G. Giant defect emission enhancement from ZnO nanowires through desulfurization process. *Sci. Rep.* 2020, doi:10.1038/s41598-020-61189-7.
- [9] Ramya, M.; Nideep, T.K.; Nampoore, V.P.N.; Kailasnath, M. Solvent assisted evolution and growth mechanism of zero to three dimensional

ZnO nanostructures for dye sensitized solar cell applications. *Sci. Rep.* 2021, doi:10.1038/s41598-021-85701-9.

[10] Naeem-ur-Rehman; Mehmood, M.; Ali, S.M.; Ramay, S.M.; Alkhuraji, T.S. Au/ZnO hybrid nanocomposites and their optical and photocatalytic properties. *Appl. Phys. A Mater. Sci. Process.* 2020, doi:10.1007/s00339-020-03909-4.

[11] Nguyen, T.H.; Do, T.A.T.; Giang, H.T.; Ho, T.G.; Pham, Q.N.; Man, M.T. Effect of metal-support couplings on the photocatalytic performance of Au-decorated ZnO nanorods. *J. Mater. Sci. Mater. Electron.* 2020, doi:10.1007/s10854-020-04056-5.

[12] Ponnuvelu, D. V.; Dhakshinamoorthy, J.; Prasad, A.K.; Dhara, S.; Kamruddin, M.; Pullithadathil, B. Geometrically Controlled Au-Decorated ZnO Heterojunction Nanostructures for NO₂ Detection. *ACS Appl. Nano Mater.* 2020, doi:10.1021/acsanm.0c01053.

[13] Wang, J.; Fan, S.; Xia, Y.; Yang, C.; Komarneni, S. Room-temperature gas sensors based on ZnO nanorod/Au hybrids: Visible-light-modulated dual selectivity to NO₂ and NH₃. *J. Hazard. Mater.* 2020, doi:10.1016/j.jhazmat.2019.120919.

[14] Laskowski, F.A.L.; Oener, S.Z.; Nellist, M.R.; Gordon, A.M.; Bain, D.C.; Fehrs, J.L.; Boettcher, S.W. Nanoscale semiconductor/catalyst interfaces in photoelectrochemistry. *Nat. Mater.* 2020, doi:10.1038/s41563-019-0488-z.

[15] Chen, T.; Xing, G.Z.; Zhang, Z.; Chen, H.Y.; Wu, T. Tailoring the photoluminescence of ZnO nanowires using Au nanoparticles. *Nanotechnology* 2008, doi:10.1088/0957-4484/19/43/435711.

[16] Bora, T.; Myint, M.T.Z.; Al-Harhi, S.H.; Dutta, J. Role of surface defects on visible light enabled plasmonic photocatalysis in Au-ZnO nanocatalysts. *RSC Adv.* 2015, doi:10.1039/c5ra16569e.

[17] Raji, R.; Gopchandran, K.G. Plasmonic photocatalytic activity of ZnO: Au nanostructures: Tailoring the plasmon absorption and interfacial

charge transfer mechanism. *J. Hazard. Mater.* 2019, doi:10.1016/j.jhazmat.2019.01.052.

[18] Shahine, I.; Jradi, S.; Beydoun, N.; Gaumet, J.J.; Akil, S. Plasmon-Enhanced Photoluminescence and Photocatalysis Reactions in Metal-Semiconductor Nanomaterials: UV-Generated Hot Electron in Gold-Zinc Oxide. *ChemPhotoChem* 2020, doi:10.1002/cptc.201900252.

[19] Bahariqushchi, R.; Cosentino, S.; Scuderi, M.; Dumons, E.; Tran-Huu-Hue, L.P.; Strano, V.; Grandjean, D.; Lievens, P.; Poulin-Vittrant, G.; Spinella, C.; et al. Free carrier enhanced depletion in ZnO nanorods decorated with bimetallic AuPt nanoclusters. *Nanoscale* 2020, doi:10.1039/donr04134c.

[20] Hsu, N.E.; Hung, W.K.; Chen, Y.F. Origin of defect emission identified by polarized luminescence from aligned ZnO nanorods. *J. Appl. Phys.* 2004, doi:10.1063/1.1787905.

[21] Shan, W.; Walukiewicz, W.; Ager, J.W.; Yu, K.M.; Yuan, H.B.; Xin, H.P.; Cantwell, G.; Song, J.J. Nature of room-temperature photoluminescence in ZnO. *Appl. Phys. Lett.* 2005, doi:10.1063/1.1923757.

[22] Djurišić, A.B.; Leung, Y.H.; Tam, K.H.; Ding, L.; Ge, W.K.; Chen, H.Y.; Gwo, S. Green, yellow, and orange defect emission from ZnO nanostructures: Influence of excitation wavelength. *Appl. Phys. Lett.* 2006, doi:10.1063/1.2182096.

[23] Tam, K.H.; Cheung, C.K.; Leung, Y.H.; Djurišić, A.B.; Ling, C.C.; Beling, C.D.; Fung, S.; Kwok, W.M.; Chan, W.K.; Phillips, D.L.; et al. Defects in ZnO nanorods prepared by a hydrothermal method. *J. Phys. Chem. B* 2006, doi:10.1021/jp063239w.

[24] Wang, D.; Reynolds, N. Photoluminescence of Zinc Oxide Nanowires: The Effect of Surface Band Bending. *ISRN Condens. Matter Phys.* 2012, doi:10.5402/2012/950354.

[25] Fabbri, F.; Villani, M.; Catellani, A.; Calzolari, A.; Cicero, G.; Calestani, D.; Calestani, G.; Zappettini, A.; Dierre, B.; Sekiguchi, T.; et al.

Zn vacancy induced green luminescence on non-polar surfaces in ZnO nanostructures. *Sci. Rep.* 2014, doi:10.1038/srep05158.

[26] Kumar, V.; Ntwaeaborwa, O.M.; Soga, T.; Dutta, V.; Swart, H.C. Rare Earth Doped Zinc Oxide Nanophosphor Powder: A Future Material for Solid State Lighting and Solar Cells. *ACS Photonics* 2017, doi:10.1021/acsp Photonics.7b00777.

[27] Fiedler, S.; Lee Cheong Lem, L.O.; Ton-That, C.; Phillips, M.R. The role of surface depletion layer effects on the enhancement of the UV emission in ZnO induced by a nanostructured Al surface coating. *Appl. Surf. Sci.* 2020, doi:10.1016/j.apsusc.2019.144409.

[28] Barbagiovanni, E.G.; Strano, V.; Franzò, G.; Reitano, R.; Dahiya, A.S.; Poulin-Vittrant, G.; Alquier, D.; Mirabella, S. Universal model for defect-related visible luminescence in ZnO nanorods. *RSC Adv.* 2016, doi:10.1039/c6ra14453e.

[29] Ruiz Peralta, M.D.L.; Pal, U.; Zeferino, R.S. Photoluminescence (PL) quenching and enhanced photocatalytic activity of Au-decorated ZnO nanorods fabricated through microwave-assisted chemical synthesis. *ACS Appl. Mater. Interfaces* 2012, doi:10.1021/am301155u.

[30] Park, S.; Mun, Y.; An, S.; In Lee, W.; Lee, C. Enhanced photoluminescence of Au-functionalized ZnO nanorods annealed in a hydrogen atmosphere. *J. Lumin.* 2014, doi:10.1016/j.jlumin.2013.10.044.

[31] Udawatte, N.; Lee, M.; Kim, J.; Lee, D. Well-defined Au/ZnO nanoparticle composites exhibiting enhanced photocatalytic activities. *ACS Appl. Mater. Interfaces* 2011, doi:10.1021/am201221x.

[32] Rai, P.; Kim, Y.S.; Song, H.M.; Song, M.K.; Yu, Y.T. The role of gold catalyst on the sensing behavior of ZnO nanorods for CO and NO₂ gases. *Sensors Actuators, B Chem.* 2012, doi:10.1016/j.snb.2012.02.030.

[33] Strano, V.; Urso, R.G.; Scuderi, M.; Iwu, K.O.; Simone, F.; Ciliberto, E.; Spinella, C.; Mirabella, S. Double role of HMTA in ZnO nanorods grown by chemical bath deposition. *J. Phys. Chem. C* 2014, doi:10.1021/jp507496a.

- [34] Turkevich, J.; Stevenson, P.C.; Hillier, J. A study of the nucleation and growth processes in the synthesis of colloidal gold. *Discuss. Faraday Soc.* 1951.
- [35] Frens, G. Controlled Nucleation for the Regulation of the Particle Size in Monodisperse Gold Suspensions. *Nat. Phys. Sci.* 1973, doi:10.1038/physci241020a0.
- [36] Tyagi, H.; Kushwaha, A.; Kumar, A.; Aslam, M. A Facile pH Controlled Citrate-Based Reduction Method for Gold Nanoparticle Synthesis at Room Temperature. *Nanoscale Res. Lett.* 2016, doi:10.1186/s11671-016-1576-5.
- [37] ImageJ. Available online: www.imagej.nih.gov (accessed on 1 February 2021).
- [38] Thompson, M. Xrump. Available online: www.genplot.com (accessed on 1 February 2021).
- [39] Mooney, J.; Kambhampati, P. Get the basics right: Jacobian conversion of wavelength and energy scales for quantitative analysis of emission spectra. *J. Phys. Chem. Lett.* 2013.
- [40] Drouin, D.; Couture, A.R.; Joly, D.; Tastet, X.; Aimez, V.; Gauvin, R. CASINO V2.42 - A fast and easy-to-use modeling tool for scanning electron microscopy and microanalysis users. *Scanning* 2007, doi:10.1002/sca.20000.
- [41] COMSOL Multiphysics® v. 5.3. <http://www.comsol.com>. COMSOL AB, Stockholm, Sweden.
- [42] Feldman, L.C.; Mayer, J.W.; Grasserbauer, M. Fundamentals of surface and thin film analysis. *Anal. Chim. Acta* 1987, doi:10.1016/S0003-2670(00)82855-x.
- [43] Studenikin, S.A.; Cocivera, M. Time-resolved luminescence and photoconductivity of polycrystalline ZnO films. *J. Appl. Phys.* 2002, doi:10.1063/1.1461890.

- [44] Hong, S.; Joo, T.; Park, W.; Jun, Y.H.; Yi, G.C. Time-resolved photoluminescence of the size-controlled ZnO nanorods. *Appl. Phys. Lett.* 2003, doi:10.1063/1.1627472.
- [45] Kwok, W.M.; Djurišić, A.B.; Leung, Y.H.; Chan, W.K.; Phillips, D.L. Time-resolved photoluminescence from ZnO nanostructures. *Appl. Phys. Lett.* 2005, doi:10.1063/1.2137456.
- [46] Zhang, X.H.; Chua, S.J.; Yong, A.M.; Yang, H.Y.; Lau, S.P.; Yu, S.F.; Sun, X.W.; Miao, L.; Tanemura, M.; Tanemura, S. Exciton radiative lifetime in ZnO nanorods fabricated by vapor phase transport method. *Appl. Phys. Lett.* 2007, doi:10.1063/1.2429019.
- [47] Zhao, Q.X.; Yang, L.L.; Willander, M.; Sernelius, B.E.; Holtz, P.O. Surface recombination in ZnO nanorods grown by chemical bath deposition. *J. Appl. Phys.* 2008, doi:10.1063/1.2991151.
- [48] Klason, P.; Moe Børseth, T.; Zhao, Q.X.; Svensson, B.G.; Kuznetsov, A.Y.; Bergman, P.J.; Willander, M. Temperature dependence and decay times of zinc and oxygen vacancy related photoluminescence bands in zinc oxide. *Solid State Commun.* 2008, doi:10.1016/j.ssc.2007.10.036.
- [49] Layek, A.; Manna, B.; Chowdhury, A. Carrier recombination dynamics through defect states of ZnO nanocrystals: From nanoparticles to nanorods. *Chem. Phys. Lett.* 2012, doi:10.1016/j.cplett.2012.05.028.
- [50] Biroju, R.K.; Giri, P.K. Strong visible and near infrared photoluminescence from ZnO nanorods/nanowires grown on single layer graphene studied using sub-band gap excitation. *J. Appl. Phys.* 2017, doi:10.1063/1.4995957.
- [51] Barbagiovanni, E.G.; Reitano, R.; Franzò, G.; Strano, V.; Terrasi, A.; Mirabella, S. Radiative mechanism and surface modification of four visible deep level defect states in ZnO nanorods. *Nanoscale* 2016, doi:10.1039/c5nr05122c.
- [52] Barbagiovanni, E.G.; Strano, V.; Franzò, G.; Crupi, I.; Mirabella, S. Photoluminescence transient study of surface defects in ZnO nanorods

grown by chemical bath deposition. *Appl. Phys. Lett.* 2015, doi:10.1063/1.4914067.

[53] Brillson, L.J.; Mosbacher, H.L.; Hetzer, M.J.; Strzhemechny, Y.; Look, D.C.; Cantwell, G.; Zhang, J.; Song, J.J. Surface and near-surface passivation, chemical reaction, and Schottky barrier formation at ZnO surfaces and interfaces. *Appl. Surf. Sci.* 2008, doi:10.1016/j.apsusc.2008.03.050.

[54] K. Kanaya, S. Okayama, Penetration and energy-loss theory of electrons in solid targets, *J. Phys. D. Appl. Phys.* 1972, <https://doi.org/10.1088/0022-3727/5/1/308>.

[55] F.A. Lukiyanov, E.I. Rau, R.A. Sennov, Depth range of primary electrons, electron beam broadening, and spatial resolution in electron-beam studies, *Bull. Russ. Acad. Sci. Phys.* 2009, <https://doi.org/10.3103/S1062873809040029>.

[56] G. Agostini, C. Lamberti, Characterization of Semiconductor Heterostructures and Nanostructures, 2008, <https://doi.org/10.1016/B978-0-444-53099-8.X0001-2>.

[57] Brillson, L.J. Applications of depth-resolved cathodoluminescence spectroscopy. *J. Phys. D. Appl. Phys.* 2012, doi:10.1088/0022-3727/45/18/183001.

[58] Ye, J.D.; Zhao, H.; Liu, W.; Gu, S.L.; Zhang, R.; Zheng, Y.D.; Tan, S.T.; Sun, X.W.; Lo, G.Q.; Teo, K.L. Theoretical and experimental depth-resolved cathodoluminescence microanalysis of excitonic emission from ZnO epilayers. *Appl. Phys. Lett.* 2008, doi:10.1063/1.2907249.

[59] Toth, M.; Phillips, M.R. Monte Carlo modeling of cathodoluminescence generation using electron energy loss curves. *Scanning* 1998, doi:10.1002/sca.1998.4950200601.

[60] Bott, A.W. Electrochemistry of Electrochemistry of Semiconductors. *Curr. Sep.* 1998.

- [61] Beranek, R. (Photo)electrochemical methods for the determination of the band edge positions of TiO₂-based nanomaterials. *Adv. Phys. Chem.* 2011, doi:10.1155/2011/786759.
- [62] Fabregat-Santiago, F.; Garcia-Belmonte, G.; Bisquert, J.; Bogdanoff, P.; Zaban, A. Mott-Schottky Analysis of Nanoporous Semiconductor Electrodes in Dielectric State Deposited on SnO₂(F) Conducting Substrates. *J. Electrochem. Soc.* 2003, doi:10.1149/1.1568741.
- [63] Hankin, A.; Bedoya-Lora, F.E.; Alexander, J.C.; Regoutz, A.; Kelsall, G.H. Flat band potential determination: Avoiding the pitfalls. *J. Mater. Chem. A* 2019, doi:10.1039/c9ta09569a.
- [64] Memming, R. *Semiconductor Electrochemistry*; 2015.
- [65] Scholz, F. *Electroanalytical methods: Guide to experiments and applications*; 2010; ISBN 9783642029141.
- [66] Xu, P.; Milstein, T.J.; Mallouk, T.E. Flat-Band Potentials of Molecularly Thin Metal Oxide Nanosheets. *ACS Appl. Mater. Interfaces* 2016, doi:10.1021/acsami.6b02901.
- [67] Gelderman, K.; Lee, L.; Donne, S.W. Flat-band potential of a semiconductor: Using the Mott-Schottky equation. *J. Chem. Educ.* 2007, doi:10.1021/ed084p685.
- [68] Darowicki, K.; Krakowiak, S.; Ślepski, P. Selection of measurement frequency in Mott-Schottky analysis of passive layer on nickel. In *Proceedings of the Electrochimica Acta*; 2006.
- [69] Bruno, L.; Strano, V.; Scuderi, M.; Franzò, G.; Priolo, F.; Mirabella, S. Localized Energy Band Bending in ZnO Nanorods Decorated with Au Nanoparticles. *Nanomaterials* 2021, doi:10.3390/nano11102718.
- [70] Henry M.; Fanet H. *Physique des semiconducteurs et des composants électroniques*; 2019.

[71] Gutmann, S.; Conrad, M.; Wolak, M.A.; Beerbom, M.M.; Schlaf, R. Work function measurements on nano-crystalline zinc oxide surfaces. *J. Appl. Phys.* 2012, doi:10.1063/1.4729527.

[72] Ahn, C.H.; Kim, Y.Y.; Kim, D.C.; Mohanta, S.K.; Cho, H.K. A comparative analysis of deep level emission in ZnO layers deposited by various methods. *J. Appl. Phys.* 2009, doi:10.1063/1.3054175.

[73] Janotti, A.; Van De Walle, C.G. Native point defects in ZnO. *Phys. Rev. B - Condens. Matter Mater. Phys.* 2007, doi:10.1103/PhysRevB.76.165202.

Chapter 4

Bare and Pt decorated NiO microflowers for overall water splitting

Content

Part 1.

Enhanced Electrocatalytic Activity of low cost NiO Microflowers on Graphene Paper for Oxygen Evolution Reaction	74
Materials and Methods	76
Synthesis of NiO microflowers	76
Preparation of the electrode	76
Characterization of NiO microflowers on graphene paper electrodes	77
Materials Characterization	78
Electrochemical characterization – OER	80
OER performance evaluation	84

Part 2.

Physical Insights into Alkaline overall water splitting with NiO Microflowers Electrodes with ultra-low amount of Pt catalyst	91
Experimental	93
Preparation of the electrode	93
Characterization of Pt decorated NiO microflowers	94
Morphological and elemental characterization	95
Electrochemical characterization - HER	97
Overall water splitting	105
Conclusions	106
References	107

Summary

Electrochemical water splitting represents a promising source of renewable energy. It is composed of two half reactions: the oxygen evolution reaction (OER) and the hydrogen evolution reaction (HER), taking place at the anode and cathode, respectively. This chapter is divided into two parts:

Part 1.

OER represents a limiting factor for overall water splitting because of its slow kinetics and large energy barrier. Typically, critical raw materials such as IrO₂ and RuO₂ can be involved as catalysts, still sustainable and efficient catalysts are urgently required. Among oxides of transition metals, NiO represents a promising candidate as high-performance catalyst for oxygen evolution reaction. Here, a low-cost, high-throughput, environmentally friendly chemical methodology produces NiO microflowers composed of very thin sheets (20 nm thick) intertwined like petals of a desert rose. These microflowers, dispersed onto a graphene paper substrate by spin coating or drop casting, are carefully tested as electrocatalysts for OER. The reported results prove that Ni based nanostructures are promising materials for efficient anode in sustainable water splitting electrocatalysis.

Part 2.

HER in alkaline media requires high amount of Pt based catalysts due to its sluggish kinetics. Herein, we report a low-cost chemical methodology to decorate NiO microflowers with ultralow amounts of Pt nanoparticles. These decorated microflowers, dispersed onto graphene paper by drop casting, build a high-performance HER. The effect of Pt decoration has been modelled through energy band bending supported by electrochemical analyses. A full cell for alkaline electrochemical water splitting has been built, composed of Pt decorated NiO microflowers as cathode and bare NiO microflowers as anode, showing a low potential of 1.57 V to afford a current density of 10 mA cm⁻² and a good long-term stability. The reported results pave the way towards an extensive utilization of Ni based nanostructures with ultralow Pt content for efficient electrochemical water splitting.

Efficient and cheap renewable energy production from water electrolysis is a crucial challenge for a sustainable society [1-4]. Electrochemical water splitting represents a promising way to produce renewable energy. Water splitting is composed of two half reactions: the oxygen evolution reaction (OER) and the hydrogen evolution reaction (HER), taking place at the anode and cathode, respectively [5,6]. Figure 5.1 shows a schematic representation of both reactions and the plot of the current as a function of the applied potential.

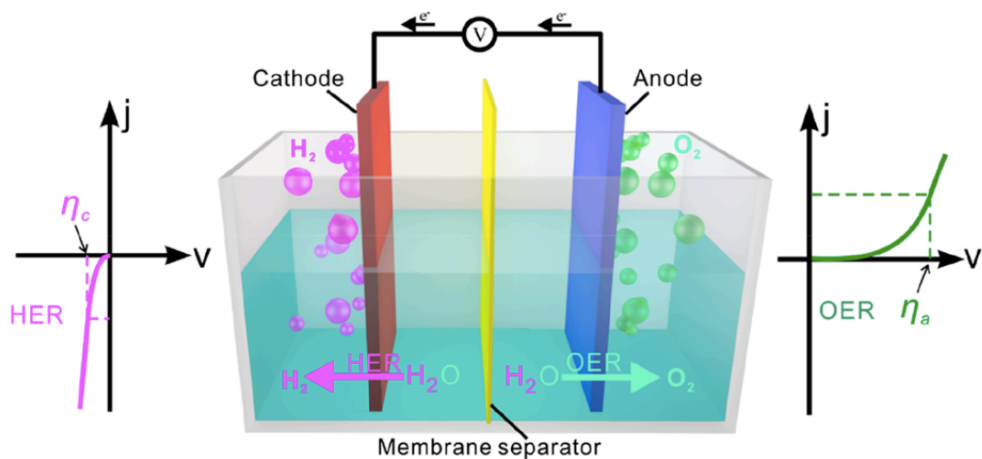


Figure 5.1: Hydrogen evolution reaction and oxygen evolution reaction of electrocatalytic water splitting [Adapted from 3].

Part 1.

P1.5.1 Enhanced Electrocatalytic Activity of low-cost NiO Microflowers on Graphene Paper for Oxygen Evolution Reaction

The OER is considered the limiting process of the overall water electrolysis, because it involves four sequential electron transfer, thereby having slow kinetics and a large energy barrier for water splitting [7-9]. In alkaline solution (Figure P1.5.1), the OER can be described by the following electrochemical reaction [8]:

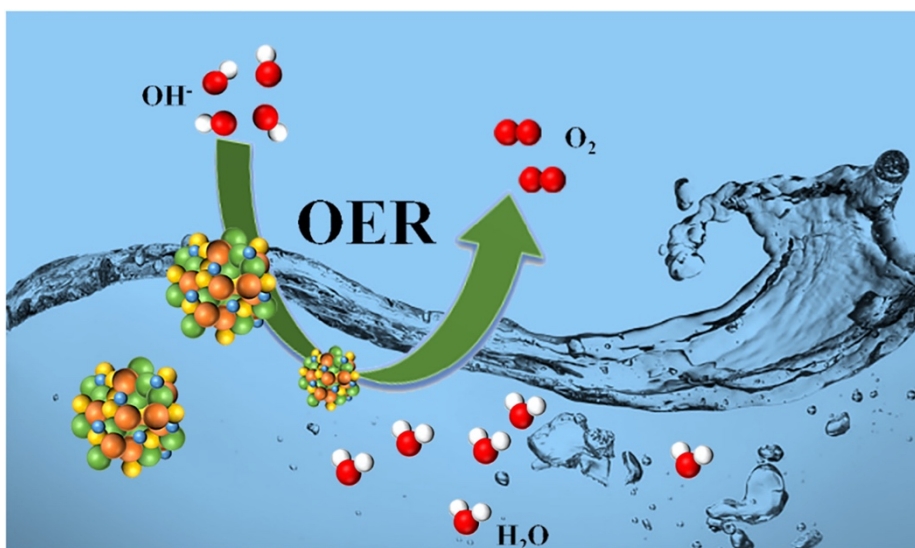


Figure P1.5.1: Illustration of the electrocatalytic OER in alkaline media.

Over the past decades, considerable research effort has been devoted to design, synthesize, and characterize different oxygen evolution anode materials with the aim of achieving acceptable rates of active oxygen production at the lowest possible overpotentials [8]. Optimizing the kinetics of the OER is crucial for the generation of hydrogen as a renewable fuel. Accordingly, the development of efficient, abundant, and inexpensive catalysts is essential. Nowadays, one important issue is the availability of raw materials for large-scale production of energy through electrolysis [10-12].

Although their significant economic importance for key sectors in the global economy, they have a high-supply risk and there is a lack of (suitable) substitutes, due to their unique and reliable properties. The development of new non-precious metal catalysts and understanding the origin of their activity for the OER are essential for rationally designing highly active low-cost catalysts as alternatives to state-of-the-art critical raw materials [13,14].

Oxides and hydroxides of non-critical transition metals (e.g., Fe, Co, Ni) have been extensively investigated and are currently prevailing electrocatalysts used in the OER [6,15-17]. Although they possess inferior electrocatalytic activity for the OER if compared with the state-of-art materials (RuO_2 , IrO_2), they have relatively low cost and high corrosion resistance in alkaline solution as anode materials for the OER [18,19]. Among these, Ni oxide represents a promising candidate as anode material with enhanced electrochemical performances [20-25].

Both experimental and theoretical studies suggested that the Ni^{2+} has the more efficient interactions with OH^- for the OER compared with other metal oxides (Fe, Mn, Co) which is ideal for catalysts with superior performance [23,26]. Furthermore, NiO nanostructures (such as oriented arrays, multilayers, or interconnected networks) increase electrolyte permeability through the active material, facilitating the mass transport at the interface [24]. Thanks to unique size dependent properties, mass diffusion, and high surface area, nanostructured NiO is often used as a high-performance OER catalyst [21-23,25,27-29]. Finally, graphene supported NiO nanostructures has been demonstrated in literature very good option, since graphene enhances electron transport and hence catalytic performance [30-32], promotes nanostructures dispersion and inhibits their aggregation.

The electrochemical performance of the catalyst should be carefully evaluated in terms of the balance between mass loading and intensive quantities (Turnover frequencies and mass activities). The frequently used overpotential value at fixed current density (as indicator for the catalytic activity of the electrodes) is largely dependent on catalyst mass and surface over volume ratio. A careful determination of Turnover frequency and mass activity, independent of catalyst mass, is a key step towards a solid evaluation of the electrochemical properties of new OER catalysts¹⁷. They provide a clear and unequivocal indication of the real intrinsic catalytic properties of the materials used, decoupling them from the effects linked to the catalyst mass loading.

P1.5.2 Experimental

P1.5.2.1 Synthesis of NiO microflowers

NiO microflowers (μ Fs) were obtained from a chemical solution method through a bain-marie configuration at 50 °C (see Appendix B for details).

P1.5.2.2 Preparation of the electrode

Graphene paper (GP) substrates (240 nm thick, Sigma Aldrich, St. Louis, MO, USA) were rinsed with deionized water and dried in N₂ to clean the surface from any impurity. The electrode is realized by spin coating (200 rpm, 4 minutes) μ Fs solution onto GP in an area of 1 cm². Electrodes were dried on a hot plate at 80 °C for 10 minutes. The amount of catalyst was varied by adding another drop of solution and repeating the spin coating and drying steps. NiO μ Fs loaded on GP by spin coating were labelled NiO_{S1} and NiO_{S2}. To further increase the μ Fs mass on GP we deposited 10 μ L of μ Fs solution via drop casting in an area of 1 cm², followed by drying on hot plat at 80 °C for 10 minutes.

Also in this case, the amount of catalyst was varied through the addition of different drop of solution. The electrodes prepared by drop casting method were labelled NiO_{D1}, NiO_{D2} and NiO_{D3}. The mass of μ Fs on GP was measured by a Mettler Toledo MX5 Microbalance (sensitivity: 0.01 mg). The values obtained for the catalysts mass were 0.06 mg, 0.18 mg, 0.30 mg, 0.50 mg, and 0.75 mg for NiO_{S1}, NiO_{S1}, NiO_{D1}, NiO_{D2}, and NiO_{D3}, respectively. Table P1.5.1 summarizes the deposition method and the mass loading of the prepared samples.

Sample	Deposition method	Catalyst loading [± 0.01 mg]
NiO _{S1}	SPIN COATING	0.06
NiO _{S2}	SPIN COATING	0.18
NiO _{D1}	DROP CASTING	0.30
NiO _{D2}	DROP CASTING	0.50
NiO _{D3}	DROP CASTING	0.75

Table P1.5.1: Deposition Method and Catalyst loading for all the prepared electrodes.

P1.5.2.3 Characterization of NiO microflowers on graphene paper electrodes

Surface morphology was analyzed by using a Scanning Electron Microscope (Gemini field emission SEM Carl Zeiss SUPRA 25, FEG-SEM, Carl Zeiss Microscopy GmbH, Jena, Germany) combined with energy dispersive X-ray spectroscopy (EDX). SEM images were analyzed by using ImageJ software [33].

The amount of NiO μ Fs on GP was evaluated by Rutherford backscattering spectrometry (RBS, 2.0 MeV He⁺ beam at normal incidence) with a 165° backscattering angle by using a 3.5 MV HVEE Singletron accelerator system (High Voltage Engineering Europa, Netherlands). RBS spectra were analyzed by using XRump software [34].

XRD patterns were recorded using a Rigaku Smartlab diffractometer, equipped with a rotating anode of Cu K α radiation operating at 45 kV and 200 mA, in grazing incidence mode (0.5 °).

Transmission electron microscopy (TEM) analyses of NiO μ Fs dispersed on a TEM grid were performed with a Cs-probe-corrected JEOL JEM ARM200F microscope at a primary beam energy of 200 keV operated in scanning TEM (STEM) mode. STEM images were analyzed by using DigitalMicrograph® software [35].

Electrochemical measurements were carried out at room temperature by using a VersaSTAT 4 potentiostat (Princeton Applied Research, USA) and a three-electrode setup with a platinum counter electrode, a saturated calomel electrode (SCE, HI-5412 Glass body refill calomel reference electrode, Hanna Instruments) as reference electrode, and our samples as working electrode, without purging any inert gas. 1 M KOH (pH 14, Sigma Aldrich, St. Louis, MO, USA) was used as supporting electrolyte. Current density was normalized to the geometrical surface area and measured potentials vs SCE were converted to the reversible hydrogen electrode (RHE) according to the equation [36]:

$$E_{\text{RHE}} = E_{\text{SCE}} + 0.059 \cdot \text{pH} + 0.244 \quad (\text{P1.5.2})$$

Cyclic voltammetry (CV) curves were recorded at a scan rate of 5 mV s⁻¹ in the potential range -0.3 ÷ 1.0 V vs SCE in order to stabilize electrodes. OER activities of NiO catalysts were investigated using linear sweep voltammetry (LSV) at scan rate of 5 mV s⁻¹. Electrochemical impedance spectroscopy (EIS) was performed with a superimposed 5 mV sinusoidal voltage in the frequency range 10⁴ ÷ 10⁻¹ Hz. Nyquist plots were acquired in the so-called turnover region, just after the onset potential of each

sample where all the studied electrocatalysts possess appreciable OER activity [38]. All measured potentials (η') were manually corrected by iR_u -compensation as follows:

$$\eta = \eta' - iR_u \quad (\text{P1.5.3})$$

where i is the electrode current and R_u [Ω] is the uncompensated resistance, as measured by EIS.

Tafel plots were extrapolated from polarization curves by plotting the overpotential η as a function of the log of current density. Chronopotentiometry (CP) analysis was employed to study the stability of samples in a 1 M KOH solution for 15 hours at a constant current density of 10 mA cm^{-2} .

P1.5.3 Materials characterization

Figure P1.5.2(a-b) shows SEM and STEM images of NiO μ Fs. The morphology of the catalysts remembers that of a desert rose (inset Figure P1.5.2(a)), an intricate formation of rose-like crystal clusters of gypsum or baryte, which include abundant sand grains.

NiO μ Fs are further characterized by using X-ray diffraction (XRD) spectroscopy (XRD pattern in Figure P1.5.2(c)). All the reflections in XRD pattern can be indexed to face-centered cubic (fcc) phase NiO (JCPDS card no. #47-1049). The two characteristic peaks at 37.25° , and 43.28° , correspond to the (111), and (200) diffraction planes, respectively. No peaks from other phases are detected, indicating that the product is of high purity.

An in-plane view STEM micrograph of a single NiO nanosheet is shown in Figure P1.5.2(d). The inset is an enlarged view of the NiO nanosheet at atomic resolution that shows the crystal lattice and confirms that it is NiO Fm-3m in the bunsenite form (Figure P1.5.2(e) shows a 3-D atomic model of NiO fcc atomic cell). Furthermore, it was found that the nanosheets composing the μ Fs are (111) planes (Figure P1.5.2(b) and P1.5.2(d)).

EDX spectrum of NiO μ Fs on GP is reported in Figure P1.5.2(f), indicating the effective deposition of catalyst on the carbon-based substrate. EDX analysis unravels the presence of a peak at 0.85 keV easily attributed to the L_{α} of Ni, whereas the two peaks centered at 7.47 and 8.26 keV arise from K_{α} and K_{β} lines of Ni, respectively. The C peak (K_{α} , 0.277 keV) is ascribed to the underneath GP substrate.

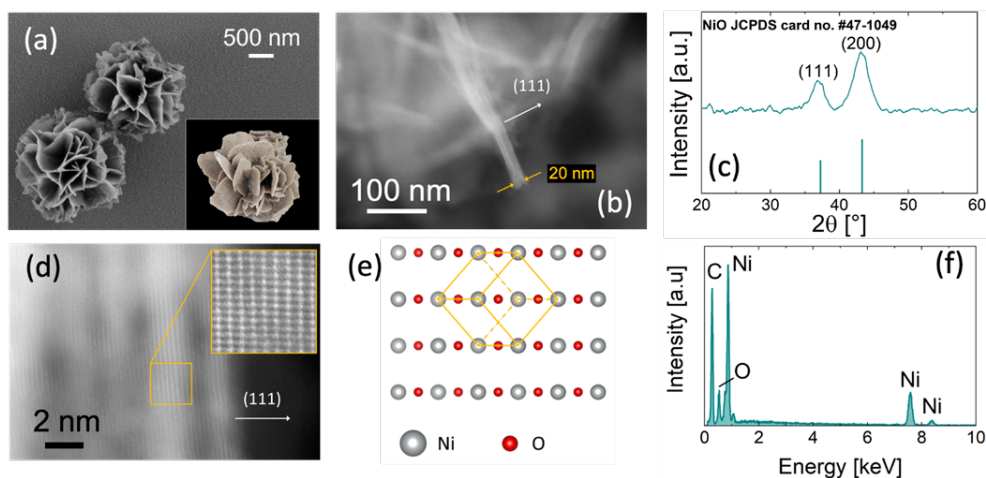


Figure P1.5.2: (a) SEM image of NiO μ Fs dispersed on GP (desert rose in the inset); (b) STEM image of a single NiO nanosheet; (c) XRD pattern of NiO μ Fs; (d) high resolution STEM images of the edge of a nanosheet with an enlarged view of atomic lattice in the inset; (e) 3-D atomic model of the NiO fcc atomic cell; (f) EDX spectrum of μ Fs dispersed on GP.

Mass variation of NiO μ Fs on GP was confirmed by Rutherford backscattering spectrometry (RBS) analysis (Figure P1.5.3(a)) since the Ni amount is proportional to the Ni peak (~ 1.5 MeV) in the spectrum [37]. As expected, Ni amounts on GP increased with the number of drops, both during spin coating and drop casting. The low tail of Ni peak at low energies is attributable to a 3D cluster configuration of Ni μ Fs agglomerated onto the substrate. Peaks at 0.45 MeV and 0.7 MeV refer to the presence of carbon and oxygen from the substrate and μ Fs, respectively.

Finally, SEM analysis allowed us to assess the presence or absence of NiO μ Fs agglomerates depending on the deposition method. Figure C3 confirms the presence of large agglomerates of μ Fs in the case of drop casting method while almost no agglomeration was detected in the spin coating case.

After OER test, NiO μ Fs do not appreciably change their morphology (Figure P1.5.3(b) shows NiO_{S1} electrode after OER).

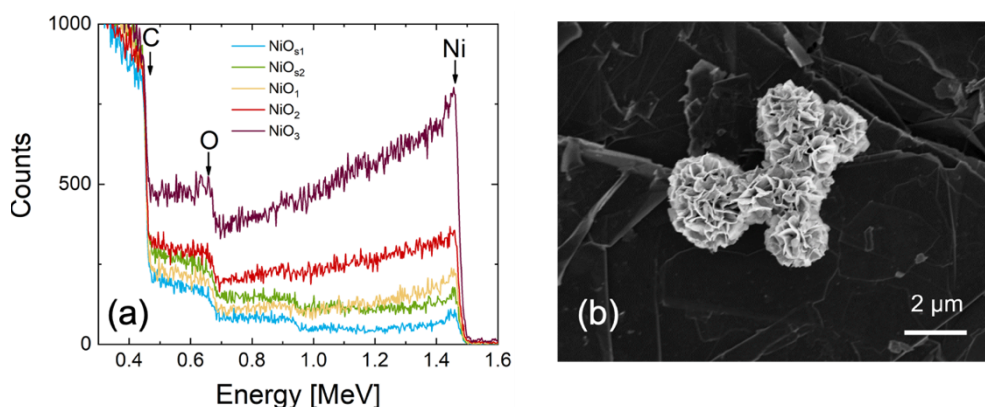


Figure P1.5.3: (a) RBS spectra of NiO μ Fs on GP; (b) SEM images of NiO μ Fs on GP after electrochemical tests.

P1.5.4 Electrochemical characterization – OER

To measure the performances of NiO μ Fs electrocatalysts toward OER, we performed a series of electrochemical measurements in alkaline media (1M KOH, pH 14). Figure P1.5.4 reports the polarization curves of the samples (obtained from linear sweep voltammetry technique, LSV) after their stabilization through CV (\sim 20 cycles). Two kinds of behavior can be recognized in all the samples:

- (i) at low overpotentials all the electrodes show a similar response, with a rapid increase of current density due to oxygen formation;
- (ii) at high overpotentials the slope for spin coated samples is well lower than that of other samples.

OER is somehow quenched for low massive samples at higher current density (Table P1.5.2). NiO_{D2} and NiO_{D3} samples (with a mass of 0.50 and 0.75 mg, respectively) exhibit improved OER performance, as evidenced

by the overpotential of (314 ± 1) mV and (312 ± 1) mV required to reach a current density of 10 mA cm^{-2} , which is lower compared to those ones for samples with lower mass.

The similar values for both catalysts suggested us that not only the material dispersion plays a crucial role in the catalytic performance, but all the amount of catalyst is a fundamental parameter to investigate the electrochemical behavior of the samples. It seems to be a sort of a limiting mass (0.50 mg in our case) beyond which no further increase of overpotential can be detected.

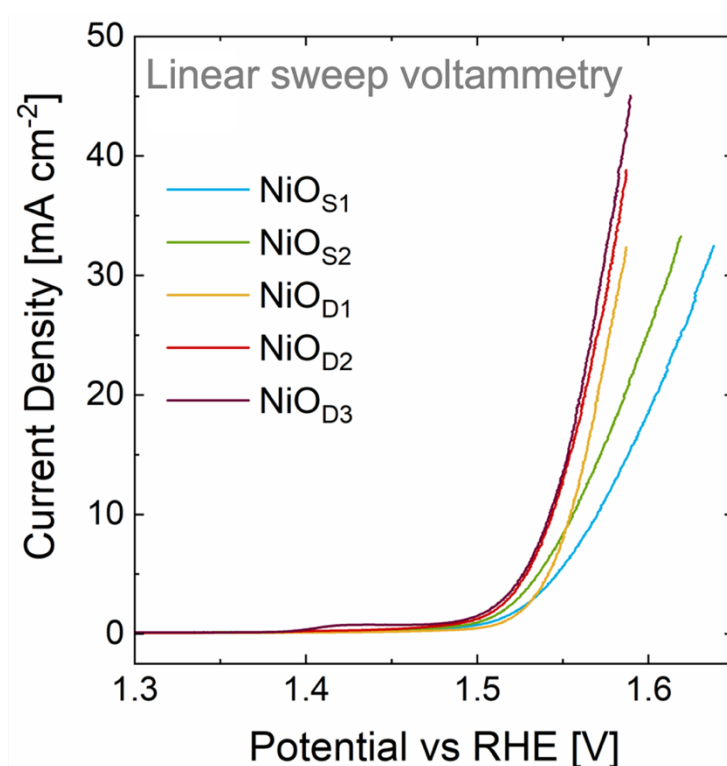


Figure P1.5.4: (a) Polarization curves of NiO on GP.

To assess the activity trend of our set of electrocatalysts and to further elucidate the electrode kinetics, electrochemical impedance spectroscopy (EIS) was performed (Figure P1.5.5(a)). This kind of circuit is extensively used in all these cases in which products are formed after the adsorption/desorption of one or more intermediates species at the electrode surface [41,42-46]. Table P1.5.3 reports all the parameters extracted from the fit.

In this circuit (Figure P1.5.5(b)), R_u is the uncompensated resistance (linked with the voltage drop in the solution), R_{ct} is the charge transfer resistance for the electrode reaction, CPE_{dl} the double layer capacitance (in our case all the capacitances are replaced with Constant Phase Elements, CPE, to take into account the non-ideal behavior of the electrodes), R_p is related to the mass transfer resistance (pseudoresistance) of the adsorbed intermediate OH^- , and CPE_p is the pseudocapacitance (associated with the surface coverage of the adsorbed intermediates) [18,20,38,41,42-45]. The experimental data, supported by the Armstrong and Henderson model, show a reduction in both R_{ct} and R_p as the mass of the catalyst increases, while R_u remains almost constant (Figure P1.5.6(a)), as expected. The reduced R_{ct} and R_p prove that the increase in catalyst mass accelerates the electron transfer kinetics at the electrode-solution interface, facilitating the adsorption of OH^- on the surface of μ Fs (and the subsequent O_2 formation). The increase in mass leads to an increase in CPE_{dl} indicating an improved capability to adsorb OH^- and higher electrocatalytic activity (Figure P1.5.6(b)). By contrast CPE_p decreases as the mass of catalyst increases since the higher the number of active sites, the lower their occupancy.

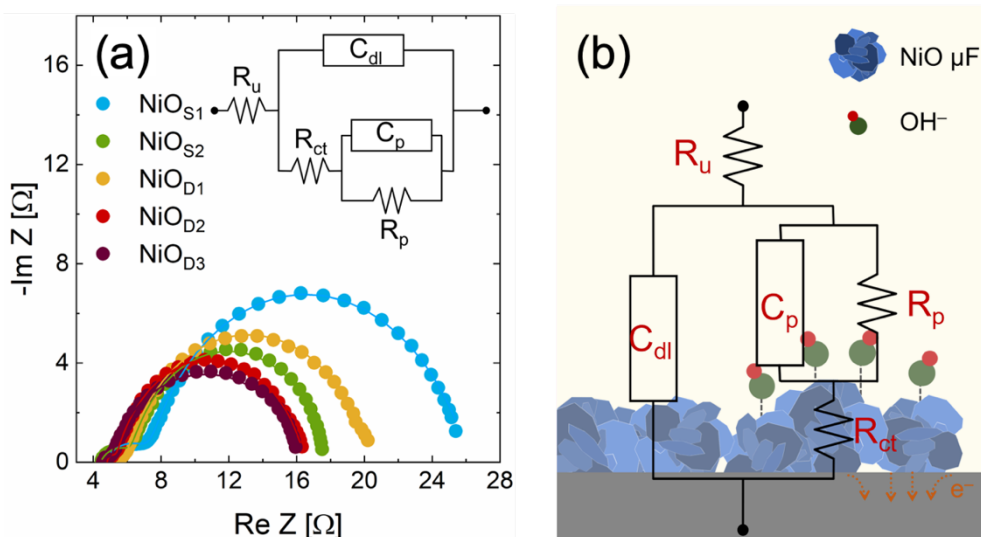


Figure P1.5.5: (a) Nyquist plots with the fitting curves plotted, (b) schematic representation of equivalent circuit elements on NiO catalyst on GP.

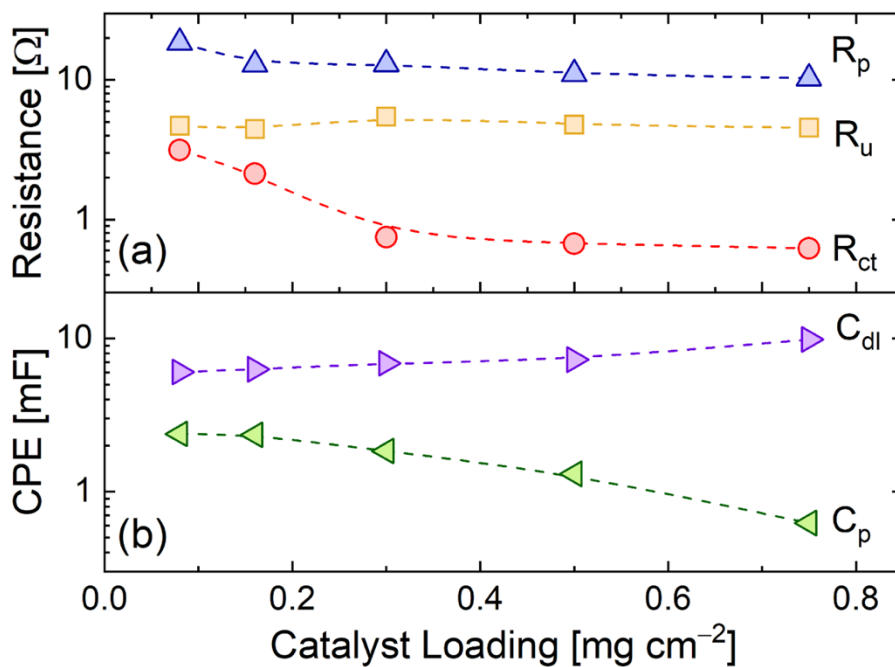


Figure P1.5.6: Behavior of equivalent circuit elements as a function of mass loading.

Sample	Catalyst loading [±0.01 mg]	Overpotential at 10 mA cm ⁻² [±1 mV]	Tafel slope [mV dec ⁻¹]
NiO _{S1}	0.06	338	54-108
NiO _{S2}	0.18	326	48-97
NiO _{D1}	0.30	324	40-50
NiO _{D2}	0.50	314	47-60
NiO _{D3}	0.75	312	56-58

Table P1.5.2: Overpotential (at a current density of 10 mA cm⁻²) and Tafel slope for NiO microflowlers on GP.

Sample	R_u [Ω]	R_{ct} [Ω]	R_p [Ω]	C_{dl} [mF s ⁿ⁻¹]	n_1	C_p [mF s ⁿ⁻¹]	n_2
NiO _{S1}	4.67	2.71	18.6	6.05	0.8	2.38	0.6
NiO _{S2}	4.44	2.00	12.9	6.93	0.8	2.35	0.6
NiO _{D1}	5.47	0.68	13.1	6.89	0.8	1.84	0.8
NiO _{D2}	4.78	0.61	11.1	7.3	0.8	1.3	0.7
NiO _{D3}	4.54	0.43	10.3	9.87	0.9	0.62	0.6

Table P1.5.3: EIS fitting parameters.

P1.5.5 OER performance evaluation

The electrocatalytic activities of NiO μ Fs were further examined by corresponding Tafel plots, extrapolated from polarization curves (Figure P1.5.7), and the Tafel slopes extrapolated from the linear fit of data points are reported in Table P1.5.2. Generally, a smaller Tafel slope implies faster electrochemical kinetics [4,7,8].

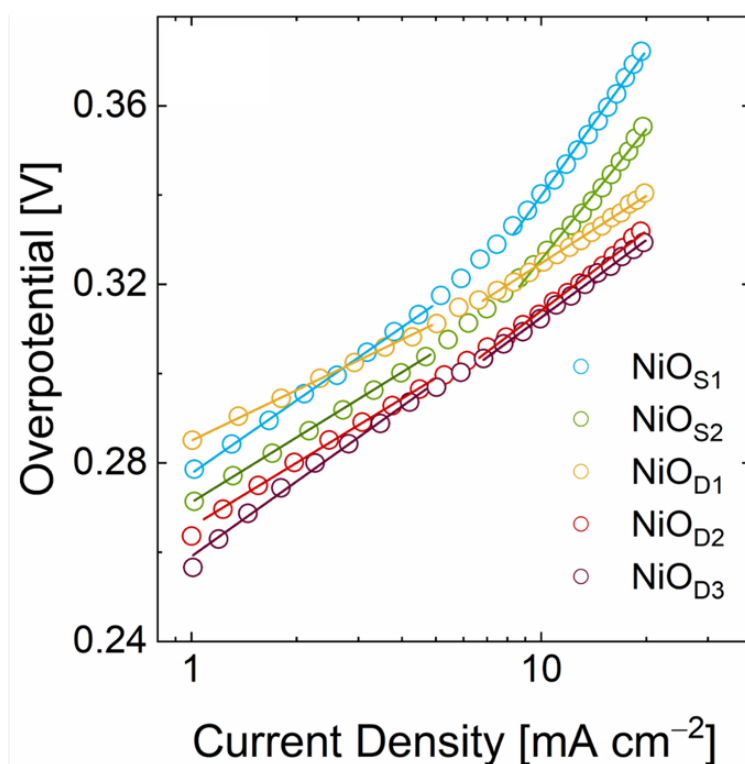


Figure P1.5.7: Tafel plots of NiO μ Fs deposited on GP substrates.

Moreover, it is possible to have an indication of the rate determining step (RDS) of the process. By considering the different proposed path for OER [8,19] and the works of Doyle, Brandon and Lyons [18,20,47] on OER on Ni electrodes, our Tafel slopes in the low current density region indicate a RDS represented by the adsorption of OH^- ions on the surface of the electrocatalyst (see Appendix C for details on OER mechanism at Ni-based electrodes).

Any change of Tafel slope in this potential region can easily reflect the concentration of active sites and their contribution in the overall process [7]. The lower Tafel slope of drop casted catalysts indicates that the oxygen production rate is reduced for massive samples. At high current density, the Tafel slopes drastically change for the samples prepared by spin coating (reflecting the trend of current density in LSVs of Figure P1.5.4). For drop casted catalyst the Tafel slope values remain nearly constant for the entire investigated potential range. The mentioned increase can be attributed to different mechanisms:

- (i) increased mass transport resistances,
- (ii) (ii) change in the RDS,
- (iii) (iii) adsorption of the reaction intermediates [20],
- (iv) (iv) change of active sites and their contribution [7].

Given the above, the small mass deposited on the GP for NiO_{S1} and NiO_{S2} does not provide an adequate number of active sites to produce oxygen causing a change in the slope of the polarization curves and an increase of Tafel slopes.

Our results prove that there is a limit mass value (and a degree of dispersion) below which the catalytic performance of NiO electrodes drastically worsens at high overpotentials. Nevertheless, to deeper investigate the effect of NiO μ Fs in the OER mechanism it is essential to take into account the number and especially availability of active sites on the surface of the catalysts.

Relying only on overpotential to evaluate the OER performance can be misleading since that is an extensive quantity and it is not quantitatively linked to the number of active materials involved in the OER. Not only the number of active sites on the surface of our catalysts influences the oxygen production, but also the rate of adsorption/desorption of OH⁻ ions. To better investigate the metrics related to the intrinsic activity of the electrodes, the turn-over frequency (TOF) must be considered [17,48]. The TOF is defined as the rate of production of oxygen molecules per active site:

$$\text{TOF} = \frac{I}{4nF} \quad (\text{P1.5.4})$$

where I is the measured current at a fixed overpotential, the term 4 represents the number of electrons involved in the OER, F is the Faraday constant and n is the number of moles of the active sites [48].

The greatest difficulties come from determining the number of active sites. There is not a general consensus in considering the bulk of the catalyst or only the outer surface as an active element involved the OER [16]. At least two possibilities can be identified:

- (i) the activity is confined to a near surface region in which there is ionic conductivity and electrolyte intercalated between the μF and in the multiple plans composing NiO nanosheets, and
- (ii) bulk activity in which the entire material is active [16,17,47]. We determined a minimum (TOF_{bulk}) and a maximum ($\text{TOF}_{\text{redox}}$) TOF based on the different assumptions on the number of active sites described above.

In particular, TOF_{bulk} assumes that all the deposited moles are active, while $\text{TOF}_{\text{redox}}$ assumes that only one active site per electron is transferred in the Ni reduction peak of the cyclic voltammogram (CV, see Figure P1.5.8) [16]. For the calculation of TOF_{bulk} , the number of moles is given by:

$$n = \frac{\text{total mass [g]}}{\text{MW [g mol}^{-1}] \cdot A[\text{cm}^2]} \quad (\text{P1.5.5})$$

where A is the testing area of the electrode and MW is the molecular weight of NiO ($74.6928 \text{ g mol}^{-1}$).

Concerning the determination of redox peak integration is the easiest approach and an efficient way of finding out the number of active catalytic sites. It is possible to use the first backward sweep of a CV scan and integrate the charge under the reduction peak [48]. The n for $\text{TOF}_{\text{redox}}$ can be calculated by the following expression:

$$n = \frac{Q [\text{C}]}{F [\text{C mol}^{-1}] \cdot A [\text{cm}^2]} \quad (\text{P1.5.6})$$

where Q is the total charge of a redox peak, F is the Faraday constant (96485 C mol^{-1}).

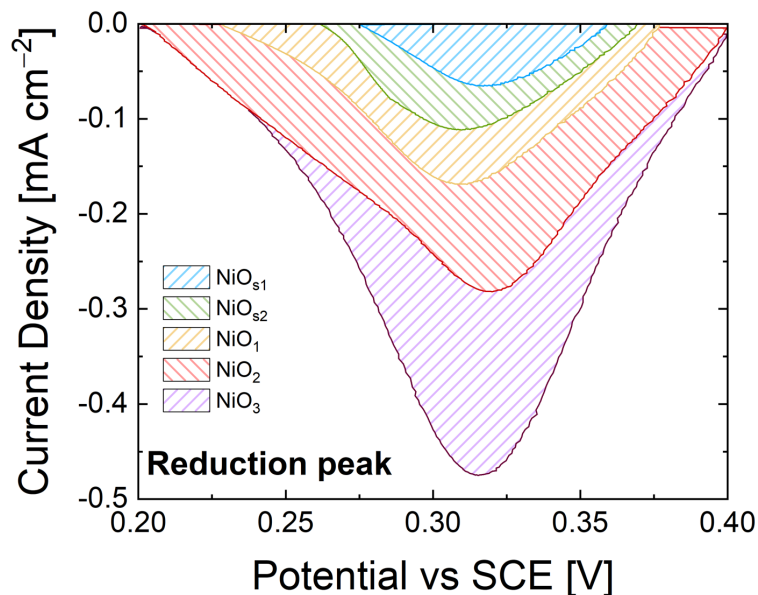


Figure P1.5.8: Reduction peaks of electrodes after the first backward scan during CV.

Figure P1.5.9(a) shows the values for TOF_{bulk} and $\text{TOF}_{\text{redox}}$ calculated for all the samples at fixed overpotential. In all cases $\text{TOF}_{\text{redox}}$ is approximately two orders of magnitude higher than TOF_{bulk} . By considering only TOF_{bulk} , it is easy to understand how the less massive sample (NiO_{S1}) has a higher TOF.

On the other hand, $\text{TOF}_{\text{redox}}$ designates as best electrocatalyst the NiO_{D2} sample. This discrepancy arises from the consideration that not all the catalyst mass deposited on GP is electrochemically active during the OER, but only a small fraction of the total mass contributes with active sites to the reaction [47,48]. To evaluate and compare the intrinsic catalytic activity, it is important to look at the activity per unit mass (mass activity, A mg^{-1}).

Mass activity is defined as the ratio between a fixed current density j and the catalyst loading. In our case we calculate the mass activity at a current density of 10 mA cm^{-2} by using the following expression:

$$\text{Mass activity} = \frac{j [\text{A cm}^{-2}]}{\text{catalyst loading} [\text{mg cm}^{-2}]} \quad (\text{P1.5.7})$$

Figure P1.5.9(b) compares the mass activity of the NiO catalysts at a current density of 10 mA cm^{-2} by considering both the total loading of μFs and only the redox contribution to the OER. The mass activity calculated from the redox fraction of the total mass is almost 2 orders of magnitude higher than in the bulk case. Such behavior reveals that increasing the mass of the μFs does not lead to a corresponding increase of the intrinsic OER performance, because of the decrease of the number of electrocatalyst active sites. In the massive samples, the electrochemical properties are weakened, leading to less effective material utilization [25].

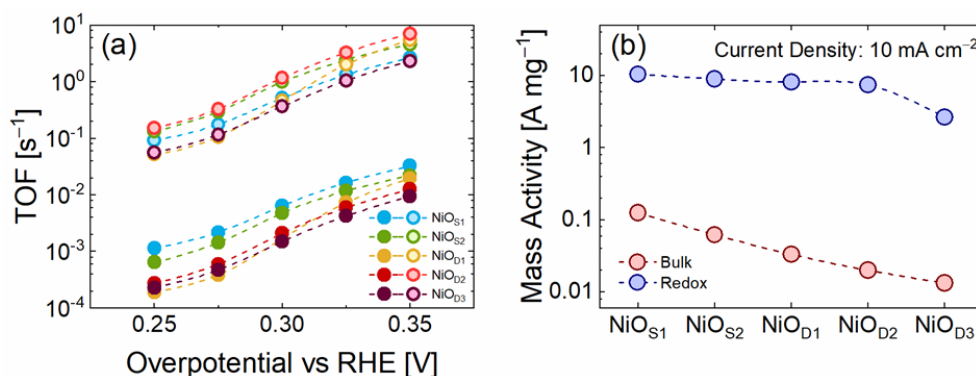


Figure P1.5.9: (a) TOF_{bulk} and $\text{TOF}_{\text{redox}}$ of NiO catalysts on GP; (b) bulk and redox mass activity at a current density of 10 mA cm^{-2} .

The obtained results should be compared with the state-of-art. As remarked by Kibsgaard, the state-of-art for OER is not represented by ruthenium, iridium, or ruthenium- and iridium-based materials, and comparison with these precious materials is irrelevant [17]. Table P1.5.4 compares state-of-the-art for TOF of NiO-based non-noble metal catalysts for the OER in alkaline media at an overpotential of 350 mV. The reaction rate ($\text{TOF}_{\text{redox}}$) of 6.98 s^{-1} for NiOD2 is, to the best of our knowledge, among the highest reported for non-noble catalysts in alkaline condition in literature [16,24,25,48-52]. Moreover, we compared the mass activity of our electrocatalysts at a constant current density of 10 mA cm^{-2} as a function of overpotential with the current state-of-art (Figure P1.5.10). In our samples, an increase of the mass loading leads to a reduction of the overpotential for the OER, but at the same time, a significant decrease of intrinsic activity. This comparison, together with the TOF values, makes our NiO μFs valuable candidates as anode electrodes for the OER.

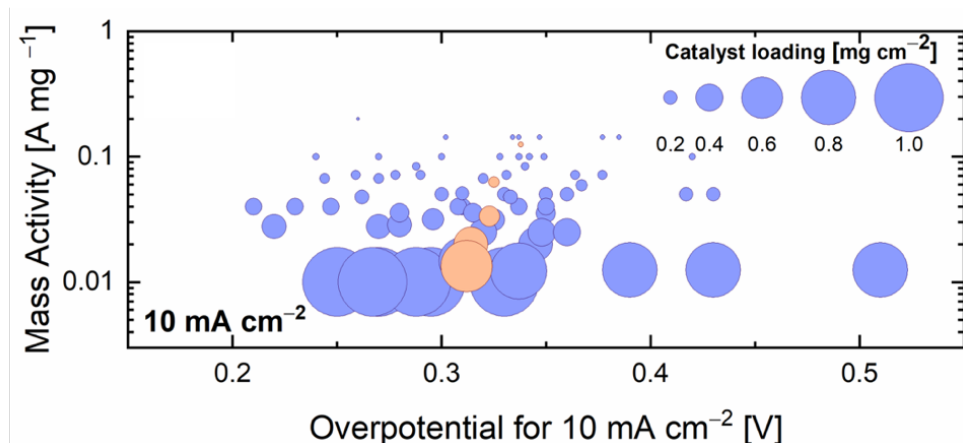


Figure P1.5.10: Mass activity at 10 mA cm^{-2} as a function of the overpotential and the catalyst loading [adapted from 17].

Finally, the durability of the NiO_{D_2} electrode was tested using chronopotentiometry. As displayed in Figure P1.5.11, the voltage at a current density of 10 mA cm^{-2} was slightly increasing up to 15 hours remaining lower than 0.4 V, demonstrating a good stability of the electrode.

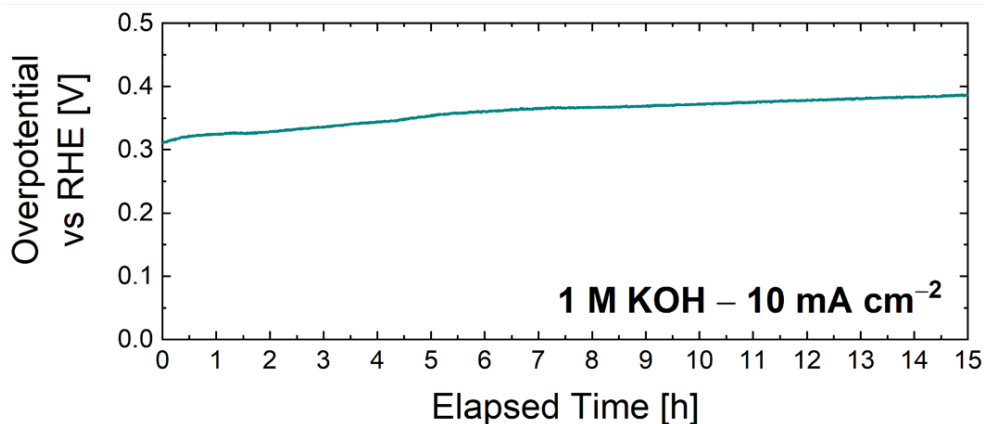


Figure P1.5.11: Chronopotentiometric test of NiO_{D_2} electrode.

Electrocatalyst material	Electrolyte	Overpotential [mV]	Tafel slope [mV dec ⁻¹]	TOF _{bulk} [s ⁻¹] at $\eta=350$ mV	TOF _{redox} [s ⁻¹] at $\eta=350$ mV	Ref.
NiO nanofibers	1M KOH	322	78	0.07	NA	[24]
NiTi oxide nanosheet	1M KOH	320	52	0.005	NA	[52]
NiO thin film	0.5M KOH	360	54	0.07	NA	[49]
Ni(OH) ₂ nanoplates	0.1M KOH	474	87	0.015 (490 mV)	NA	[50]
Ni/NiO nanoparticles	1M KOH	320	61	0.11	NA	[51]
NiO nanowalls	1M KOH	345	48	0.18	NA	[25]
Ni-P	1M KOH	335	71	0.05	0.62	[48]
NiO _{s1}	1M KOH	338	54-108	0.03	2.64	This work
NiO _{s2}	1M KOH	326	48-97	0.02	4.57	This work
NiO _{p1}	1M KOH	324	40-50	0.02	5.44	This work
NiO _{p2}	1M KOH	314	47-60	0.01	6.98	This work
NiO _{p3}	1M KOH	312	56-58	0.009	2.31	This work

Table P1.5.4: Overpotential (at a current density of 10 mA cm⁻²), Tafel slope and TOF for different electrodes.

Part 2.

P2.5.1 Physical Insights into Alkaline overall water splitting with NiO Microflowers Electrodes with ultra-low amount of Pt catalyst

The hydrogen evolution reaction (HER) is one of the most often studied electrocatalytic processes owing to its industrial and technological interest for producing hydrogen gas through a limited number of green reaction steps [1-11].

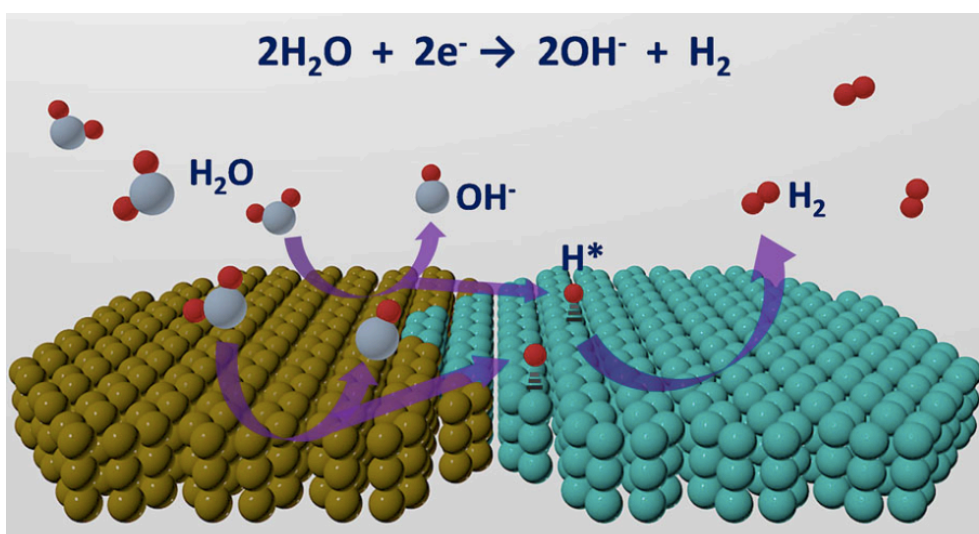


Figure P2.5.1: Hydrogen production steps [11].

The reaction occurs at cathode via a two-electrons reaction [12]:



From an industrial perspective on water electrolysis, HER is often conducted in alkaline media to achieve higher stability of the catalyst materials [11]. In alkaline medium, HER proceeds through two steps [8, 9, 13, 14]:

1. First, the catalyst splits a H_2O molecule (Volmer step) into a hydroxyl ion (OH^-) and an adsorbed hydrogen atom (H_{ads});
2. then, a hydrogen molecule is formed via either the interaction of the H_{ads} atom and water molecule (Heyrovsky step) or the combination of two H_{ads} atoms (Tafel step).

However, the kinetics of HER in alkaline medium are slow if compared with those in acid environment because of the low concentration of available protons. As a consequence, this process will require additional effort to obtain protons by water dissociation near or on electrode surface. The state-of-art HER catalyst is platinum (Pt) and its alloys, but the scarcity and cost of Pt, universally considered a critical raw material, limit its large-scale application for electrolysis [12]. In past decades, extensive research has been focused on the development of practical alternatives to Pt, as efficient and renewable energy sources [13, 15]. These have resulted in the identification of a myriad of promising HER catalysts free of precious metals such as sulfides, phosphides, carbides, nitrides, selenides, and borides [3, 16, 17].

Meanwhile, enhancing the efficiency of noble metals utilization may also provide a realistic approach to the development of high-performance and cost-effective catalysts. While Pt is well-known to be effective for the adsorption of H_{ads} atoms, the overall sluggish HER kinetics in alkaline solutions stems from the insufficient catalyzing capability of Pt toward the cleavage of the H – OH bond. A possible solution consists in the creation of catalysts with a combination of metal oxides and Pt, where the oxides promote the dissociation of H_2O and the nearby Pt facilitates the adsorption and recombination of H_{ads} into molecular H_2 [12, 15, 18].

The transition metal oxide NiO is considered a valuable candidate as active material for electrochemical water splitting thanks to its Earth abundance and low cost [19]. Furthermore, NiO nanostructures (interconnected networks, nanosheets, microflowers) increase electrolyte permeability through the active material, making more favorable the mass transport at the electrode-solution interface [20]. Thanks to unique catalytic properties, nanostructured NiO is often used as a high-performance OER catalyst [21-24]. Recent literature reports also evidenced that NiO is particularly interesting due to its high stability for HER in alkaline electrolytes [4].

Heterostructured materials on the nanoscale have exhibited great potential in this area. These classes of catalysts, with double or multiple types of active sites on the surface, exhibit remarkable advantages for the HER in alkaline solutions. A synergistic electronic interaction between the metal and the oxide has been proposed as the reason for the enhanced HER performance [4, 11, 18]. In particular, Pt-NiO catalysts can be the key for designing efficient and cheap catalyst at which Pt favors H^+ adsorption and NiO promotes the adsorption of OH^- species [25, 26].

Unfortunately, there are no reports on overall water splitting using only NiO-based materials (decorated or not) as bifunctional electrocatalysts, except for two ones [1, 24]. Mondal *et al.* tested the performance of porous hollow nanostructured NiO electrodes for overall water splitting taking advantage of their high surface areas, porous microstructures, inner hollow architectures [1]. Similarly, Bian *et al.* synthesized a hierarchically structured Pt/NiO/Ni/CNTs with a low loading of Pt NPs for efficient OER and HER, benefiting from the presence of the NiO/Ni heterojunction to boost the overall water splitting performance [25].

In this second part, we report a new strategy for overall water splitting electrodes, using NiO microflowers decorated with ultralow content of Pt nanoparticles (NPs). Our hybrid metal-oxide catalyst unfolds outstanding activity toward HER. An alkaline electrolyzer is finally tested using Pt-NiO μ Fs electrode and undecorated NiO μ Fs as cathode and anode, respectively. The presented electrode represents a valid strategy for the deployment of cost-effective electrocatalysts with a very small content of noble metal for widespread water electrocatalysis application.

P2.5.2 Experimental

P2.5.2.1 Preparation of the electrode

Pt nanoparticles (NPs) dispersion was produced through the green chemical reduction method described in Chapter 2 [17].

Graphene paper (GP) substrates (1 x 1.5 cm², 240 nm thick, Sigma Aldrich, St. Louis, MO, USA) were rinsed with deionized water and ethanol and dried in N₂ to clean the surface from any impurity. NiO μ Fs were deposited by drop casting by using 20 μ L of NiO dispersion. The samples were then dried on a hot plate at 80 °C for 10 minutes. Pt NPs were dispersed onto the electrode by subsequent addition of drops with NP dispersion in order to vary the catalyst loading. The mass of NiO (0.30 mg) on GP was measured by a Mettler Toledo MX5 Microbalance (sensitivity: 0.01 mg). Decorated samples are labelled according to the number of Pt dispersion drops (e.g. 5Pt-NiO indicates NiO catalyst decorated with 5 drops of Pt NPs dispersion).

P2.5.2.2 Characterization of Pt decorated NiO microflowers

Surface morphology was analyzed by using a Scanning Electron Microscope (SEM, Gemini field emission SEM Carl Zeiss SUPRA 25, Carl Zeiss Microscopy GmbH, Jena, Germany). SEM images were analyzed by using ImageJ software [27].

Transmission electron microscopy (TEM) analyses of Pt decorated NiO μ Fs dispersed on a TEM grid were performed with a Cs-probe-corrected JEOL JEM ARM200F microscope at a primary beam energy of 200 keV operated in scanning TEM (STEM) mode and equipped with a 100 mm² silicon drift detector for energy dispersive X-ray (EDX) spectroscopy. For EDX elemental mapping, the Pt X-rays signal was collected by scanning the same region multiple times with a dwell time of 1 ms. TEM images and EDX spectra were analyzed by using DigitalMicrograph® software [28].

The variation in the amount of Pt NPs on NiO μ Fs was analyzed by Rutherford backscattering spectrometry (RBS, 2.0 MeV He⁺ beam at normal incidence) with a 165° backscattering angle by using a 3.5 MV HVEE Singletron accelerator system (High Voltage Engineering Europa, Netherlands). RBS spectra were analyzed by using XRump software [29]. Once the Pt amount is known, the number of active Pt moles can be calculated as follows:

$$n_{\text{Pt}} [\text{g cm}^{-2}] = \frac{\text{Dose}_{\text{Pt}} [\text{at cm}^{-2}]}{N_A [\text{at mol}^{-1}]} \quad (\text{P2.5.1})$$

where Dose_{Pt} is the RBS Dose, representing the amount of Pt atoms per cm², and N_A is the Avogadro's number.

Electrochemical measurements were carried out at room temperature by using a VersaSTAT 4 potentiostat (Princeton Applied Research, USA) and a three-electrode setup with a graphite rod as counter electrode, a saturated calomel electrode (SCE) as reference electrode, and the prepared electrodes as working electrodes. 1 M KOH (pH 14, Sigma Aldrich, St. Louis, MO, USA) was used as supporting electrolyte. Cyclic voltammetry (CV) curves were recorded at a scan rate of 10 mV s⁻¹ in the potential range -0.7 ÷ -1.5 V vs SCE in order to stabilize the electrodes. The HER activities of decorated catalysts were investigated using linear sweep voltammetry (LSV) at scan rate of 5 mV s⁻¹ in the same potential windows of CVs. Electrochemical impedance spectroscopy (EIS) was performed with a superimposed 10 mV sinusoidal voltage in the frequency range 10⁴ ÷ 10⁻¹ Hz at a potential just after the onset potential (E_{onset} , the

minimum potential at which a reaction product is formed at an electrode). Tafel plots were extrapolated from polarization curves by plotting the overpotential (η) as a function of the log of the current density. Mott–Schottky (M-S) analyses were conducted on bare and decorated samples in the potential range 0 – 1 V vs. SCE, at 1000 Hz frequency. Chronopotentiometry (CP) analysis was employed to study the stability of the samples in a 1 M KOH solution for 15 hours at a constant current density of 10 mA cm^{-2} .

P2.5.3 Morphological and elemental characterization

Figures P2.5.2(a-b) show SEM images of NiO μ Fs on GP. Our catalyst recovers the surface of graphene electrode with an irregular thickness due to the agglomeration of μ Fs. After decoration, Pt NPs spread onto NiO μ Fs (Figure P2.5.2(c)). EDX elemental map in Figure P2.5.2(d) allowed us to confirm the effective presence of Pt decorating NiO catalyst.

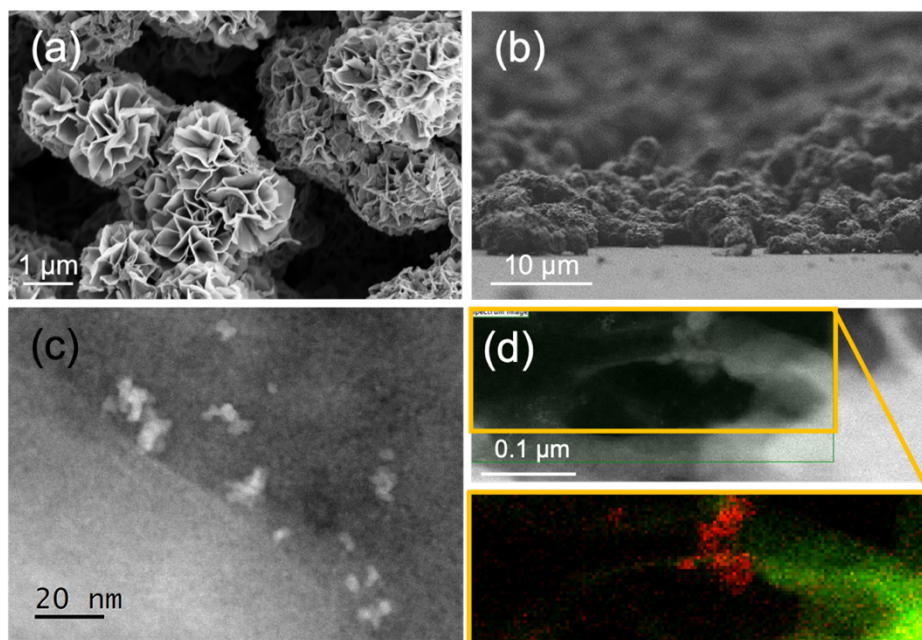


Figure P2.5.2: (a) SEM image of NiO μ Fs on GP; (b) tilted view of NiO μ Fs on GP; (c) STEM Z-contrast image of Pt NPs on NiO μ Fs (20Pt-NiO); (d) EDX elemental map of Pt NPs (red) on a single NiO sheet (green and yellow for Ni and O, respectively).

RBS analyses (Figure P2.5.3(a)) confirmed Pt presence and allowed us to quantify the Pt loading, by using a flat substrate covered with the same

drops containing Pt NP dispersion used for the electrode fabrication. We assume that after drop casting, the measured Pt loading on a flat substrate is the same of that on NiO μ Fs. The Pt loading is related to the area of Pt peak in the RBS spectrum (at around 1.8 MeV) [32]. As expected, Pt amount increases with the number of drops: 1.2×10^{16} at cm^{-2} , 1.8×10^{16} at cm^{-2} , 3.4×10^{16} at cm^{-2} , for 5, 10, and 20 drops, respectively (Figure P2.5.3(b)). Pt NP density cannot be verified by SEM analysis because of the rough surface and shadowing effect caused by NiO nanostructures.

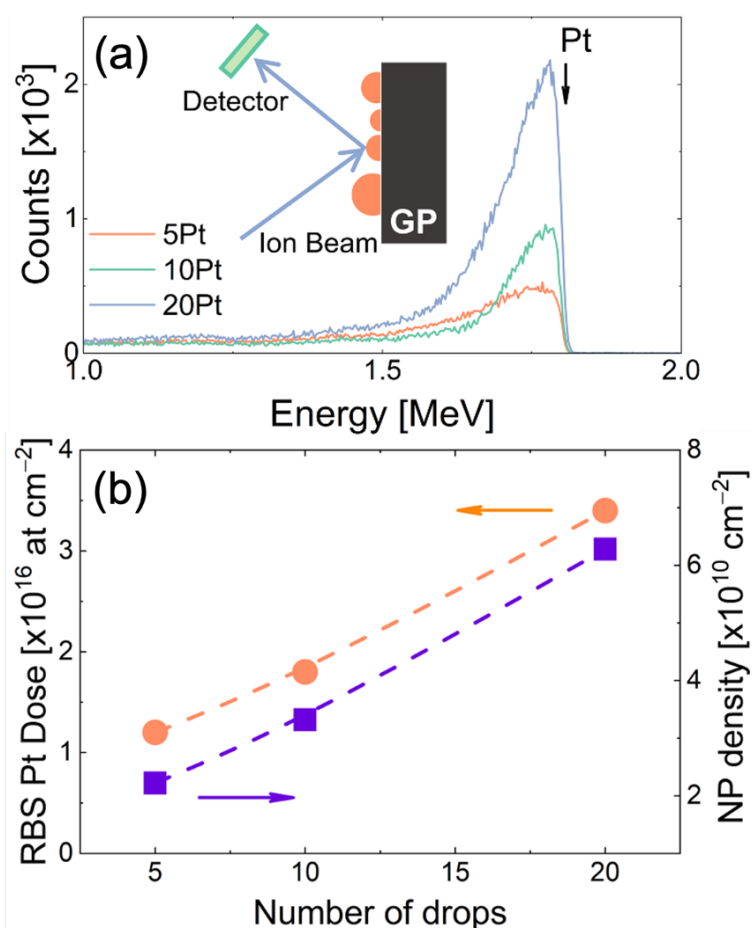


Figure P2.5.3: (a) RBS spectra of Pt NPs on a flat GP substrate; (b) RBS Pt dose and NP density as a function of the number of Pt colloidal solution drops.

Thus, the Pt amount (D_{RBS} , from RBS [31]) was joined with Pt NP diameter to evaluate the density N of NPs decorating NiO μ Fs, through the following relation [33, 34]:

$$D_{RBS} = N \rho_{at} V_{NP} \quad (\text{P2.5.2})$$

where ρ_{at} is the Pt atomic bulk density (6.62×10^{22} at cm^{-3}) and V_{NP} is the volume of a single NP (in cm^3) based on the size of NPs (measured from SEM images). Following these considerations, the NP density was found to vary from 2×10^{10} NPs cm^{-2} to 6.2×10^{10} NPs cm^{-2} (Figure P2.5.2(b)). Finally, from eq. (P2.5.1) the Pt loading can be easily calculated, confirming the extremely low content of Pt in our decorated electrodes.

P2.5.4 Electrochemical characterization – HER

To evaluate the electrochemical performance of bare and decorated NiO μ Fs on HER in alkaline conditions, electrochemical analyses were performed in 1 M KOH (Figure P2.5.4). Polarization curves (Figure P2.5.4(a)) clearly show how the presence of Pt drastically reduces the activation barrier for the H_2 production, confirmed by a variation in the onset potential and overpotential at a constant current density of 10 mA cm^{-2} from 247 to 66 mV (Table P2.5.1).

Two types of behavior can be distinguished as a function of the quantity of Pt:

- (i) for no (or ultralow) Pt loading, both overpotential and onset potential appear at relatively high voltages, indicating that high energies are required to overcome the adsorption of H^+ and subsequent production of H_2 steps;
- (ii) by increasing the density of NPs (10Pt and 20Pt), overpotential and onset potential drastically reduce pointing out an enhanced catalytic action of Pt against HER.

Tafel slopes of Pt decorated NiO μ Fs are reported in Figure P2.5.4(b). Pt decoration leads to a decrease of Tafel slope to a value of 82 mV dec^{-1} for 20Pt-NiO sample. Tafel slope values allow a deep understanding of HER catalytic mechanism.

Three possible pathways (illustrated in Figure P2.5.4(c)) for the HER reaction in alkaline medium can be distinguished [8, 9, 35]:

- (i) electrochemical hydrogen adsorption (Volmer step, $\text{H}_2\text{O} + \text{e}^- \rightarrow \text{H}_{\text{ads}} + \text{OH}^-$) at the active site of the catalyst;
- (ii) H_2 formation through an electrochemical desorption step (Heyrovsky step, $\text{H}_{\text{ads}} + \text{H}_2\text{O} + \text{e}^- \rightarrow \text{H}_2 + \text{OH}^-$);
- (iii) H_2 formation through a recombination step between two adsorbed hydrogen atoms (Tafel step: $\text{H}_{\text{ads}} + \text{H}_{\text{ads}} \rightarrow \text{H}_2$).

Usually, the rate-determining step (RDS) can be evaluated from the value of the Tafel slope [35-37]. Our values (by considering the kinetic analysis and mechanism for HER that are based on Butler-Volmer equation [36]) suggest that the RDS for our catalysts is represented by Volmer step and by the initial hydrogen adsorption. NiO-based materials have been widely proved to be optimal catalysts for OH^- adsorption [18, 25, 26]. The high Tafel slope value for bare semiconductor electrode clearly demonstrates that the HER proceeds much slower in NiO sample. Conversely, Pt loading causes a reduction of Tafel slopes (Figure P2.5.4(d)).

This evidence suggests that HER is limited by the hydrogen adsorption, with a poor efficiency in the NiO case. Conversely, the presence of Pt in decorated catalysts reveals an enhanced adsorption of hydrogen atoms on the surface. Pt decoration not only reduces the activation barrier for the activation of the HER (evidenced by the lowest overpotential for the most decorated sample), but also favors the hydrogen adsorption at the catalyst surface.

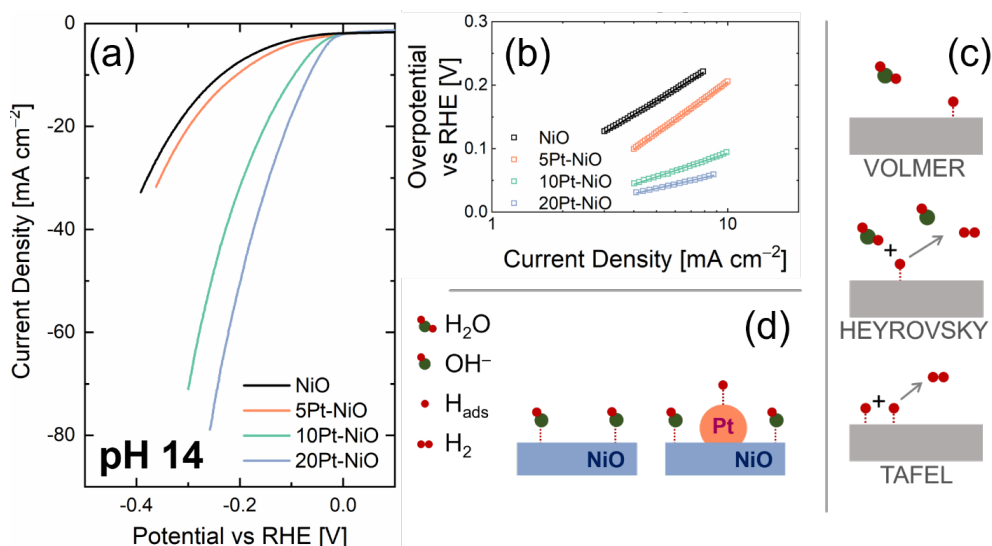


Figure P2.5.4: (a) Polarization curves, (b) Tafel plot of bare and decorated NiO μFs ; (c) HER mechanisms; (d) HER mechanism at NiO and Pt-NiO electrodes.

Sample	RBS Dose [at cm ⁻²]	NP density [NPs cm ⁻²]	Pt loading [μg cm ⁻²]	Overpotential [mV]	Tafel slope [mV dec ⁻¹]
NiO	-	-	-	247	224
5Pt-NiO	1.20·10 ¹⁶	1.0·10 ⁸	3.9	206	260
10Pt-NiO	1.80·10 ¹⁶	1.5·10 ⁸	5.8	94	115
20Pt-NiO	3.40·10 ¹⁶	2.9·10 ⁸	11.2	66	82

Table P2.5.1: Amount of Pt NPs for different drops and HER parameters.

Nyquist plots from EIS analysis in Figure P2.5.5(a) remark the role of Pt NPs in the HER. They were acquired in the so-called turnover region, just after the onset potential of each sample in order to appreciate a good HER activity [21, 39]. The experimental EIS spectra were fitted (continuous lines) by the Armstrong-Henderson equivalent circuit [10, 13, 14, 21, 39, 40-45] (Figure P2.5.4(b)) and the extracted fitting parameters are reported in Figure P2.5.5(c-d).

The adequately fitted experimental data reveal how the 5 parameters vary with Pt decoration (Figure P2.5.5(c-d)). R_u and C_{dl} do not appreciably change, as expected since the Pt NPs coverage is quite limited and most of the interface among NiO μ Fs and electrolyte is unchanged. A clear reduction in both R_{ct} and R_p with Pt loading indicates that Pt accelerates the electron transfer kinetics, probably enhancing the availability of electrons at surface. C_p , related to H_{ads} adsorption, decreases as the amount of Pt increases. Pt NPs act as effective active sites for hydrogen adsorption. Consequently, the higher the number of active sites, the lower their occupancy and therefore the value of C_p .

To quantitatively evaluate the effect of Pt decoration of NiO μ Fs we performed Mott-Schottky (M-S) analysis (Appendix C for details). The M-S plot typically reports the inverse of squared capacitance (C^{-2}) measured as a function of potential applied to the sample, as reported in Figure P2.5.6(a) [21, 46-51]. By increasing E , C^{-2} goes to zero as the applied potential increases, indicating the presence of a capacitance at the electrode-electrolyte interface. Such behavior is typical of a p -type semiconductor, as NiO is [52, 53].

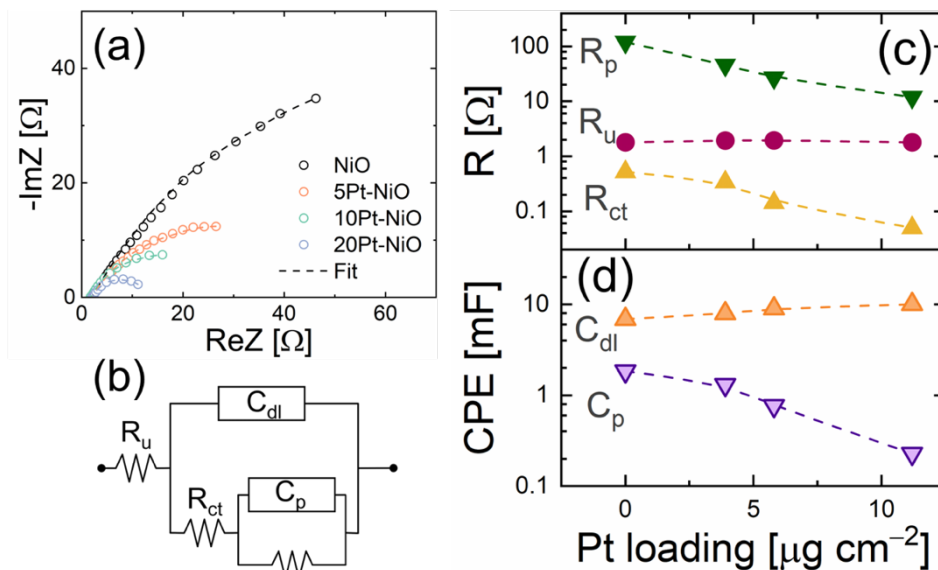


Figure P2.5.5: (a) Nyquist plot for bare and decorated electrodes; (b) Armstrong and Henderson equivalent circuit used to fit the experimental data; (c, d) behavior of equivalent circuit elements as a function of mass loading.

The intercept with x -axis (E_{FB}) represents the so-called flat band potential [46-51, 54-56]. For a planar semiconductor electrode, the quantity $\Delta E_{M-S} = E_{FB} - E_{OC}$ (where E_{OC} is the open circuit potential) represents the bending of the semiconductor energy bands [21] resulting from the alignment of the Fermi level of the electrode and the redox potential of the electrolyte (violet points in Figure P2.5.6(b)).

After the loading of Pt NPs, we observed a clear shift of E_{FB} towards more positive potential, up to 0.454 V in 20Pt-NiO case (Table P2.5.2). Even if our electrodes are nanostructured semiconductors, such evidence reveals a considerable difference in energy band bending due to Pt decoration. Moreover, it is possible to correlate the effect of decoration on energy band position of NiO with catalytic properties of the electrodes by considering the value of onset potential (E_{onset} , green points in Figure P2.5.5(b)).

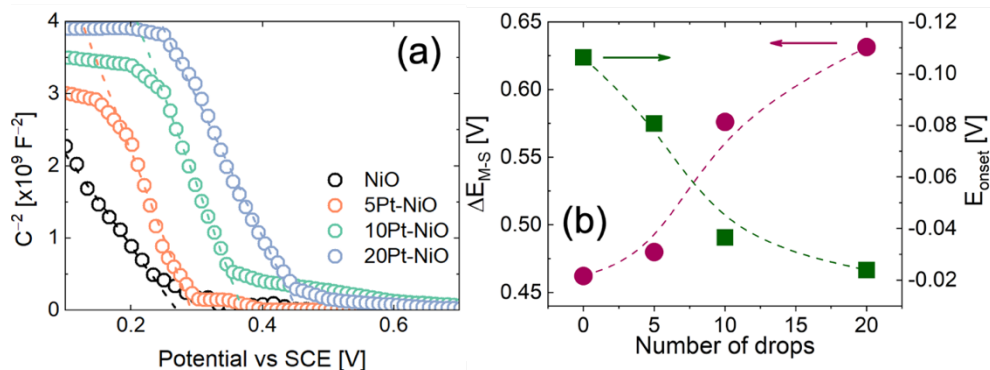


Figure P2.5.6: (a) Mott-Schottky plot of bare and Pt-decorated NiO electrodes; (b) variation of NiO energy band bending and onset potential as a function of the number of Pt solution drops.

Onset potential is usually considered an important indicator for the catalytic activity along with the exchange current density in electrocatalysis [31]. For a cathodic reaction, onset potential is the highest potential at which a reaction product (H_2 in our case) is formed at an electrode [57]. A commonly used method for the determination of this value is the intersection point between the tangent lines of the Faradaic and non-Faradaic [57-59]. Figure P2.5.7(b) clarifies the effect of Pt loading on ΔE_{M-S} and E_{onset} . As the amount of Pt NPs increases, the energy band bending grows, index of the creation of a nano Schottky junction at the metal-semiconductor interface [21].

Pt decoration increases the energy band bending, because of electron spillover effects, leading to space charge regions and localized electric field [34]. At the same time, a drastic reduction of E_{onset} is observed in presence of Pt NPs. These two evidences confirm that surface decoration of NiO μ Fs is highly effective in tuning the catalytic properties of our nanostructured electrode. The increase in bending of semiconductor energy levels leads to accumulation of electrons below the semiconductor surface, considerably reducing the activation barrier for H_2 production and making the HER mechanism more favorable at lower overpotentials.

Figure P2.5.7 schematizes the effect of Pt loading on NiO band position at the electrode-electrolyte interface.

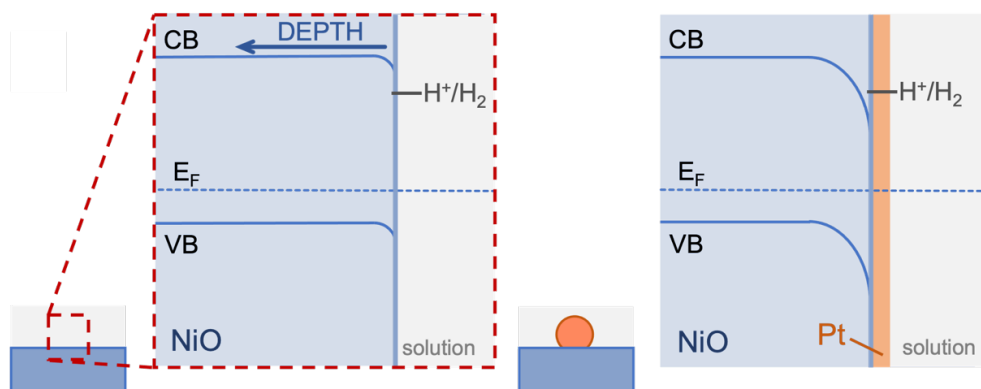


Figure P2.5.7: Scheme of the modification of energy levels at the semiconductor-electrolyte interface for bare NiO and Pt-NiO catalysts.

Sample	Pt drops	E_{OC} [V]	E_{FB} [V]	ΔE_{M-S} [V]	E_{onset} [V]
NiO	-	-0.192	0.270	0.462	-0.106
5Pt-NiO	5	-0.187	0.292	0.479	-0.081
10Pt-NiO	10	-0.206	0.370	0.576	-0.036
20Pt-NiO	20	-0.178	0.454	0.632	-0.024

Table P2.5.2: Values of open circuit potential, flat band potential, energy barrier, and onset potential for bare and decorated samples.

As previously said, TOF is a crucial parameter for evaluating the HER performance of a catalyst because it reflects the intrinsic electrocatalytic activity of the electrode [2, 17, 31, 60]. As presented in Figure P2.5.8(a), Pt-decorated samples show markedly high TOF values. It is worth to note that the TOF value of 2.07 s^{-1} (at an overpotential of 50 mV) found for 20Pt-NiO is comparable (and even superior) to those reported in literature and confirms that the present Pt NP decorated catalyst owns extraordinary efficiency of hydrogen generation (see Table P2.5.3).

The obtained results are now compared with the state-of-art. Figure P2.5.8(b) shows the comparison of mass activity measured at 10 mA cm^{-2} and the overpotential for 10 mA cm^{-2} (based on geometric area) for our

decorated electrodes with other Pt-based catalysts under alkaline conditions [2].

In our samples, an increase of the mass loading leads to a reduction of the overpotential for the HER, without a significant decrease of intrinsic activity. This comparison, together with the TOF values, makes our Pt decorated NiO μ Fs valuable candidates as cathode electrodes for the HER.

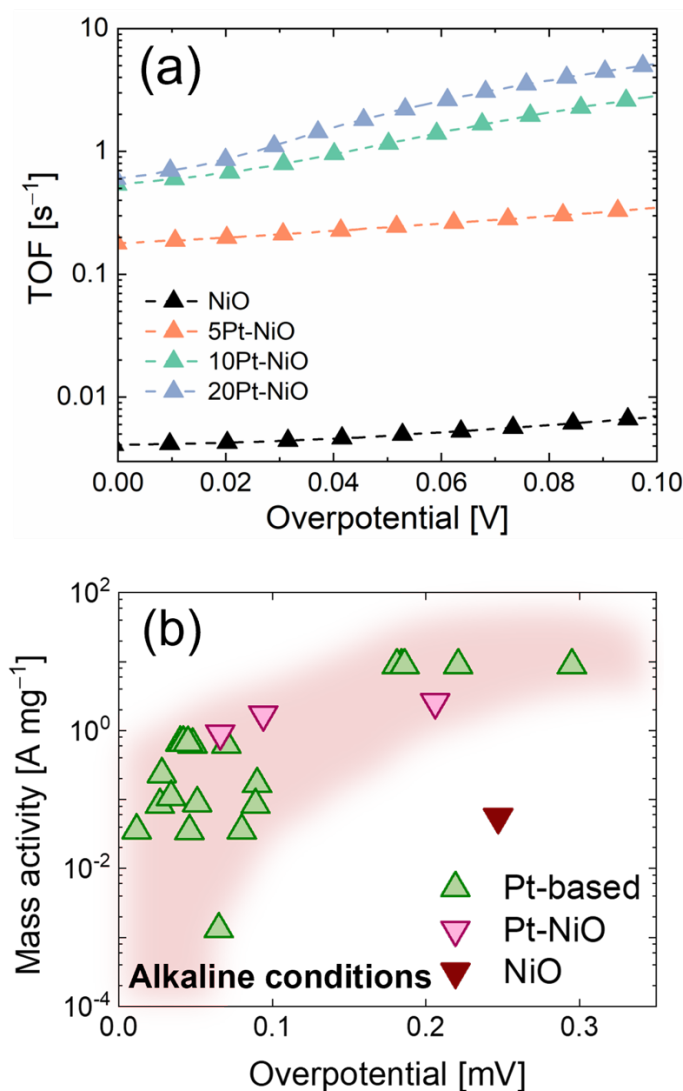


Figure P2.5.8: (a) TOF of Pt-NiO catalysts on GP; mass activity at 10 mA cm^{-2} as a function of the overpotential and the catalyst loading [adapted from 2].

Electrode	Electrolyte	Overpotential at 10 mA cm ⁻² [mV]	Tafel slope [mV dec ⁻¹]	TOF at 50 mV [s ⁻¹]	Mass activity at 10 mA cm ⁻² [A mg ⁻¹]	Ref.
Pt/C/Ni(OH) ₂		90			0.17	1
Pt-NiO/C	1M KOH	41.7	78.8	-	5.35	2
NiS/Ni ₂ P	1M KOH	120	71	-	-	3
NiO/NF	1M KOH	69.9	82	-	-	4
NiO/Ni@NCNTs	1M KOH	87.5	80	-	-	5
Hollow NiO	1M KOH	424	105	-	-	6
Pt-NiO/NF	1M KOH	100 (50 mV)	-	-	-	7
NiO/NF	1M KOH	70	65	0.6 (0V)	-	8
NiO/Ni-CNT	1M KOH	80	82	-	0.036	9
Ni/NiO	1M KOH	226	135	-	-	10
Pt@Ni/NF	1M KOH	34	30	~0.5	0.25	11
CoMnP/Ni ₂ P/NiFe	1M KOH	204	95	-	-	12
Pt@2D-Ni(OH) ₂	0.1 M KOH	123 (4.2mAcm ⁻²)	119	-	8.85	13
Pt/NiO/Ni/CNTs	1M KOH	97	65	-	0.14 (50 mV)	14
Pt/Ni-P	1M KOH	22	30	1.78	-	15
NiO	1M KOH	247	224	0.005	0.06	Our work
5Pt-NiO	1M KOH	206	260	0.24	2.57	Our work
10Pt-NiO	1M KOH	94	115	1.16	1.71	Our work
20Pt-NiO	1M KOH	66	82	2.07	0.91	Our work

Table P2.5.3: HER performance for different cathode materials.

P2.5.5 Overall water splitting

Motivated by the excellent HER performance of catalysts and the high OER activity of our previously reported NiO μ Fs on GP [21], we investigated the overall water-splitting performance under alkaline condition by employing 20Pt-NiO μ Fs as the cathode and NiO μ Fs as the anode (a scheme of the Pt-NiO||NiO is reported in Figure P2.5.9(a)). Our as-constructed alkaline electrolytic cell requires a low potential of 1.57 V to afford a current density of 10 mA cm⁻² (Figure P2.5.9(b)), which is comparable or smaller to other electrocatalysts reported in Table P2.5.4.

In addition, the overall water-splitting durability of the two electrodes was tested using chronopotentiometry for 24 hours (Figure P2.5.9(c)) showing a good stability over prolonged times (with an increase of overpotential of 50 mV after 24 hours).

Our results reveal that the present Pt-NiO||NiO electrodes represent highly efficient electrocatalysts.

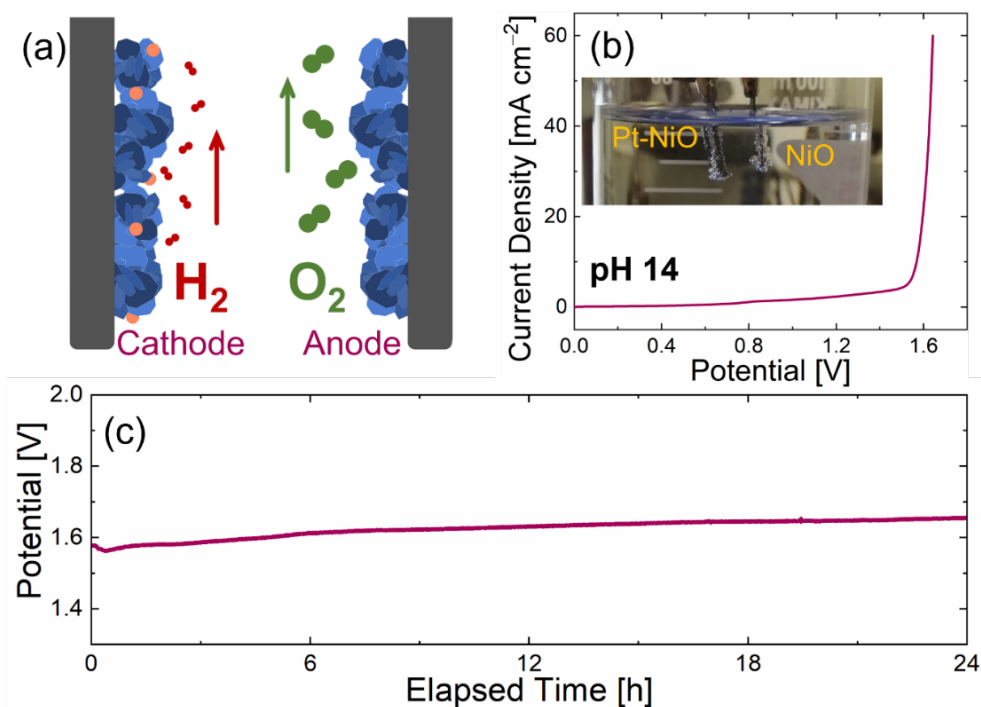


Figure P2.5.9: (b) Polarization curve of the two-electrode electrolyzer Pt-NiO||NiO for overall water splitting under alkaline condition (1M KOH, pH 14); (c) long-term chronopotentiometric stability test of Pt-NiO||NiO.

Catalyst material	Electrolyte	Overall water splitting overpotential at 10 mAcm ⁻² [V]	Ref.
Pt/NiO/Ni/CNT-3 Pt/NiO/Ni/CNT-3	1M KOH	1.61	61
NiO/Ni-CNT NiFe LDH	1 M KOH	1.50 (20 mAcm ⁻²)	62
Pt/Ni-P/NF Ni-P/NF	1 M KOH	1.64	17
Pt-NiO NiO	1M KOH	1.57	This work

Table P2.5.4: Summary of various Ni-based Electrocatalysts for Overall Water Splitting.

Conclusions

In conclusion, we developed a high-efficiency OER and HER catalyst by dispersing low-cost synthesized bare or decorated NiO microflowers (μ Fs) onto a GP substrate. By varying the loading of μ Fs and Pt NPs the role of active sites was elucidated with respect to the total mass of electrocatalyst. The NiO catalyst with optimized mass loading and material dispersion on GP shows an overpotential for OER of 314 mV at current density of 10 mA cm⁻², a promisingly low Tafel slope of 47 mV dec⁻¹.

The Pt-NiO catalyst with optimized NP loading shows an overpotential for HER of only 66 mV at current density of 10 mA cm⁻² and a Tafel slope of 82 mV dec⁻¹. An alkaline all NiO-based electrolyzer was developed by using Pt-NiO as cathode and bare NiO as anode, requiring a low potential of 1.57 V to afford a current density of 10 mA cm⁻² and a good long-term stability. The high activity, and low-cost of the present Pt-NiO μ Fs pave the way for large-scale and long-term applications of NiO-based catalysts for overall water splitting.

References

Part 1

- [1] P. C. K. Vesborg, B. Seger and I. Chorkendorff, *J. Phys. Chem. Lett.*, 2021, DOI:10.1021/acs.jpcclett.5b00306.
- [2] J. M. Gonçalves, T. A. Matias, K. C. F. Toledo and K. Araki, in *Advances in Inorganic Chemistry*, 2019, DOI: 10.1016/bs.adioch.2019.03.002.
- [3] J. Zhu, L. Hu, P. Zhao, L. Y. S. Lee and K. Y. Wong, *Chem. Rev.*, 2020, DOI:10.1021/acs.chemrev.9b00248.
- [4] A. R. Zeradjanin, J. Masa, I. Spanos and R. Schlögl, *Front. Energy Res.*, 2021, DOI:10.3389/fenrg.2020.613092.
- [5] W. Li, D. Xiong, X. Gao and L. Liu, *Chem. Commun.*, 2019, DOI:10.1039/c9cc02845e.
- [6] S. Anantharaj, S. R. Ede, K. Sakthikumar, K. Karthick, S. Mishra and S. Kundu, *ACS Catal.*, 2016, DOI:10.1021/acscatal.6b02479.
- [7] G. Li, L. Anderson, Y. Chen, M. Pan and P. Y. Abel Chuang, *Sustain. Energy Fuels*, 2018, DOI:10.1039/c7se00337d.
- [8] R. L. Doyle and M. E. G. Lyons, in *Photoelectrochemical Solar Fuel Production: From Basic Principles to Advanced Devices*, 2016.
- [9] X. Tian, P. Zhao and W. Sheng, *Adv. Mater.*, 2019, DOI:10.1002/adma.201808066.
- [10] S. Kiemel, T. Smolinka, F. Lehner, J. Full, A. Sauer and R. Mieke, *Int. J. Energy Res.*, , DOI:10.1002/er.6487.
- [11] N. T. Suen, S. F. Hung, Q. Quan, N. Zhang, Y. J. Xu and H. M. Chen, *Chem. Soc. Rev.*, 2017, DOI:10.1039/c6cs00328a.

- [12] A. H. Tkaczyk, A. Bartl, A. Amato, V. Lapkovskis and M. Petranikova, *J. Phys. D. Appl. Phys.*, 2018, DOI:10.1088/1361-6463/aaba99.
- [13] G. Carollo, A. Garbujo, F. Mauvy and A. Glisenti, *Energy and Fuels*, 2020, DOI:10.1021/acs.energyfuels.0c01678.
- [14] A. I. Inamdar, H. S. Chavan, S. M. Pawar, H. Kim and H. Im, *Int. J. Energy Res.*, 2019, DOI:10.1002/er.5026.
- [15] Y. Matsumoto and E. Sato, *Mater. Chem. Phys.*, 1986, DOI:10.1016/0254-0584(86)90045-3.
- [16] C. Roy, B. Sebok, S. B. Scott, E. M. Fiordaliso, J. E. Sørensen, A. Bodin, D. B. Trimarco, C. D. Damsgaard, P. C. K. Vesborg, O. Hansen, I. E. L. Stephens, J. Kibsgaard and I. Chorkendorff, *Nat. Catal.*, 2018, DOI:10.1038/s41929-018-0162-x.
- [17] J. Kibsgaard and I. Chorkendorff, *Nat. Energy*, 2019, DOI:10.1038/s41560-019-0407-1.
- [18] R. L. Doyle, I. J. Godwin, M. P. Brandon and M. E. G. Lyons, *Phys. Chem. Chem. Phys.*, 2013, DOI:10.1039/c3cp51213d.
- [19] E. Fabbri, A. Habereder, K. Waltar, R. Kötz and T. J. Schmidt, *Catal. Sci. Technol.*, 2014, DOI:10.1039/c4cy00669k.
- [20] M. E. G. Lyons and M. P. Brandon, *Int. J. Electrochem. Sci.*, 2008, 3, 1425-1462.
- [21] P. Manivasakan, P. Ramasamy and J. Kim, *RSC Adv.*, 2015, DOI:10.1039/c5ra01739d.
- [22] D. Takimoto, S. Hideshima and W. Sugimoto, *ACS Appl. Nano Mater.*, 2021, DOI:10.1021/acsanm.1c01328.
- [23] W. Yuan, C. Li, M. Zhao, J. Zhang, C. M. Li and S. P. Jiang, *Electrochim. Acta*, 2020, DOI:10.1016/j.electacta.2020.136118.

- [24] V. D. Silva, T. A. Simões, J. P. F. Grilo, E. S. Medeiros and D. A. Macedo, *J. Mater. Sci.*, 2020, DOI:10.1007/s10853-020-04481-1.
- [25] S. Cosentino, M. Urso, G. Torrisi, S. Battiato, F. Priolo, A. Terrasi and S. Mirabella, *Mater. Adv.*, 2020, DOI:10.1039/d0ma00467g.
- [26] R. Subbaraman, D. Tripkovic, K. C. Chang, D. Strmcnik, A. P. Paulikas, P. Hirunsit, M. Chan, J. Greeley, V. Stamenkovic and N. M. Markovic, *Nat. Mater.*, 2012, DOI:10.1038/nmat3313.
- [27] B. P. Reddy, K. Mallikarjuna, M. Kumar, M. C. Sekhar, Y. Suh and S. H. Park, *Ceram. Int.*, 2021, DOI:10.1016/j.ceramint.2020.09.172.
- [28] A. Mondal, A. Paul, D. N. Srivastava and A. B. Panda, *Int. J. Hydrogen Energy*, 2018, DOI:10.1016/j.ijhydene.2018.06.139.
- [29] P. T. Babar, A. C. Lokhande, M. G. Gang, B. S. Pawar, S. M. Pawar and J. H. Kim, *J. Ind. Eng. Chem.*, 2018, DOI:10.1016/j.jiec.2017.11.037.
- [30] Z. Pu, Q. Liu, A. M. Asiri and X. Sun, *J. Appl. Electrochem.*, 2014, DOI:10.1007/s10800-014-0743-6.
- [31] K. O. Iwu, A. Lombardo, R. Sanz, S. Scirè and S. Mirabella, *Sensors Actuators, B Chem.*, 2016, DOI:10.1016/j.snb.2015.10.109.
- [32] M. Urso, G. Pellegrino, V. Strano, E. Bruno, F. Priolo and S. Mirabella, *Nanotechnology*, 2018, DOI:10.1088/1361-6528/aaacb6.
- [33] ImageJ. ImageJ. Available online: www.imagej.nih.gov.
- [34] Thompson, M. Xrump. Available online: www.genplot.com.
- [35] DigitalMicrograph®. Available online: <https://www.gatan.com/products/tem-analysis/gatan-microscopy-suite-software>.
- [36] M. B. Stevens, L. J. Enman, A. S. Batchellor, M. R. Cosby, A. E. Vise, C. D. M. Trang and S. W. Boettcher, *Chem. Mater.*, 2017, DOI:10.1021/acs.chemmater.6b02796.

- [37] T. L. Alford, L. C. Feldman and J. W. Mayer, *Fundamentals of nanoscale film analysis*, 2007, DOI:10.1007/978-0-387-29261-8.
- [38] S. Anantharaj and S. Noda, *ChemElectroChem*, 2020, DOI:10.1002/celec.202000515.
- [39] J. E. B. Randles, *Faraday Discuss.*, 1947, DOI:10.1039/DF9470100011.
- [40] R. D. Armstrong and M. Henderson, *J. Electroanal. Chem.*, 1972, DOI:10.1016/S0022-0728(72)80477-7.
- [41] E. B. Castro, C. A. Gervasi and J. R. Vilche, *J. Appl. Electrochem.*, 1998, DOI:10.1023/A:1003488409147.
- [42] B. E. Conway and T. C. Liu, *Langmuir*, 1990, DOI:10.1021/la00091a044.
- [43] E. A. Franceschini, G. I. Lacconi and H. R. Corti, *Electrochim. Acta*, 2015, DOI:10.1016/j.electacta.2015.01.110.
- [44] N. Krstajić, M. Popović, B. Grgur, M. Vojnović and D. Šepa, *J. Electroanal. Chem.*, 2001, DOI:10.1016/S0022-0728(01)00590-3.
- [45] G. Wu, N. Li, D. R. Zhou, K. Mitsuo and B. Q. Xu, *J. Solid State Chem.*, 2004, DOI:10.1016/j.jssc.2004.06.027.
- [46] M. E. G. Lyons and M. P. Brandon, *J. Electroanal. Chem.*, 2010, DOI:10.1016/j.jelechem.2009.11.024.
- [47] S. Anantharaj, P. E. Karthik and S. Noda, *Angew. Chemie - Int. Ed.*, 2021, DOI:10.1002/anie.202110352.
- [48] S. Battiato, M. Urso, S. Cosentino, A. L. Pellegrino, S. Mirabella and A. Terrasi, *Nanomaterials*, 2021, DOI:10.3390/nano11113010.
- [49] A. C. Pebley, E. Decolvenaere, T. M. Pollock and M. J. Gordon, *Nanoscale*, 2017, DOI:10.1039/c7nr04302c.

[50] X. Zhou, Z. Xia, Z. Zhang, Y. Ma and Y. Qu, *J. Mater. Chem. A*, 2014, DOI:10.1039/c4ta01952k.

[51] F. E. Sarac Oztuna, T. Beyazay and U. Unal, *J. Phys. Chem. C*, , DOI:10.1021/acs.jpcc.9b07460.

[52] Y. Zhao, X. Jia, G. Chen, L. Shang, G. I. N. Waterhouse, L. Z. Wu, C. H. Tung, D. Ohare and T. Zhang, *J. Am. Chem. Soc.*, 2016, DOI:10.1021/jacs.6b01606.

Part 2

[1] Mondal A, Paul A, Srivastava DN, Panda AB. NiO hollow microspheres as efficient bifunctional electrocatalysts for Overall Water-Splitting. *Int J Hydrogen Energy* 2018. <https://doi.org/10.1016/j.ijhydene.2018.06.139>.

[2] Kibsgaard J, Chorkendorff I. Considerations for the scaling-up of water splitting catalysts. *Nat Energy* 2019. <https://doi.org/10.1038/s41560-019-0407-1>.

[3] Bu X, Wei R, Gao W, Lan C, Ho JC. A unique sandwich structure of a CoMnP/Ni₂P/NiFe electrocatalyst for highly efficient overall water splitting. *J Mater Chem A* 2019. <https://doi.org/10.1039/c9ta02551k>.

[4] Faid AY, Barnett AO, Seland F, Sunde S. Ni/NiO nanosheets for alkaline hydrogen evolution reaction: In situ electrochemical-Raman study. *Electrochim Acta* 2020. <https://doi.org/10.1016/j.electacta.2020.137040>.

[5] Li X, Zhao L, Yu J, Liu X, Zhang X, Liu H, et al. Water Splitting: From Electrode to Green Energy System. *Nano-Micro Lett* 2020. <https://doi.org/10.1007/s40820-020-00469-3>.

[6] Doyle RL, Lyons MEG. The oxygen evolution reaction: Mechanistic concepts and catalyst design. *Photoelectrochem. Sol. Fuel Prod. From*

Basic Princ. to Adv. Devices, 2016. https://doi.org/10.1007/978-3-319-29641-8_2.

[7] Suen NT, Hung SF, Quan Q, Zhang N, Xu YJ, Chen HM. Electrocatalysis for the oxygen evolution reaction: Recent development and future perspectives. *Chem Soc Rev* 2017. <https://doi.org/10.1039/c6cs00328a>.

[8] Safizadeh F, Ghali E, Houlachi G. Electrocatalysis developments for hydrogen evolution reaction in alkaline solutions - A Review. *Int J Hydrogen Energy* 2015. <https://doi.org/10.1016/j.ijhydene.2014.10.109>.

[9] Lasia A. Mechanism and kinetics of the hydrogen evolution reaction. *Int J Hydrogen Energy* 2019. <https://doi.org/10.1016/j.ijhydene.2019.05.183>.

[10] Franceschini EA, Lacconi GI, Corti HR. Kinetics of the hydrogen evolution on nickel in alkaline solution: New insight from rotating disk electrode and impedance spectroscopy analysis. *Electrochim Acta* 2015. <https://doi.org/10.1016/j.electacta.2015.01.110>.

[11] Wei J, Zhou M, Long A, Xue Y, Liao H, Wei C, et al. Heterostructured Electrocatalysts for Hydrogen Evolution Reaction Under Alkaline Conditions. *Nano-Micro Lett* 2018. <https://doi.org/10.1007/s40820-018-0229-x>.

[12] Stephens IEL, Chorkendorff I. Minimizing the use of platinum in hydrogen-evolving electrodes. *Angew Chemie - Int Ed* 2011. <https://doi.org/10.1002/anie.201005921>.

[13] Doyle RL, Godwin IJ, Brandon MP, Lyons MEG. Redox and electrochemical water splitting catalytic properties of hydrated metal oxide modified electrodes. *Phys Chem Chem Phys* 2013. <https://doi.org/10.1039/c3cp51213d>.

[14] Nikolic VM, Maslovara SL, Tasic GS, Brdaric TP, Lausevic PZ, Radak BB, et al. Kinetics of hydrogen evolution reaction in alkaline electrolysis on a Ni cathode in the presence of Ni-Co-Mo based ionic

activators. *Appl Catal B Environ* 2015. <https://doi.org/10.1016/j.apcatb.2015.05.012>.

[15] Chen ZJ, Cao GX, Gan LY, Dai H, Xu N, Zang MJ, et al. Highly Dispersed Platinum on Honeycomb-like NiO@Ni Film as a Synergistic Electrocatalyst for the Hydrogen Evolution Reaction. *ACS Catal* 2018. <https://doi.org/10.1021/acscatal.8b02212>.

[16] Hou Y, Lohe MR, Zhang J, Liu S, Zhuang X, Feng X. Vertically oriented cobalt selenide/NiFe layered-double-hydroxide nanosheets supported on exfoliated graphene foil: An efficient 3D electrode for overall water splitting. *Energy Environ Sci* 2016. <https://doi.org/10.1039/c5ee03440j>.

[17] Battiato S, Bruno L, Terrasi A, Mirabella S. Superior Performances of Electroless-Deposited Ni-P Films Decorated with an Ultralow Content of Pt for Water-Splitting Reactions. *ACS Appl Energy Mater* 2022. <https://doi.org/10.1021/acsaem.1c03880>.

[18] Subbaraman R, Tripkovic D, Chang KC, Strmcnik D, Paulikas AP, Hirunsit P, et al. Trends in activity for the water electrolyser reactions on 3d M(Ni,Co,Fe,Mn) hydr(oxy)oxide catalysts. *Nat Mater* 2012. <https://doi.org/10.1038/nmat3313>.

[19] Gong M, Wang DY, Chen CC, Hwang BJ, Dai H. A mini review on nickel-based electrocatalysts for alkaline hydrogen evolution reaction. *Nano Res* 2016. <https://doi.org/10.1007/s12274-015-0965-x>.

[20] Silva VD, Simões TA, Grilo JPF, Medeiros ES, Macedo DA. Impact of the NiO nanostructure morphology on the oxygen evolution reaction catalysis. *J Mater Sci* 2020. <https://doi.org/10.1007/s10853-020-04481-1>.

[21] Bruno L, Scuderi M, Priolo F, Mirabella S. Enhanced Electrocatalytic Activity of low-cost NiO Microflowers on Graphene Paper for Oxygen Evolution Reaction. *Sustain. Energy & Fuels* 2022. <https://doi.org/10.1039/D2SE00829G>.

- [22] Cosentino S, Urso M, Torrisi G, Battiato S, Priolo F, Terrasi A, et al. High intrinsic activity of the oxygen evolution reaction in low-cost NiO nanowall electrocatalysts. *Mater Adv* 2020. <https://doi.org/10.1039/d0ma00467g>.
- [23] Manivasakan P, Ramasamy P, Kim J. Reactive-template fabrication of porous NiO nanowires for electrocatalytic O₂ evolution reaction. *RSC Adv* 2015. <https://doi.org/10.1039/c5ra01739d>.
- [24] Yuan W, Li C, Zhao M, Zhang J, Li CM, Jiang SP. In situ self-assembled 3-D interconnected pristine graphene supported NiO nanosheets as superior catalysts for oxygen evolution. *Electrochim Acta* 2020. <https://doi.org/10.1016/j.electacta.2020.136118>.
- [25] Bian Y, Wang H, Gao Z, Hu J, Liu D, Dai L. A facile approach to high-performance trifunctional electrocatalysts by substrate-enhanced electroless deposition of Pt/NiO/Ni on carbon nanotubes. *Nanoscale* 2020. <https://doi.org/10.1039/d0nr03378b>.
- [26] Li Q, Cheng W, Zeng C, Zheng X, Sun L, Jiang Q, et al. Facile and rapid synthesis of Pt-NiO_x/NiF composites as a highly efficient electrocatalyst for alkaline hydrogen evolution. *Int J Hydrogen Energy* 2022. <https://doi.org/10.1016/j.ijhydene.2021.12.101>.
- [27] ImageJ. Available on <https://imagej.nih.gov/ij/index.html>.
- [28] DigitalMicrograph®. Available online: <https://www.gatan.com/products/tem-analysis/gatan-microscopy-suite-software>.
- [29] Thompson, M. Xrump. Available online: www.genplot.com.
- [30] Stevens MB, Enman LJ, Batchellor AS, Cosby MR, Vise AE, Trang CDM, et al. Measurement techniques for the study of thin film heterogeneous water oxidation electrocatalysts. *Chem Mater* 2017. <https://doi.org/10.1021/acs.chemmater.6b02796>.

- [31] Anantharaj S, Karthik PE, Noda S. The Significance of Properly Reporting Turnover Frequency in Electrocatalysis Research. *Angew Chemie - Int Ed* 2021. <https://doi.org/10.1002/anie.202110352>.
- [32] Alford TL, Feldman LC, Mayer JW. Fundamentals of nanoscale film analysis. 2007. <https://doi.org/10.1007/978-0-387-29261-8>.
- [33] Bruno L, Urso M, Shacham-Diamand Y, Priolo F, Mirabella S. Role of substrate in au nanoparticle decoration by electroless deposition. *Nanomaterials* 2020;10. <https://doi.org/10.3390/nano10112180>.
- [34] Bruno L, Strano V, Scuderi M, Franzò G, Priolo F, Mirabella S. Localized Energy Band Bending in ZnO Nanorods Decorated with Au Nanoparticles. *Nanomaterials* 2021;11:2718. <https://doi.org/10.3390/nano11102718>.
- [35] Zheng Y, Jiao Y, Vasileff A, Qiao SZ. The Hydrogen Evolution Reaction in Alkaline Solution: From Theory, Single Crystal Models, to Practical Electrocatalysts. *Angew Chemie - Int Ed* 2018. <https://doi.org/10.1002/anie.201710556>.
- [36] Tian X, Zhao P, Sheng W. Hydrogen Evolution and Oxidation: Mechanistic Studies and Material Advances. *Adv Mater* 2019. <https://doi.org/10.1002/adma.201808066>.
- [37] Shinagawa T, Garcia-Esparza AT, Takanabe K. Insight on Tafel slopes from a microkinetic analysis of aqueous electrocatalysis for energy conversion. *Sci Rep* 2015. <https://doi.org/10.1038/srep13801>.
- [38] Murthy AP, Theerthagiri J, Madhavan J. Insights on Tafel Constant in the Analysis of Hydrogen Evolution Reaction. *J Phys Chem C* 2018. <https://doi.org/10.1021/acs.jpcc.8b07763>.
- [39] Anantharaj S, Noda S. Appropriate Use of Electrochemical Impedance Spectroscopy in Water Splitting Electrocatalysis. *ChemElectroChem* 2020. <https://doi.org/10.1002/celec.202000515>.

- [40] Armstrong RD, Henderson M. Impedance plane display of a reaction with an adsorbed intermediate. *J Electroanal Chem* 1972. [https://doi.org/10.1016/S0022-0728\(72\)80477-7](https://doi.org/10.1016/S0022-0728(72)80477-7).
- [41] Castro EB, Gervasi CA, Vilche JR. Oxygen evolution on electrodeposited cobalt oxides. *J Appl Electrochem* 1998. <https://doi.org/10.1023/A:1003488409147>.
- [42] Conway BE, Liu TC. Characterization of Electrocatalysis in the Oxygen Evolution Reaction at Platinum by Evaluation of Behavior of Surface Intermediate States at the Oxide Film. *Langmuir* 1990. <https://doi.org/10.1021/la00091a044>.
- [43] Krstajić N, Popović M, Grgur B, Vojnović M, Šepa D. On the kinetics of the hydrogen evolution reaction on nickel in alkaline solution - Part I. The mechanism. *J Electroanal Chem* 2001. [https://doi.org/10.1016/S0022-0728\(01\)00590-3](https://doi.org/10.1016/S0022-0728(01)00590-3).
- [44] Lyons MEG, Brandon MP, *Int. J. Electrochem. Sci.*, 2008, 3, 1425-1462.
- [45] Wu G, Li N, Zhou DR, Mitsuo K, Xu BQ. Anodically electrodeposited Co+Ni mixed oxide electrode: Preparation and electrocatalytic activity for oxygen evolution in alkaline media. *J Solid State Chem* 2004. <https://doi.org/10.1016/j.jssc.2004.06.027>.
- [46] Bott, A. W. *Electrochemistry of Semiconductors*. *Curr. Sep.* 1998, 17, 3.
- [47] Beranek R. (Photo)electrochemical methods for the determination of the band edge positions of TiO₂-based nanomaterials. *Adv Phys Chem* 2011. <https://doi.org/10.1155/2011/786759>.
- [48] Fabregat-Santiago F, Garcia-Belmonte G, Bisquert J, Bogdanoff P, Zaban A. Mott-Schottky Analysis of Nanoporous Semiconductor Electrodes in Dielectric State Deposited on SnO₂(F) Conducting Substrates. *J Electrochem Soc* 2003. <https://doi.org/10.1149/1.1568741>.

- [49] Hankin A, Bedoya-Lora FE, Alexander JC, Regoutz A, Kelsall GH. Flat band potential determination: Avoiding the pitfalls. *J Mater Chem A* 2019. <https://doi.org/10.1039/c9ta09569a>.
- [50] Memming R. *Semiconductor Electrochemistry*. 2000. <https://doi.org/10.1002/9783527613069>.
- [51] Scholz F. *Electroanalytical methods: Guide to experiments and applications*. 2010. <https://doi.org/10.1007/978-3-642-02915-8>.
- [52] Hall DS, Lockwood DJ, Bock C, MacDougall BR. Nickel hydroxides and related materials: A review of their structures, synthesis and properties. *Proc R Soc A Math Phys Eng Sci* 2015. <https://doi.org/10.1098/rspa.2014.0792>.
- [53] Ash B, Nalajala VS, Popuri AK, Subbaiah T, Minakshi M. Perspectives on nickel hydroxide electrodes suitable for rechargeable batteries: Electrolytic vs. chemical synthesis routes. *Nanomaterials* 2020. <https://doi.org/10.3390/nano10091878>.
- [54] Xu P, Milstein TJ, Mallouk TE. Flat-Band Potentials of Molecularly Thin Metal Oxide Nanosheets. *ACS Appl Mater Interfaces* 2016. <https://doi.org/10.1021/acsami.6b02901>.
- [55] Gelderman K, Lee L, Donne SW. Flat-band potential of a semiconductor: Using the Mott-Schottky equation. *J Chem Educ* 2007. <https://doi.org/10.1021/ed084p685>.
- [56] Darowicki K, Krakowiak S, Ślepski P. Selection of measurement frequency in Mott-Schottky analysis of passive layer on nickel. *Electrochim. Acta*, 2006. <https://doi.org/10.1016/j.electacta.2005.04.079>.
- [57] Florent M, Wallace R, Bandosz TJ. Oxygen Electroreduction on Nanoporous Carbons: Textural Features vs Nitrogen and Boron Catalytic Centers. *ChemCatChem* 2019. <https://doi.org/10.1002/cctc.201801675>.
- [58] Blasco-Ahicart M, Soriano-Lopez J, Carbo JJ, Poblet JM, Galan-Mascaros JR. Polyoxometalate electrocatalysts based on earthabundant

metals for efficient water oxidation in acidic media. *Nat Chem* 2018. <https://doi.org/10.1038/NCHEM.2874>.

[59] Lu G, Yang H, Zhu Y, Huggins T, Ren ZJ, Liu Z, et al. Synthesis of a conjugated porous Co(ii) porphyrinylene-ethynylene framework through alkyne metathesis and its catalytic activity study. *J Mater Chem A* 2015. <https://doi.org/10.1039/c4ta06231k>.

[60] Battiato S, Urso M, Cosentino S, Pellegrino AL, Mirabella S, Terrasi A. Optimization of oxygen evolution reaction with electroless deposited Ni–P catalytic nanocoating. *Nanomaterials* 2021. <https://doi.org/10.3390/nano11113010>.

[61] Bian Y, Wang H, Gao Z, Hu J, Liu D, Dai L. A facile approach to high-performance trifunctional electrocatalysts by substrate-enhanced electroless deposition of Pt/NiO/Ni on carbon nanotubes. *Nanoscale* 2020. <https://doi.org/10.1039/d0nr03378b>.

[62] Gong M, Zhou W, Tsai MC, Zhou J, Guan M, Lin MC, et al. Nanoscale nickel oxide/nickel heterostructures for active hydrogen evolution electrocatalysis. *Nat Commun* 2014. <https://doi.org/10.1038/ncomms5695>.

Chapter 5

Enlightening the Bimetallic Effect of Au@Pd Nanoparticles on Ni Oxide Nanostructures

Content

Bimetallic nanoparticle decoration	121
Methods	123
Colloidal Au, Pd, and Au@Pd dispersion	123
Decorate Ni oxide electrode (NOE)	123
Analytical Techniques	123
Morphological and elemental characterization	125
Electrochemical modification and characterization	126
Modeling the bimetallic decoration effect	130
Glucose and H₂O₂ sensing test	136
Conclusions	139
References	140

Summary

In this chapter, we experimentally investigate the decoration of a Ni oxide nanostructure with NPs of Au, Pd and Au@Pd (Au core, Pd shell). Bimetallic decoration of semiconductor electrodes typically improves catalytic and sensing performances because of a well-claimed synergistic effect. Electrochemical measurements quantitatively elucidate the effect of decoration with mono or bimetallic nanoparticles. Decorated electrodes show higher redox currents than bare ones and a shift in redox peaks, which can be ascribed to a more efficient electron transport and improved catalytic properties. These effects are satisfactorily modeled employing a nano Schottky junction at the nanoparticle-semiconductor interface, pointing out large energy band bending, space charge region and local electric field in bimetallic decoration. Sensing test of glucose and H₂O₂ by decorated Ni oxide electrodes are performed to consolidate our model. The presence of bimetallic nanoparticles enhances enormously the electrochemical performances of the material in terms of sensitivity, catalytic activity, and electrical transport. The modification of energy band diagram in semiconductor is analyzed and discussed also in terms of electron transfer during redox reactions.

4.1 Bimetallic nanoparticle decoration

Bimetallic nanoparticles (NPs) have attracted enormous interest in the past decade due to their intriguing physical and chemical properties, and their applications in many fields of materials science (catalysis, photocatalysis, optics, sensing, and nanomedicines) [1-5]. Indeed, the addition/substitution of one or more chemical elements to a metallic surface increases the possible bonding geometries of surface adsorbates and simultaneously changes the electronic structure at surface [6]. Generally, bimetallic NPs can be classified according to their mixing pattern (chemical ordering) and geometric structure. Two main categories of NPs can be identified: core-shell (or core@shell) and nanocomposite bimetallic NPs (Figure 4.1), with an ordered atomic arrangement in the first case and random mixed atoms in the second one [2]. Independently of the ordering, a certain improvement of catalytic and sensing performance is observed and typically explained inferring a *synergistic* effect [7]. In fact, most fundamental properties of NPs cannot be described as extrapolation of bulk properties. From the theoretical perspective, bimetallic NPs provide ideal test bench for the development of novel theoretical concepts and techniques and present a series of questions of fundamental interest [8].

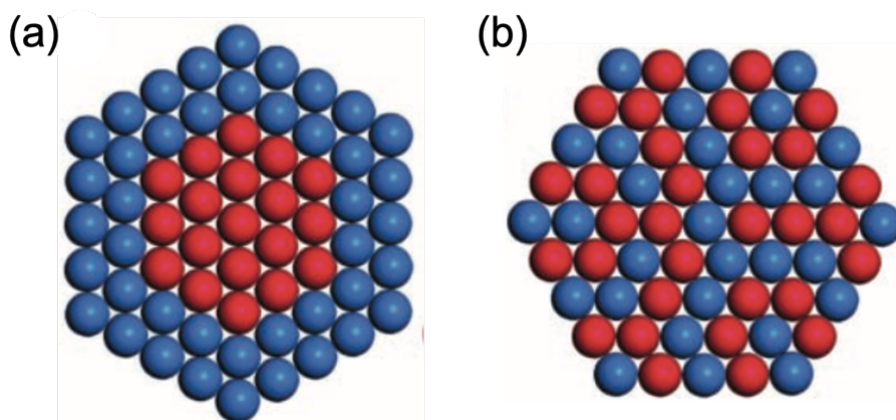


Figure 4.1: Bimetallic nanoparticles with different configurations: (a) core-shell and (b) alloy [adapted from 1].

Several theoretical investigations studied this synergistic effect on surface adsorption and chemical reactions [9-14]. When a foreign metal atom is added to a metal host, a key change occurs in d -band position and filling, caused by local bonding alteration to accommodate the foreign atom. The number of d -electrons is typically affected by these changes, and its variation leads to a change in reactivity of bimetallic nanoparticles [15]. Figure 4.2 show the effect of different nanoparticles on the electronic band structure of the catalyst. From the experimental point of view, the effect of bimetallic NPs induces a sensible boost in terms of sensitivity [16,17], catalytic activity [11,14,18], and electrical properties [19,20]. However, most experimental papers, beyond measuring the bimetallic effect and invoking an unspecified synergistic effect, miss any attempt to microscopic characterize and model it [21]. A deep understanding of the relationship between catalytic outcome and synergistic effect in bimetallic NPs could help in developing more efficient sensors with low cost, enhanced activity, and high selectivity [21].

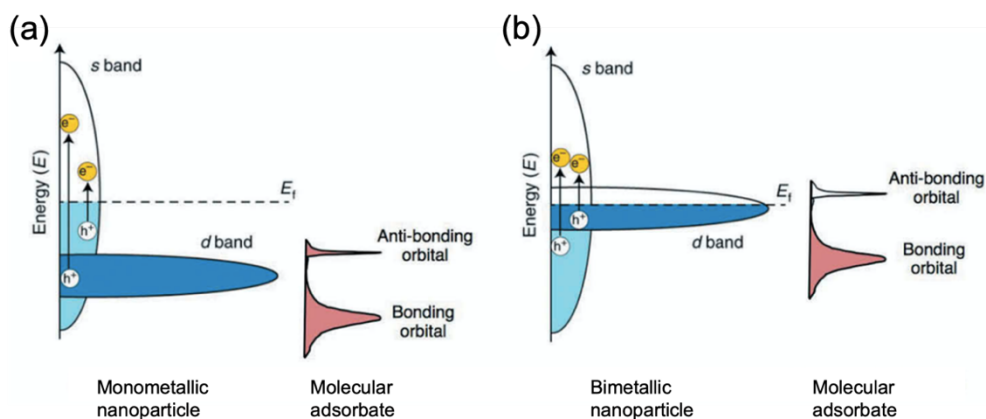


Figure 4.1: Electronic band structure of typical (a) monometallic and (b) bimetallic nanoparticles. To the right of each diagram is the density of states of a simple molecular adsorbate [Adapted from 4].

Among the different applications of bimetallic NP, electrochemical sensors are largely involved to exploit the synergistic effect thanks to their simplicity, low-cost fabrication, and ease to be minimized, leading to higher sensitivity and selectivity [22-30]. In particular, core-shell bimetallic Au@Pd NPs are observed to have superior synergistic effects [11-14,26,31]. In most cases, the effect of decoration with bimetallic NPs is evaluated on flat or bulk substrates [12,26,32-34]. The enhanced

electrocatalytic activity and electrochemical stability of bimetallic NPs were exploited for electrochemical enzyme-free sensing achieving high sensitivity and selectivity [12,34-35]. The presence of NPs on nanostructured substrates can link the advantages of nanostructures (large surface area and/or quantum size effect) with the specificity of synergistic effects.

4.2 Methods

4.2.1 Colloidal Au, Pd, and Au@Pd dispersion

Dispersions containing Au or Pd or Au@Pd NPs following the procedure in Chapter 2 [37-40].

4.2.2 Decorated Ni oxide electrode (NOE)

Fluorine-doped Tin Oxide (FTO) substrates (1x2 cm², resistivity ~ 13 Ω/sq, Sigma-Aldrich, St. Louis, MO, USA) were used as substrate for Ni nanofoam (NF) synthesis (details in Appendix B) [41,42]. The metallic Ni nanostructure is then decorated via spin coating (500 rpm, 60 s) by using 50 μL of the mono or bimetallic NPs dispersion as prepared. The samples are dried on a hot plate at 80 °C for 10 minutes. Finally, the Ni oxide electrode (NOE) were obtained by several cycles of cyclic voltammetry (CV, in 0.1 M NaOH, scan rate of 0.05 V s⁻¹) between -0.3 V and 0.9 V vs SCE, leading to surface oxidation of Ni [43]. Decorated samples are labelled according to NP type onto NOE (e.g., Au-NOE refers to NOE decorated with Au NPs).

4.2.3 Analytical techniques

UV-vis spectroscopy was performed on Au solution using a Varian Cary 500 (Agilent technologies, California, USA) double beam scanning UV/VIS/NIR spectrophotometer.

The elemental composition of NPs in the dispersions was evaluated on a Si wafer coated with NPs (via spin coating) by Rutherford backscattering spectrometry (RBS, 2.0 MeV He⁺ beam at normal incidence) with a 165° backscattering angle by using a 3.5 MV HVEE Singletron accelerator system (High Voltage Engineering Europa, Netherlands). RBS spectra were analyzed by using XRump software [44].

Surface morphology was analyzed by using a Scanning Electron Microscope (SEM, Gemini field emission SEM Carl Zeiss SUPRA 25, FEG-SEM, Carl Zeiss Microscopy GmbH, Jena, Germany).

Transmission electron microscopy (TEM) analyses of Au, Pd and Au@Pd NPs dispersed on a TEM grid were performed with a Cs-probe-corrected JEOL JEM ARM200F microscope at a primary beam energy of 200 keV operated in scanning TEM (STEM) mode and equipped with a 100 mm² silicon drift detector for energy dispersive X-ray (EDX) spectroscopy. For EDX elemental mapping, the Au M and Pd L X-rays signals were collected by scanning the same region multiple times with a dwell time of 1 ms. TEM images and EDX spectra were analyzed by using DigitalMicrograph® software [45].

Electrochemical measurements were carried out at room temperature by using a VersaSTAT 4 potentiostat (Princeton Applied Research, USA) and a three-electrode setup with a platinum counter electrode, a saturated calomel electrode (SCE) as reference electrode, and our samples as working electrode, without purging any inert gas. 0.1 M NaOH (Sigma Aldrich, St. Louis, MO, USA) was used as supporting electrolyte. Cyclic voltammetry (CV) curves were recorded at a scan rate of 50 mV s⁻¹ in the potential range -0.3 ÷ 1.0 V vs SCE. Electrochemical impedance spectroscopy (EIS) was performed at the oxidation peak potential with a superimposed 5 mV sinusoidal voltage in the frequency range 10⁴ ÷ 10⁻¹ Hz. Mott-Schottky (M-S) analyses were conducted on bare and decorated NOE samples in the potential range -0.5 ÷ 1 V vs SCE, at 1000 Hz frequency. Chronoamperometry (CA) analysis was employed to study the response of the samples to successive additions of different amounts of glucose (D-(+)-glucose, Sigma-Aldrich, St. Louis, MO, USA) and H₂O₂ (30 w/w% H₂O₂ in H₂O, Sigma-Aldrich, St. Louis, MO, USA) to the 0.1 M NaOH solution.

A simulation of semiconductor energy bands, electron concentration, and electric field at the metal/semiconductor interface has been carried out by *COMSOL Multiphysics® software* [46].

4.3 Morphological and elemental characterization

Figure 4.3(a) shows the synthesis and decoration procedure of Ni-based electrodes by a three-step method:

1. Chemical Bath deposition ($\text{Ni}(\text{OH})_2$ nanowalls);
2. Thermal Annealing (Ni nanofoam)
3. Nanoparticle Decoration.

SEM images of Ni NF and Au@Pd decorated Ni NF are reported in Figure 4.3(b-c), revealing an open porous structure made of chain-like clusters of metallic Ni NPs (20 nm large) with some bigger bimetallic nanoparticles randomly distributed on the surface of the nanostructure.

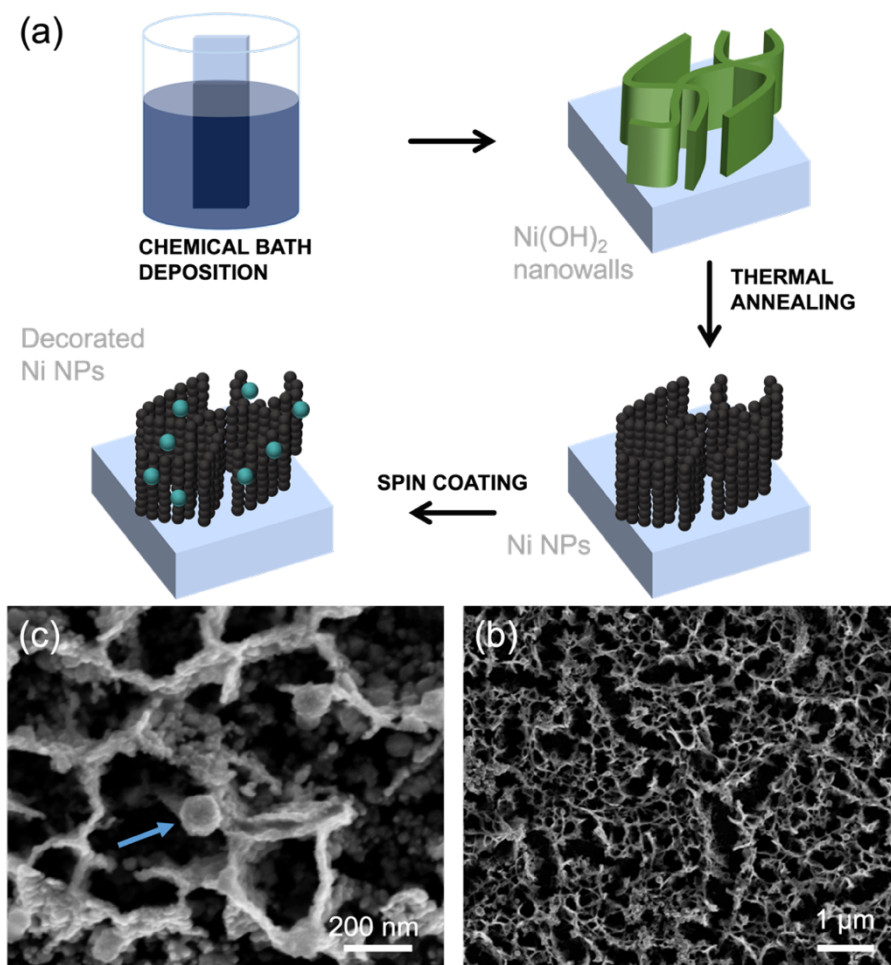


Figure 4.3: (a) Schematic representation of synthesis and decoration of Ni NPs; (b) SEM image of porous Ni NPs; (c) High magnification SEM image of Au@Pd NPs anchored on the top of Ni NPs (blue arrow).

4.4 Electrochemical modification and characterization

The bare or decorated metallic Ni NPs were then modified by electrochemical methods in order to form a thin layer of Ni oxide/hydroxide through several cycles of cyclic voltammetry (CV, in 0.1 M NaOH, scan rate of 0.05 V s^{-1}) between -0.3 V and 0.9 V vs SCE (Figure 4.4(a)) [43,49]. The surface oxidation of Ni is the last step to produce Ni oxide electrodes (NOE) consisting of a metallic Ni skeleton covered by a thin semiconductor Ni oxide/hydroxide, possibly decorated with mono- or bimetallic NPs.

Figure 4.4(b) displays the cyclic voltammograms of bare electrode compared to that decorated with Au, Pd, and Au@Pd NPs. CV curves were recorded in 0.1 M NaOH at a scan rate of 0.05 V s^{-1} between -0.3 V and 0.9 V vs SCE, for several cycles, until stable voltammograms are obtained. This leads to the oxidation of surface Ni into a $\sim 3 - 4 \text{ nm}$ NiOOH/Ni(OH)₂ shell uniformly recovering Ni NPs [43,49]. Actually, the CV curves always show a pair of redox peaks around $V = 0.6 \div 0.75 \text{ V}$ vs SCE (oxidation peak) and $V = -0.05 \div 0.15 \text{ V}$ vs SCE (reduction peak), caused by the reversible transition $\text{Ni}^{2+}/\text{Ni}^{3+}$ in alkaline medium [41,50,51]:

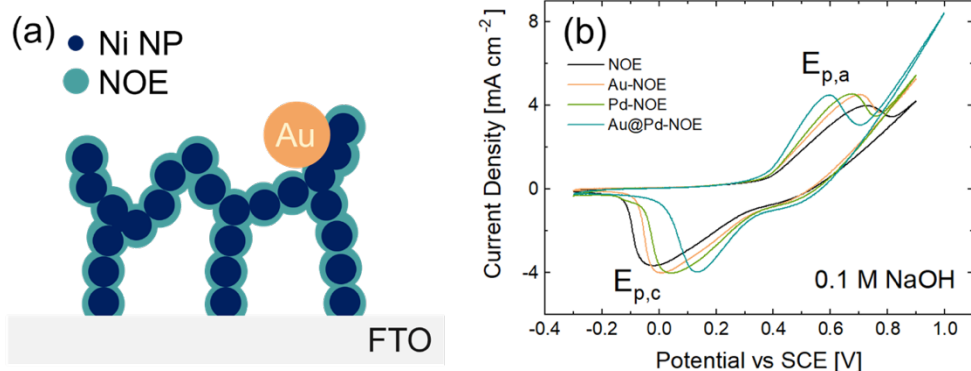
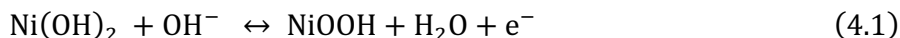


Figure 4.4: (a) Scheme of a cross section of decorated NOE; (b) cyclic voltammograms of bare and decorated electrodes.

From a microscopic point of view, the liquid/solid interface tested by electrochemical analysis is composed of used electrolyte (0.1 M NaOH) and NiOOH/Ni(OH)₂ semiconductor decorated with mono- or bimetallic NPs. The effect of decoration on the redox behavior of Ni electrode will be obtained by comparing the bare semiconductor with decorated one. Compared to bare electrode, the decorated ones present higher peak currents both in oxidation and reduction. In addition, the gap between anodic ($E_{p,a}$) and cathodic ($E_{p,c}$) peak potentials ($\Delta E_p = E_{p,a} - E_{p,c}$) decreases in decorated electrodes, especially in bimetallic case. At the same time, the full width at half maximum (FWHM, calculated by subtracting the background signal to the peak one) of both anode and cathode peaks is also reduced following decoration, especially with bimetallic NPs (Figure 4.5 shows the redox peaks after background subtraction) [52-54].

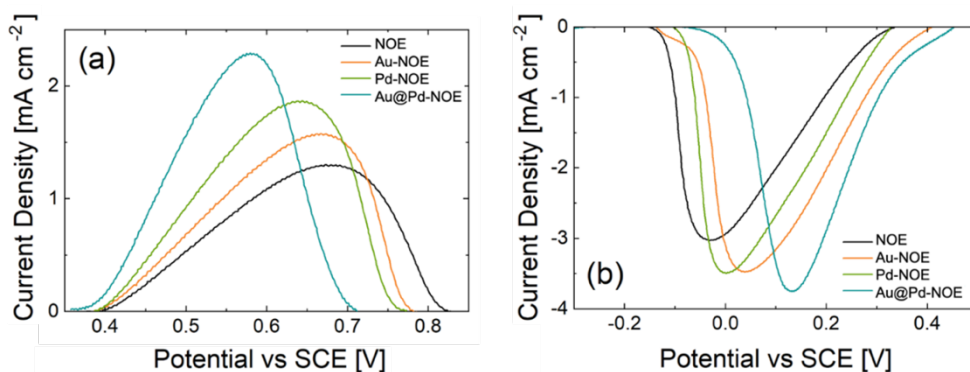


Figure 4.5: (a) anodic and (b) cathodic peaks for bare and decorated electrode after the subtraction of the baseline.

To ensure that the presence of NPs affects predominantly the NOE and not the FTO substrate, CVs on Au, Pd, and Au@Pd NP decorated FTO were performed. As shown in Figure 4.6(a), neither mono- nor bi-metallic NPs influences the electrochemical performances of ITO since CV curves do not present any difference between each other. This is a clear indication of how NPs decoration is effective in the modification of redox behavior of NOE. It is important to note that, although CV cycling creates a Ni oxide/hydroxide shell at the metal Ni NPs surface, it does not modify the morphology of the nanostructures (a SEM image of NOE after electrochemical measurements is shown in Figure 4.6(b)).

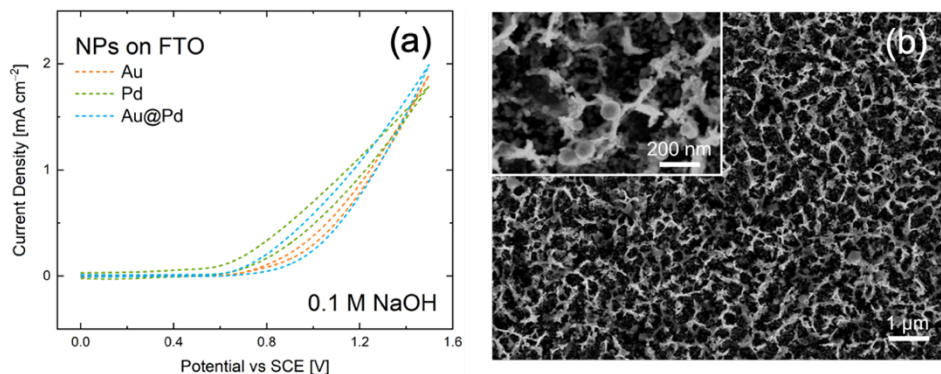


Figure 4.6: (a) Cyclic voltammograms of Au, Pd and Au@Pd NPs on FTO; (b) SEM image of NOE after electrochemical characterization (Au@Pd NP anchored to NOE in the inset).

EIS was employed to study the interfacial properties of electrodes. Figure 4.7(a) exhibits the real and imaginary part of impedance (Nyquist plot) of bare and modified electrodes, together with fitting lines assuming a simple Randles circuit (inset) [55]. The decoration induces a dramatic change in semicircular shape of Nyquist plot, reducing the circle diameter (representing the Charge Transfer Resistance (R_{ct}) from 12.5Ω (bare NF) to $10 - 11 \Omega$ (Au or Pd-Ni NF), to 5.5Ω (Au@Pd-NF). Fit parameters are reported in Table 4.1. The decreased peak potentials give an indication of an enhanced capability of bimetallic system to catalyze the electrocatalytic reactions [23,54]. These results prove that decoration accelerates the electron transfer kinetics, especially in the bimetallic case [22,23,56-60], and well explain the reduction of ΔE_p in the CV curves.

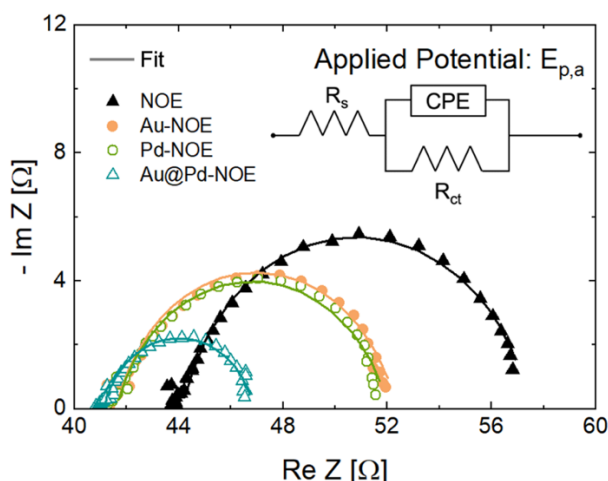


Figure 4.7: EIS spectra of bare and decorated NOE (Randle circuit in the inset).

Sample	R_S [Ω]	R_{ct} [Ω]	CPE [mF s^{n-1}]	n
NOE	43.7 ± 0.3	12.5 ± 0.7	1.1 ± 0.3	0.53
Au-NOE	41.3 ± 0.2	10.6 ± 0.5	0.7 ± 0.2	0.64
Pd-NOE	41.2 ± 0.3	10.4 ± 0.6	0.5 ± 0.7	0.65
Au@Pd-NOE	40.9 ± 0.3	5.6 ± 0.6	0.2 ± 0.4	0.62

Table 4.1: Circuit parameters calculated from EIS spectra fitting.

To further investigate the mono- and bimetallic decoration on our nanostructured electrode, we performed Mott-Schottky (M-S) analysis (details in Appendix A). The M-S plot typically reports the inverse of squared capacitance (C^{-2}) measured as a function of potential (E) applied to the sample, as reported in Figure 4.8. By increasing E , C^{-2} goes to zero, indicating a larger and larger capacitance at the solid-electrolyte interface. Such behavior is typical of a p -type semiconductor, as the $\text{Ni}(\text{OH})_2$ is [61,62]. The so-called flat band potential, the intercept with x -axis (E_{FB}) [63-69], tells the potential where saturation of C occurs (Table 4.2). In a planar semiconductor electrode, after proper correction with open circuit potential (E_{OC}), $\Delta E_{M-S} = E_{FB} - E_{OC}$ represents the energy band bending at equilibrium (flat Fermi energy, electrode to electrolyte) [70]. The energy band bending results from the alignment of the Fermi level of bare or modified semiconductor surface and the redox potential of electrolyte [71]. With decoration, there is a clear shift of E_{FB} towards more positive potential, up to 0.4 V in bimetallic case (Table 4.2). Even if our electrodes are not planar but nanostructured semiconductor, such evidence points out a key difference in energy band bending due to mono- and bimetallic decoration. A larger value of E_{FB} points out that a more positive potential is needed to saturate the capacitance. This datum helps the modeling of bimetallic effects, as follows.

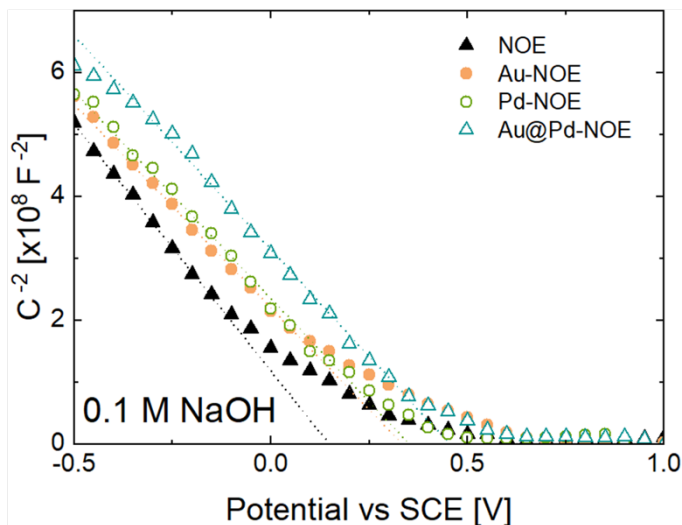


Figure 4.8: Mott-Schottky plot of bare and decorated NOE.

Sample	E_{FB} [V vs SCE]	E_{OC} [V vs SCE]	ΔE_{M-S} [V]
NOE	0.150	0.065	0.085
Au-NOE	0.335	0.052	0.283
Pd-NOE	0.352	0.059	0.293
Au@Pd-NOE	0.455	0.047	0.408

Table 4.2: Values of flat band potential, open circuit potential and energy barrier for bare and decorated samples.

4.5 Modeling the bimetallic decoration effect

Qualitative and quantitative information can be extracted from electrochemical analytical data.

The expression of the peak current I_p in a typical CV strongly depends on the reaction mechanism [71-73]. In particular, for a generic reaction:

$$I_p \propto AD^{1/2}c_0v^{1/2} \quad (4.2)$$

where A is the area of the electrode (cm^2), D is the diffusion coefficient (cm^2/s), c_0 is the reagent concentration (mol/cm^3), and v is the scan rate (V/s).

The quantity that most influences the reaction mechanism is the diffusion coefficient. Higher peak current corresponds to a higher diffusion coefficient and, consequently, to an improved electron transfer at the solid-liquid interface.

Referring to the electron transfer theories developed by Marcus, Hush and Gerischer [74-81], it is possible to describe electrochemical kinetics in terms of thermodynamic quantities and energy levels. The position of a voltammetric peak is related to the electrochemical potential provided, therefore it carries information on both the thermodynamics and the kinetics of the process [71-73]. By applying an electrical potential, the activation energy (ΔG^\ddagger) necessary to obtain an oxidation (or reduction) of the electrode is provided. The total free energy of the system can be seen as the sum of a thermodynamic term (ΔG_{TD}) and an activation one:

$$\Delta G = \Delta G^0 + \Delta G^\ddagger \quad (4.3)$$

ΔG^0 determines the position of the reversible potential, corresponding to the process without activation barriers for charge transfer, according to Nernst's law:

$$\Delta G^0 = -nF(E - E_{redox}) \quad (4.4)$$

where n is the number of electrons involved in the reaction, F is the Faraday's constant, E is the electrode potential, and E_{redox} is the standard redox potential. On the other hand, ΔG^\ddagger corresponds to that additional term (overpotential) that must be provided to start the reaction and corresponds to the activation barriers of the process [71,73]. As the activation barrier increases, the electrochemical irreversibility of the system increases and an overpotential is required for the reaction to take place. Due to this additional potential, the CV signals move to more extreme potentials (therefore to higher energies). The oxidation potential will shift to the right, while the reduction potential will shift to the left. At the same time, peaks broaden and lower [73].

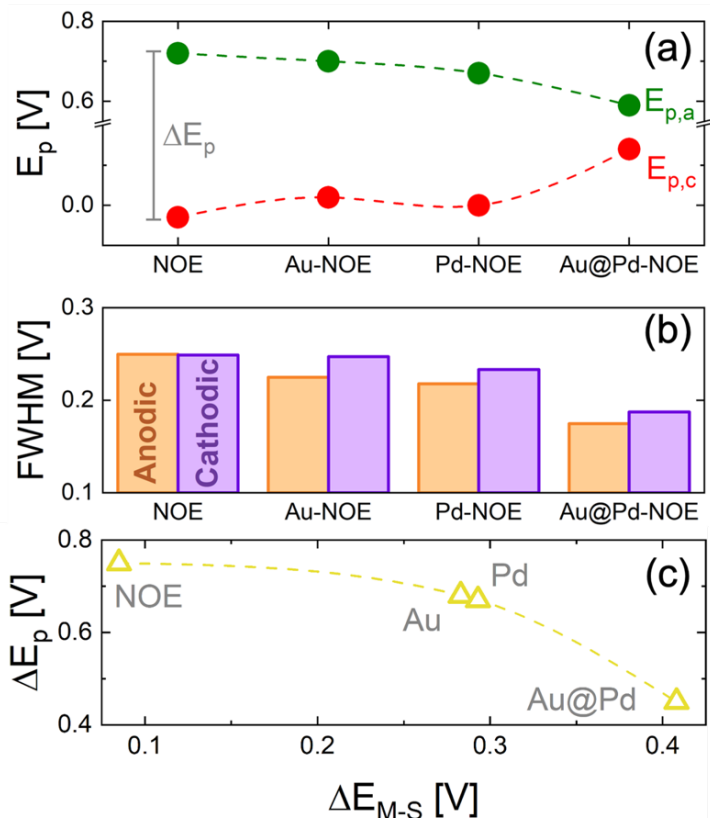


Figure 4.9: Variation of (a) $E_{p,a}$ and $E_{p,c}$ as a function of metal NP decoration (the peak separation between the two peaks positions is labelled as ΔE_p), (b) FWHM of the anodic and cathodic peaks; (c) relation between ΔE_p and ΔE_{M-S} .

The potential of oxidation ($E_{p,a}$) and reduction ($E_{p,c}$) peaks are reported in Figure 4.9(a) for each sample. The position of a voltammetric peak carries information on both thermodynamics and kinetics of the electrochemical process taking place (Eq. (4.1) in our case) [71-73]. The activation energy for electrode oxidation (or reduction) is provided by applying the electrical potential to the electrode. It should be noted that in our NOE the metallic skeleton provides an effective bias of the catalytic surface, reducing any potential drop, in a fashion similar to what previously modelled [43]. As the activation barrier increases, the electrochemical irreversibility of the system increases and an overpotential is required for the reaction to take place, shifting the oxidation (reduction) peak to higher (lower) electrical potential. Figure 4.9(a) represents the catalytic action of NP decoration, by reducing the activation barrier for Eq. (4.1).

It is noteworthy the bimetallic effect which overcomes that of monometallic decoration, strongly reducing the ΔE_p . Figure 4.9(b) reports the FWHM for all the peaks, evidencing a clear shrinking trend with decoration. A catalytic reduction of activation energy results also in a reduction of FWHM, and of both anodic and cathodic peaks, making more and more favorable the electron transfer at solid-electrolyte interface.

Figure 4.9(c) clarifies the relation among the ΔE_p and ΔE_{M-S} , as obtained from Figure 4.8. As the energy band bending grows (in bimetallic decorated sample), the energy separation among oxidation and reduction peaks decreases, index of a strong catalytic effect compared to bare sample. The mono- or bimetallic decoration increases the energy band bending, because of electron spillover effects, leading to space charge regions and a potentially very high, localized electric field [19,40].

To compute and visualize such energy band bending at the interface between NPs and $\text{Ni}(\text{OH})_2$, COMSOL [46] simulations were performed assuming a single metal circular dot (20 nm large) placed onto the semiconductor (Figure 4.10(a)) and simulating a nano Schottky junction [18,40,70]. The simulation does not consider surface defects or temperature dependence and takes into account the experimentally extracted Mott-Schottky band bending (Table 4.2).

Actually, the M-S measurement returns an average behavior of samples and not a local quantification of energy band bending at the decoration site. Despite these limits, the simulation helps to understand the catalytic effect of mono- and bimetallic decoration.

The *p*-type semiconductor is greatly enriched in electrons (spillover effect) below the metallic dot (Figure 4.10(b)), which means a downward bending of its energy bands. The energy map of the conduction band minimum (CBM) for Au@Pd decorated sample as a function of depth and distance from NP center is reported in Figure 4.10(c). The downward bending of CBM extends almost 5 nm within semiconductor, denoting a giant electric field under the NP, pointing towards the bulk. Considering our case in which the Ni oxide is confined in a thin shell (3-4 nm) on a metal core in our NOE, it is reasonable to hypothesize that the whole nanostructure is depleted of electrons (pushed towards the surface by a giant built-in electric field).

The 2D map of electric field at decoration site is shown in Figure 4.10(d) for the bimetallic case, revealing intensity up to 10^8 V m^{-1} . A peculiar “halo effect” comes because of the largest potential gradient at the NP edge⁴⁰. A comparison of band bending and electron concentration at decoration site

between Au and Au@Pd decoration is presented in Figure 4.10(b) and Figure 4.10(e). The bimetallic decoration induces a 10 times higher electron concentration in comparison to Au NP decoration, pointing out how the synergistic effect among Au and Pd in core-shell nanostructures can boost a catalytic action of modified electrodes.

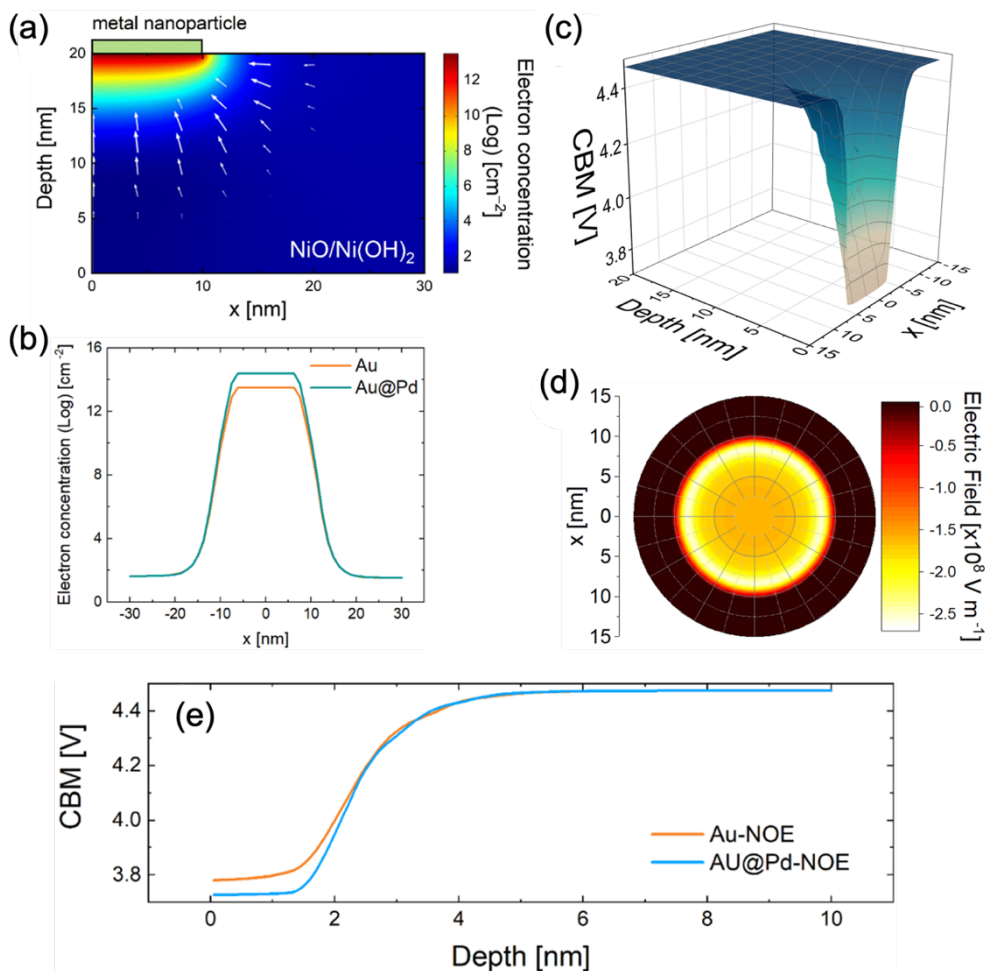


Figure 4.4: (a) 2D COMSOL simulation of the electron concentration at Au@Pd-NOE interface; (b) electron concentration profile at metal-semiconductor interface; COMSOL simulations of (c) conduction band minimum (CBM) of Au@Pd-NOE sample, and (d) electric field map under a circular Au@Pd dot; (e) conduction band minimum (CBM) profile for Au and Au@Pd decorated samples.

Figure 4.11 contains a schematic representation of our model of bimetallic effect by exploiting the energy band bending at the decoration site as a consequence of the formation of a nano Schottky junction. Compared to bare electrode (Figure 4.11(a)), the presence of mono- and bimetallic NPs (Figure 4.11(b-c)) induces a larger ΔE_{M-S} which points out a larger energy band bending of semiconductor. The gradient of energy band represents the intensity of localized electric field, which comes from a space charge region. In turns, mono- and bimetallic NP decoration leads to accumulation of immobile positive charges at the solid-electrolyte interface, with greatest extent in case of bimetallic case. In this scenario, the large electric field at decoration site should lead to a net local charge imbalance, with electron accumulation in the Ni oxide at electrode side, and OH^- ions buildup at electrolyte side. The increased concentration of OH^- ions close to the electrode surface makes more favorable the conversion of $\text{Ni}(\text{OH})_2$ to NiOOH (Eq. (4.1)) during the anodic scan of the potential. The accumulation of electrons, on the other side, facilitates the electrode reduction during the cathodic scan. In bimetallic NP decoration, such catalytic actions are enhanced probably because of the different d -band filling in Au@Pd core@shell NP [11,15].

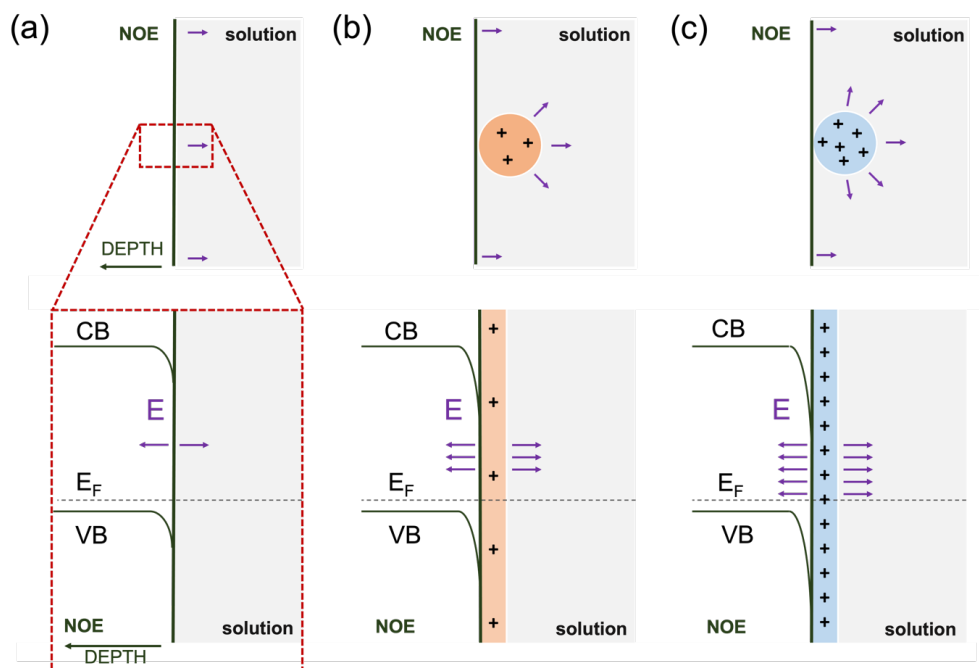


Figure 4.11: Scheme of energy band bending and local electric field E for (a) bare, (b) Au (or Pd), and (c) Au@Pd decorated electrode at solid-liquid interface.

4.6 Glucose and H₂O₂ sensing test

To validate our model, sensing tests in both oxidant and reducing conditions were conducted, detecting glucose and H₂O₂, respectively. The amperometric responses of NOE, Au-NOE, Pd-NOE, and Au@Pd-NOE samples were recorded by successive additions of glucose or H₂O₂ to electrochemical cell containing 50 mL NaOH (0.1M). Figure B7 displays typical current-time plot of electrodes with continuous addition of glucose or H₂O₂. Steady-state currents were typically obtained 2-3 s after addition.

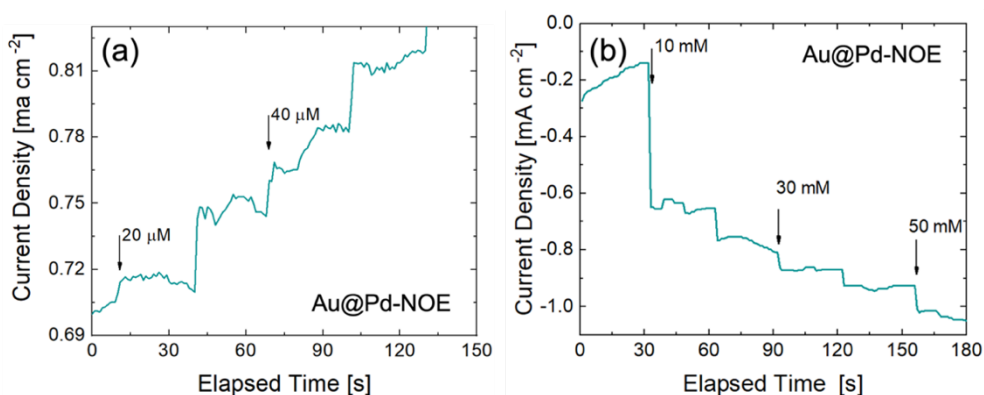


Figure 4.12: Chronoamperometric curves of Au@Pd-NOE sample after subsequent additions of (a) glucose and (b) H₂O₂.

Concerning glucose test, the fabricated samples show a sensitivity of 2.41, 2.75, 2.52, 2.90 mA cm⁻²mM⁻¹ for NOE, Au-NOE, Pd-NOE, and Au@Pd-NOE, respectively. The same electrode, for H₂O₂ test, gave sensitivities of 23.6, 130.9, 127.4, 340 μA cm⁻²mM⁻¹. Figure 4.13 summarizes the obtained sensitivities of electrodes, while a large comparison with similar sensors in literature is given in Table 4.3. No significant changes in sensitivity can be appreciated in glucose test, while for H₂O₂ detection, bimetallic NPs catalyze H₂O₂ reduction with a sensitivity approximately one order of magnitude higher than bare NOE and almost three times higher than samples decorated with monometallic NPs. These results consolidate our model of energy band bending induced by decoration. Bare NOE (NiO and Ni(OH)₂) is made of *p*-type semiconductor [61,62], while decorated NOE shows electron reservoirs localized at decoration sites.

During glucose oxidation, electrons are transferred from solution to electrode and thus no appreciable effects is observed after decoration. The downward band bending, as a result of the creation of an electric field directed to the bulk of the semiconductor, leads to the transfer of electrons to the solution. During the glucose oxidation, however, the electrons have to pass from the solution to the samples in order to oxidate the analyte. For this reason, no appreciable effect from the oxidation of glucose was appreciated and none boost in sensitivity from the decoration with bimetallic nanoparticles was observed. On the other hand, during H_2O_2 reduction, availability of electrons at surface of NOE boosts the sensitivity of decorated electrodes in comparison to bare one. The different orders of magnitude of the sensitivity between the oxidation of glucose and the reduction of H_2O_2 can be easily explained by considering that only in those regions close to NPs (i.e. at the nano Schottky junctions) the electric field induces a modification of energy bands and an accumulation of electrons. As a consequence, only small percentage of surface (with a higher concentration of available electrons) are active in H_2O_2 reduction, while for glucose the whole material is responsible for the oxidation reaction. Moreover, the synergism between Au and Pd, with higher electric field and electron concentration, induces an extra boost in sensitivity and better electrochemical performances than the monometallic counterpart.

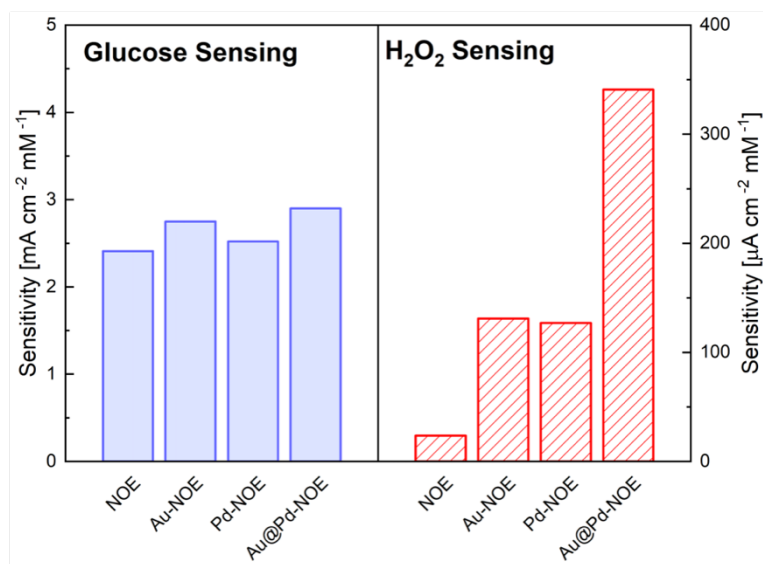


Figure 4.13: Sensitivity of NOE, Au-NOE, Pd-NOE, and Au@Pd-NOE for glucose and H_2O_2 test.

GLUCOSE			
Electrode	Sensitivity [$\mu\text{A cm}^{-2} \text{mM}^{-1}$]	LOD [μM]	Ref.
Au-CuO - GCE	3126.76	1.4	16
Ag@Cu	20.9	3.5	22
Au@Ni/C	23.17	15.7	29
PtPd - MWCNTs	112	31	53
Au-Ni	30.58	25	59
CuO/NiO - Carbon	856.7	0.037	82
PtPb - MWCNTs	17.8	1.8	83
CuOx/NiOy	2043	0.08	84
Au-C	101.2	3	85
NiCoP	6115	0.36	86
NOE	2410	6	Our Work
Au-NOE	2750	5	Our Work
Pd-NOE	2523	7	Our Work
Au@Pd-NOE	2901	3	Our Work

H₂O₂			
Electrode	Sensitivity [$\mu\text{A cm}^{-2} \text{mM}^{-1}$]	LOD [mM]	Ref.
AuPd-NG	5095.5	0.02	17
Ag@Cu	85.1	0.3	22
Pd@Ag - RGO	1307.46	0.7	23
CoFe - NGR	435.7	0.28	24
AuPt	46.7	2.6	25
PtIr - MWCNTs	58.8	2.5	52
PtPd - MWCNTs	414.8	1.2	52
PtAu-RGO - GCE	410.5	0.008	83
CuOx/NiOy	271.1	0.09	84
Au-C	170.6	1.5	85
PtCu	60.4	12.1	87
PtNi	208.5	31.2	87
PtPd	239.8	114	87
PtRh	839.9	348	87
Au@Pt	882.2	0.1	88
Ag-Au	600	0.2	89
Ag-Au	260.08	0.18	90
NOE	23.6	6.7	Our Work
Au-NOE	130.9	1.2	Our Work
Pd-NOE	127	1.3	Our Work
Au@Pd-NOE	340.8	0.5	Our Work

Table 4.3: Comparison of analytical performance of bare and decorated Ni NF with recently reported glucose and H₂O₂ sensors.

4.7 Conclusions

Au, Pd and Au@Pd (core@shell) nanoparticles were synthesized through a low-cost method and used to decorate a Ni oxide nanostructured electrode. The effect of mono- and bimetallic decoration was carefully investigated via electron microscopy and electrochemical analytical techniques, revealing that decoration with core@shell nanoparticles allows a higher catalytic effect both on Ni redox reaction and on H₂O₂ sensing tests. The decoration effect was then modeled employing a nano Schottky junction at the nanoparticle-semiconductor interface, leading to a significant energy band bending (extending 5 nm below the decorated side) and to a giant localized electric field (up to 10⁸ V m⁻¹), causing a catalysis booster. The bimetallic nanoparticle creates a larger band bending correlated with better catalytic and sensing performances improved by more than a decade in sensitivity. An insight of electron transfer at microscopic scale close to the nanoparticle-semiconductor interface is given.

References

- [1] Loza, K., Heggen, M. & Epple, M. Synthesis, Structure, Properties, and Applications of Bimetallic Nanoparticles of Noble Metals. *Adv. Funct. Mater.* 30, 1909260 (2020) doi:10.1002/adfm.201909260.
- [2] Ferrando, R., Jellinek, J. & Johnston, R. L. Nanoalloys: From theory to applications of alloy clusters and nanoparticles. *Chem. Rev.* 108, 845-910 (2008) doi:10.1021/cr040090g.
- [3] Gilroy, K. D., Ruditskiy, A., Peng, H. C., Qin, D. & Xia, Y. Bimetallic nanocrystals: Syntheses, properties, and applications. *Chem. Rev.* 116, 10414–10472 (2016) doi:10.1021/acs.chemrev.6b00211.
- [4] Sytwu, K., Vadai, M. & Dionne, J. A. Bimetallic nanostructures: combining plasmonic and catalytic metals for photocatalysis. *Advances in Physics: X* 4, 1619480 (2019) doi:10.1080/23746149.2019.1619480.
- [5] Mandal, R., Baranwal, A., Srivastava, A. & Chandra, P. Evolving trends in bio/chemical sensor fabrication incorporating bimetallic nanoparticles. *Biosensors and Bioelectronics* 117, 546-561 (2018) doi:10.1016/j.bios.2018.06.039.
- [6] Hammer, B. & Nørskov, J. K. Theoretical surface science and catalysis—calculations and concepts. *Adv. Catal.* 45, 71-129 (2000) doi:10.1016/S0360-0564(02)45013-4.
- [7] Di Liberto, G., Pifferi, V., Lo Presti, L., Ceotto, M. & Falciola, L. Atomistic Explanation for Interlayer Charge Transfer in Metal-Semiconductor Nanocomposites: The Case of Silver and Anatase. *J. Phys. Chem. Lett.* 8, 5372-5377 (2017) doi:10.1021/acs.jpcclett.7b02555.
- [8] Fortunelli, A. & Barcaro, G. Density-Functional Theory of Free and Supported Metal Nanoclusters and Nanoalloys. in *Metal Clusters and Nanoalloys*, 29-79 (Springer, 2013). Doi:10.1007/978-1-4614-3643-0_2.
- [9] Logsdail, A. J., Paz-Bórbon, L. O. & Downing, C. A. DFT-Computed Trends in the Properties of Bimetallic Precious Metal Nanoparticles with

Core@Shell Segregation. *J. Phys. Chem. C* 122, 5721-5730 (2018) doi:10.1021/acs.jpcc.7b10614.

[10] Mamun, O., Winther, K. T., Boes, J. R. & Bligaard, T. High-throughput calculations of catalytic properties of bimetallic alloy surfaces. *Sci. Data* 6, 76 (2019) doi:10.1038/s41597-019-0080-z.

[11] Zhu, X. *et al.* Optimising surface d charge of AuPd nanoalloy catalysts for enhanced catalytic activity. *Nat. Commun.* 10, 1428 (2019) doi:10.1038/s41467-019-09421-5.

[12] Gao, F. & Goodman, D. W. Pd–Au bimetallic catalysts: Understanding alloy effects from planar models and (supported) nanoparticles. *Chem. Soc. Rev.* 41, 8009-8020 (2012) doi:10.1039/c2cs35160a.

[13] Zhang, L., Xie, Z. & Gong, J. Shape-controlled synthesis of Au-Pd bimetallic nanocrystals for catalytic applications. *Chem. Soc. Rev.* 45, 3916-3934 (2016) doi:10.1039/c5cs00958h.

[14] Silva, T. A. G., Teixeira-Neto, E., López, N. & Rossi, L. M. Volcano-like behavior of Au-Pd core-shell nanoparticles in the selective oxidation of alcohols. *Sci. Rep.* 4, 5766 (2014) doi:10.1038/srep05766.

[15] Nørskov, J. K., Studt, F., Abild-Pedersen, F. & Bligaard, T. *Fundamental Concepts in Heterogeneous Catalysis* (Wiley, 2014) doi:10.1002/9781118892114.

[16] Felix, S., Grace, A. N. & Jayavel, R. Sensitive electrochemical detection of glucose based on Au-CuO nanocomposites. *J. Phys. Chem. Solids* 122, 255-260 (2018) doi:10.1016/j.jpcs.2018.06.038.

[17] Shang, L., Zeng, B. & Zhao, F. Fabrication of novel nitrogen-doped graphene-hollow AuPd nanoparticle hybrid films for the highly efficient electrocatalytic reduction of H₂O₂. *ACS Appl. Mater. Interfaces* 7, 122-128 (2015) doi:10.1021/am507149y.

[18] Cosentino, S. *et al.* Role of AuPt_{1-x} Clusters in the Enhancement of the Electrochemical Activity of ZnO Nanorod Electrodes. *J. Phys. Chem. C* 121, 15644–15652 (2017) doi:10.1021/acs.jpcc.7b00480.

[19] Bahariqushchi, R. *et al.* Free carrier enhanced depletion in ZnO nanorods decorated with bimetallic AuPt nanoclusters. *Nanoscale* 12, 19213-19222 (2020) doi:10.1039/d0nr04134c.

[20] Wu, D. J., Xu, X. D. & Liu, X. J. Electric field enhancement in bimetallic gold and silver nanoshells. *Solid State Commun.* 148, 163-167 (2008) doi:10.1016/j.ssc.2008.07.030.

[21] Zhang, Y. W. *Bimetallic Nanostructures* (Wiley, 2018). doi:10.1002/9781119214618.

[22] Dong, S., Yang, Q., Peng, L., Fang, Y. & Huang, T. Dendritic Ag@Cu bimetallic interface for enhanced electrochemical responses on glucose and hydrogen peroxide. *Sensors Actuators, B Chem.* 232, 375-382 (2016) doi:10.1016/j.snb.2016.03.129.

[23] Guler, M., Turkoglu, V., Bulut, A. & Zahmakiran, M. Electrochemical sensing of hydrogen peroxide using Pd@Ag bimetallic nanoparticles decorated functionalized reduced graphene oxide. *Electrochim. Acta* 263, 118-126 (2018) doi:10.1016/j.electacta.2018.01.048.

[24] Hassan, M., Jiang, Y., Bo, X. & Zhou, M. Sensitive nonenzymatic detection of hydrogen peroxide at nitrogen-doped graphene supported-CoFe nanoparticles. *Talanta* 188, 339-348 (2018) doi:10.1016/j.talanta.2018.06.003.

[25] Liu, W. *et al.* Pt and Au bimetallic and monometallic nanostructured amperometric sensors for direct detection of hydrogen peroxide: Influences of bimetallic effect and silica support. *Sensors Actuators, B Chem.* 255, 1325-1334 (2018) doi:10.1016/j.snb.2017.08.123.

[26] Chen, T. *et al.* Controlled synthesis of Au@Pd core-shell nanocomposites and their application for electrochemical sensing of

hydroquinone. *Talanta* 198, 78-85 (2019)
doi:10.1016/j.talanta.2019.01.094.

[27] Eteya, M. M., Rounaghi, G. H. & Deiminiat, B. Fabrication of a new electrochemical sensor based on Au–Pt bimetallic nanoparticles decorated multi-walled carbon nanotubes for determination of diclofenac. *Microchem. J.* 144, 254-260 (2019) doi:10.1016/j.microc.2018.09.009.

[28] Wang, K., Wu, C., Wang, F., Liao, M. & Jiang, G. Bimetallic nanoparticles decorated hollow nanoporous carbon framework as nanozyme biosensor for highly sensitive electrochemical sensing of uric acid. *Biosens. Bioelectron.* 150, 111869(2020)
doi:10.1016/j.bios.2019.111869.

[29] Gao, X. *et al.* Core-shell gold-nickel nanostructures as highly selective and stable nonenzymatic glucose sensor for fermentation process. *Sci. Rep.* 10, 1365(2020) doi:10.1038/s41598-020-58403-x.

[30] Jiao, J. *et al.* An ultrasensitive non-enzymatic sensor for quantitation of anti-cancer substance chicoric acid based on bimetallic nanoalloy with polyetherimide-capped reduced graphene oxide. *Nanomaterials* 10, 499 (2020) doi:10.3390/nano10030499.

[31] Pifferi, V. *et al.* Au-based catalysts: Electrochemical characterization for structural insights. *Molecules* 21, 261 (2016)
doi:10.3390/molecules21030261.

[32] Sárkány, A., Geszti, O. & Sáfrán, G. Preparation of Pdshell-Aucore/SiO₂ catalyst and catalytic activity for acetylene hydrogenation. *Appl. Catal. A Gen.* 350, 157-163 (2008)
doi:10.1016/j.apcata.2008.08.012.

[33] Wang, R. *et al.* Selective oxidative esterification of alcohols over Au-Pd/graphene. *Mol. Catal.* 484, 110687 (2019)
doi:10.1016/j.mcat.2019.110687.

[34] Thanh, T. D., Balamurugan, J., Lee, S. H., Kim, N. H. & Lee, J. H. Novel porous gold-palladium nanoalloy network-supported graphene as

an advanced catalyst for non-enzymatic hydrogen peroxide sensing. *Biosens. Bioelectron.* 85, 669-678 (2016) doi:10.1016/j.bios.2016.05.075.

[35] Li, J., Zheng, Y., Zeng, J. & Xia, Y. Controlling the size and morphology of Au@Pd core-shell nanocrystals by manipulating the kinetics of seeded growth. *Chem. - A Eur. J.* 18, 8150-8156 (2012) doi:10.1002/chem.201200823.

[36] Larios-Rodríguez, E. A., Castellón-Barraza, F. F., Borbón-González, D. J., Herrera-Urbina, R. & Posada-Amarillas, A. Green-Chemical Synthesis of Monodisperse Au, Pd and Bimetallic (Core-Shell) Au-Pd, Pd-Au Nanoparticles. *Adv. Sci. Eng. Med.* 5, 1-8 (2013) doi:10.1166/ asem.2013.1354.

[37] Turkevich, J., Stevenson, P. C. & Hillier, J. A study of the nucleation and growth processes in the synthesis of colloidal gold. *Discussions of the Faraday Society* 11, 55-75 (1951) doi:10.1039/DF9511100055.

[38] Frens, G. Controlled Nucleation for the Regulation of the Particle Size in Monodisperse Gold Suspensions. *Nat. Phys. Sci.* 241, 20-22 (1973) doi:10.1038/physci241020a0.

[39] Tyagi, H., Kushwaha, A., Kumar, A. & Aslam, M. A Facile pH Controlled Citrate-Based Reduction Method for Gold Nanoparticle Synthesis at Room Temperature. *Nanoscale Res. Lett.* 11, 362 (2016) doi:10.1186/s11671-016-1576-5.

[40] Bruno, L. *et al.* Localized energy band bending in zno nanorods decorated with au nanoparticles. *Nanomaterials* 11, 2718 (2021) doi:10.3390/nano11102718.

[41] Urso, M. *et al.* Enhanced sensitivity in non-enzymatic glucose detection by improved growth kinetics of Ni-based nanostructures. *Nanotechnology* 29, 165601 (2018) doi:10.1088/1361-6528/aaacb6.

[42] Iwu, K. O., Lombardo, A., Sanz, R., Scirè, S. & Mirabella, S. Facile synthesis of Ni nanofoam for flexible and low-cost non-enzymatic glucose sensing. *Sensors Actuators, B Chem.* 224, 764-771 (2016) doi:10.1016/j.snb.2015.10.109.

[43] Urso, M. *et al.* Ni(OH)₂@Ni core-shell nanochains as low-cost high-rate performance electrode for energy storage applications. *Sci. Rep.* 9, 7736 (2019) doi:10.1038/s41598-019-44285-1.

[44] Thompson, M. Xrump. Available online: www.genplot.com.

[45] DigitalMicrograph®. Available online: <https://www.gatan.com/products/tem-analysis/gatan-microscopy-suite-software>.

[46] COMSOL Multiphysics® v. 5.3. COMSOL AB, Stockholm, Sweden. Available online: <http://www.comsol.com>.

[47] Dutta, S. *et al.* Facile Synthesis of Bimetallic Au-Pt, Pd-Pt, and Au-Pd Nanostructures: Enhanced Catalytic Performance of Pd-Pt Analogue towards Fuel Cell Application and Electrochemical Sensing. *Electrochim. Acta* 180, 1075-1084 (2015) doi:10.1016/j.electacta.2015.09.062.

[48] Alford, T. L., Feldman, L. C. & Mayer, J. W. *Fundamentals of nanoscale film analysis* (Springer, 2007) doi:10.1007/978-0-387-29261-8.

[49] Medway, S. L., Lucas, C. A., Kowal, A., Nichols, R. J. & Johnson, D. In situ studies of the oxidation of nickel electrodes in alkaline solution. *J. Electroanal. Chem.* 587, 172-181 (2006) doi:10.1016/j.jelechem.2005.11.013.

[50] Toghiani, K. E. & Compton, R. G. Electrochemical Non-Enzymatic Glucose Sensors: A Perspective and an Evaluation. *Int. J. Electrochem. Sci.* 5, 1246-1301 (2010).

[51] Petralia, S., Mirabella, S., Strano, V. & Conoci, S. A Miniaturized Electrochemical System Based on Nickel Oxide Species for Glucose Sensing Applications. *Bionanoscience* 7, 58-63 (2017) doi:10.1007/s12668-017-0399-x.

[52] Chen, K. J. *et al.* Bimetallic PtM (M=Pd, Ir) nanoparticle decorated multi-walled carbon nanotube enzyme-free, mediator-less amperometric

sensor for H₂O₂. *Biosens. Bioelectron.* 33, 120-127 (2012) doi:10.1016/j.bios.2011.12.037.

[53] Chen, K. J. *et al.* Fabrication and application of amperometric glucose biosensor based on a novel PtPd bimetallic nanoparticle decorated multi-walled carbon nanotube catalyst. *Biosens. Bioelectron.* 33, 75-81 (2012) doi:10.1016/j.bios.2011.12.020.

[54] Wang, J. *et al.* Highly sensitive electrochemical determination of Sunset Yellow based on the ultrafine Au-Pd and reduced graphene oxide nanocomposites. *J. Colloid Interface Sci.* 481, 229-235 (2016) doi:10.1016/j.jcis.2016.07.061.

[55] Randles, J. E. B. Kinetics of rapid electrode reactions. *Faraday Discuss.* 1, 11-19 (1947) doi:10.1039/DF9470100011.

[56] Han, T., Zhang, Y., Xu, J., Dong, J. & Liu, C. C. Monodisperse AuM (M = Pd, Rh, Pt) bimetallic nanocrystals for enhanced electrochemical detection of H₂O₂. *Sensors Actuators, B Chem.* 207, 404-412 (2015) doi:10.1016/j.snb.2014.10.028.

[57] Manivannan, S. & Ramaraj, R. Core-shell Au/Ag nanoparticles embedded in silicate sol-gel network for sensor application towards hydrogen peroxide. *J. Chem. Sci.* 121, 735-743 (2009) doi:10.1007/s12039-009-0088-6.

[58] Xiao, F., Zhao, F., Zhang, Y., Guo, G. & Zeng, B. Ultrasonic electrodeposition of gold - platinum alloy nanoparticles on ionic liquid - chitosan composite film and their application in fabricating nonenzyme hydrogen peroxide sensors. *J. Phys. Chem. C* 113, 849-855 (2009) iwydoi:10.1021/jp808162g.

[59] Lee, W. C. *et al.* Comparison of enzymatic and non-enzymatic glucose sensors based on hierarchical Au-Ni alloy with conductive polymer. *Biosens. Bioelectron.* 130, 48-54 (2019) doi:10.1016/j.bios.2019.01.028.

[60] Zhang, T. *et al.* AuPt/MOF-Graphene: A synergistic catalyst with surprisingly high peroxidase-like activity and its application for H₂O₂

Detection. *Anal. Chem.* 91, 10589-10595 (2019)
doi:10.1021/acs.analchem.9b01715.

[61] Hall, D. S., Lockwood, D. J., Bock, C. & MacDougall, B. R. Nickel hydroxides and related materials: A review of their structures, synthesis and properties. *Proceedings of the Royal Society A: Mathematical, Physical and Engineering Sciences* 471, 20140792 (2015)
doi:10.1098/rspa.2014.0792.

[62] Ash, B., Nalajala, V. S., Popuri, A. K., Subbaiah, T. & Minakshi, M. Perspectives on nickel hydroxide electrodes suitable for rechargeable batteries: Electrolytic vs. chemical synthesis routes. *Nanomaterials* 10, 1878 (2020) doi:10.3390/nano10091878.

[63] Bott, A. W. Electrochemistry of Semiconductors. *Curr. Sep.* 17, 3 (1998).

[64] Beranek, R. (Photo)electrochemical methods for the determination of the band edge positions of TiO₂-based nanomaterials. *Advances in Physical Chemistry* 2011, 786759 (2011) doi:10.1155/2011/786759.

[65] Fabregat-Santiago, F., Garcia-Belmonte, G., Bisquert, J., Bogdanoff, P. & Zaban, A. Mott-Schottky Analysis of Nanoporous Semiconductor Electrodes in Dielectric State Deposited on SnO₂ Conducting Substrates. *J. Electrochem. Soc.* 150, E293-E298 (2003)
doi:10.1149/1.1568741.

[66] Hankin, A., Bedoya-Lora, F. E., Alexander, J. C., Regoutz, A. & Kelsall, G. H. Flat band potential determination: Avoiding the pitfalls. *J. Mater. Chem. A* 7, 26162 (2019) doi:10.1039/c9ta09569a.

[67] Xu, P., Milstein, T. J. & Mallouk, T. E. Flat-Band Potentials of Molecularly Thin Metal Oxide Nanosheets. *ACS Appl. Mater. Interfaces* 8, 11539-11547 (2016) doi:10.1021/acsami.6b02901.

[68] Gelderman, K., Lee, L. & Donne, S. W. Flat-band potential of a semiconductor: Using the Mott-Schottky equation. *J. Chem. Educ.* 84, 685 (2007) doi:10.1021/ed084p685.

- [69] Darowicki, K., Krakowiak, S. & Ślepski, P. Selection of measurement frequency in Mott-Schottky analysis of passive layer on nickel. in *Electrochimica Acta* 51, 2204-2208 (2006). doi:10.1016/j.electacta.2005.04.079.
- [70] Laskowski, F. A. L. *et al.* Nanoscale semiconductor/catalyst interfaces in photoelectrochemistry. *Nat. Mater.* 19, 69-76 (2020) doi:10.1038/s41563-019-0488-z.
- [71] Memming, R. *Semiconductor Electrochemistry* (Wiley, 2000) doi:10.1002/9783527613069.
- [72] Compton, R. G. & Banks, C. E. *Understanding voltammetry, 2nd edition. Understanding Voltammetry, 2nd Edition* (World Scientific, 2010). doi:10.1142/P726.
- [73] Bard, A. *et al. Electrochemical Methods: Fundamentals and Applications* (Wiley, 2001).
- [74] Gerischer, H. & Ekardt, W. Fermi levels in electrolytes and the absolute scale of redox potentials. *Appl. Phys. Lett.* (1983) doi:10.1063/1.94356.
- [75] Gerischer, H. The impact of semiconductors on the concepts of electrochemistry. *Electrochimica Acta* (1990) doi:10.1016/0013-4686(90)87067-C.
- [76] Marcus, R. A. On the theory of oxidation-reduction reactions involving electron transfer. I. *J. Chem. Phys.* (1956) doi:10.1063/1.1742723.
- [77] Marcus, R. A. On the theory of oxidation-reduction reactions involving electron transfer. II. Applications to data on the rates of isotopic exchange reactions. *J. Chem. Phys.* (1957) doi:10.1063/1.1743423.
- [78] Marcus, R. A. On the theory of oxidation-reduction reactions involving electron transfer. III. applications to data on the rates of organic redox reactions. *J. Chem. Phys.* (1957) doi:10.1063/1.1743424.
- [79] Marcus, R. a. Exchange Reactions and Electron Transfer Reactions Including Isotopic Exchange Theory of Oxidation-Reduction Reactions Involving Electron Transfer. *Discuss. Faraday Soc.* (1960).

[80] Marcus, R. A. On the theory of oxidation-reduction reactions involving electron transfer. V. Comparison and properties of electrochemical and chemical rate constants. *Journal of Physical Chemistry* (1963) doi:10.1021/j100798a033.

[81] Marcus, R. A. On the Theory of Electron-Transfer Reactions. VI. Unified Treatment for Homogeneous and Electrode Reactions. *J. Chem. Phys.* (1965) doi:10.1063/1.1696792.

[82] Archana, V., Xia, Y., Fang, R. & Gnana Kumar, G. Hierarchical CuO/NiO-Carbon Nanocomposite Derived from Metal Organic Framework on Cello Tape for the Flexible and High Performance Nonenzymatic Electrochemical Glucose Sensors. *ACS Sustain. Chem. Eng.* (2019) doi:10.1021/acssuschemeng.8b05980.

[83] Cui, H. F. *et al.* Selective and sensitive electrochemical detection of glucose in neutral solution using platinum-lead alloy nanoparticle/carbon nanotube nanocomposites. *Anal. Chim. Acta* (2007) doi:10.1016/j.aca.2007.05.047.

[84] Long, L., Liu, X., Chen, L., Li, D. & Jia, J. A hollow CuO_x/NiO_y nanocomposite for amperometric and non-enzymatic sensing of glucose and hydrogen peroxide. *Microchim. Acta* (2019) doi:10.1007/s00604-018-3183-x.

[85] Mei, H. *et al.* A nanocomposite consisting of gold nanobipyramids and multiwalled carbon nanotubes for amperometric nonenzymatic sensing of glucose and hydrogen peroxide. *Microchim. Acta* (2019) doi:10.1007/s00604-019-3272-5.

[86] Zhu, Y. *et al.* A nickel-cobalt bimetallic phosphide nanocage as an efficient electrocatalyst for nonenzymatic sensing of glucose. *Microchim. Acta* (2020) doi:10.1007/s00604-019-4073-6.

[87] Janyasupab, M., Liu, C. W., Zhang, Y., Wang, K. W. & Liu, C. C. Bimetallic Pt-M (M = Cu, Ni, Pd, and Rh) nanoporous for H₂O₂ based amperometric biosensors. *Sensors Actuators, B Chem.* (2013) doi:10.1016/j.snb.2012.09.099.

[88] Li, Z. *et al.* Electrostatic Self-Assembled Bracelet-Like Au@Pt Nanoparticles: An Efficient Electrocatalyst for Highly Sensitive Non-Enzymatic Hydrogen Peroxide Sensing. *ChemElectroChem* (2020) doi:10.1002/celec.202000019.

[89] Li, W., Kuai, L., Qin, Q. & Geng, B. Ag-Au bimetallic nanostructures: Co-reduction synthesis and their component-dependent performance for enzyme-free H₂O₂ sensing. *J. Mater. Chem. A* (2013) doi:10.1039/c3ta00106g.

[90] Zhao, L. *et al.* Green Synthesis of Ag–Au Bimetallic Nanoparticles with Alginate for Sensitive Detection of H₂O₂. *Catal. Letters* (2018) doi:10.1007/s10562-018-2522-1.

Conclusions

The aim of this thesis was the controlled synthesis of mono- and bi-metallic nanoparticles for application in sensing and energy production. In particular, the chemical reduction at room temperature of Au, Pd, Pt, and Au@Pd nanoparticles was carefully investigated and controlled.

The main advantage of these technique is that it is not necessary to reach high temperatures (the process takes place at room temperature). Furthermore, the number of reactants is reduced to two, the metal precursor and the reducing agent (trisodium citrate and ascorbic acid). The variation in concentration of one of these two parameters (dissolved in aqueous solution) has a strong impact on the average size of the nanoparticles and, indirectly, on their physical and catalytic properties.

The effect nanoparticle decoration of metal oxide semiconductors (NiO, ZnO) was evaluated in terms of energy band modification, catalytic effect in sensing and energy production (water splitting):

- The decoration of ZnO nanorods by means of Au nanoparticles was experimentally investigated and modelled in terms of energy band bending. ZnO nanorods were synthesized by chemical bath deposition. Decoration with Au nanoparticles was achieved by immersion in a colloidal solution obtained through the modified Turkevich method. It induced a 10 times reduction in free electrons below the surface of ZnO, together with a decrease in UV luminescence and an increase in visible-UV intensity ratio. The effect of decoration was modelled with a nano-Schottky junction at ZnO surface below the Au nanoparticle with a Multiphysics approach. An extensive electric field with a specific halo effect formed beneath the metal–semiconductor interface. ZnO nanorod decoration with Au nanoparticles was shown to be a versatile

method to tailor the electronic properties at the semiconductor surface.

- A low-cost chemical methodology is reported to obtain large amount of microflowers made of interconnected NiO nanowalls wisely decorated with ultralow amounts of Pt nanoparticles. These decorated micro- flowers, dispersed onto graphene paper by drop casting, build a high performance HER electrode. The effect of Pt decoration has been modelled through energy band bending supported by electrochemical analyses. A full cell for alkaline electrochemical water splitting has been built, composed of Pt decorated NiO microflowers as cathode and bare NiO microflowers as anode, showing a low potential of 1.57 V to afford a current density of 10 mA cm² and a good long-term stability.
- Au, Pd and Au@Pd (core@shell) nanoparticles were used to decorate Ni-based nanostructured electrodes. Decorated electrodes show higher redox currents than bare ones and a shift in redox peaks, which can be ascribed to a more efficient electron transport and improved catalytic properties. These effects were satisfactorily modeled employing a nano Schottky junction at the nanoparticle-semiconductor interface, pointing out large energy band bending, space charge region and local electric field in bimetallic decoration. Sensing test of glucose and H₂O₂ by decorated Ni oxide electrodes were performed to consolidate our model. The presence of bimetallic nanoparticles enhances enormously the electrochemical performances of the material in terms of sensitivity, catalytic activity, and electrical transport. The modification of energy band diagram in semiconductor is analyzed and discussed also in terms of electron transfer during redox reactions.

Through the studies conducted and described in the previous chapters it was possible to verify up to what extent decoration with mono- or bi-metallic nanoparticles can affect physical and chemical properties of supporting nanostructured semiconductors. In all cases an enhancement of the electrical and catalytic properties was observed pointing out how decoration can be an effective method for locally modifying the position of the energy bands of the supporting semiconductor by minimizing the use of critical raw material (Au, Pd, Pt, ...).

Appendix A

Mott-Schottky Analysis

We need to consider what happens at the (idealized) interface between a semiconductor electrode and an electrolyte solution.

In order for the two phases to be in equilibrium, their electrochemical potential must be the same. The electrochemical potential of the solution is determined by the redox potential of the electrolyte solution, and the redox potential of the semiconductor is determined by the Fermi level [1-2]. If the redox potential of the solution and the Fermi level have not the same energy, a movement of charge between the semiconductor and the solution is required in order to equilibrate the two phases. The excess charge that is now located on the semiconductor does not lie at the surface, as it would for a metallic electrode, but extends into the electrode. This region is referred to as the space charge region and has an associated electrical field.

For an *n*-type semiconductor electrode at open circuit, the Fermi level is higher than the redox potential of the electrolyte, and hence electrons will be transferred from the electrode into the solution. Therefore, there is a positive charge associated with the space charge region, and this is reflected in an upward bending of the band edges (Figure A1(a)).

For a *p*-type semiconductor, the Fermi level is lower than the redox potential, and hence electrons must transfer from the solution to the electrode to attain equilibrium. This generates a negative charge in the space charge region, which causes a downward bending in the band edges (Figure A1(b)).

The band edges in the interior of the semiconductor vary with the applied potential in the same way as the Fermi level. However, the energies of the band edges at the interface are not affected by changes in the applied

potential. Therefore, the change in the energies of the band edges on going from the interior of the semiconductor to the interface, and hence the magnitude and direction of band bending, varies with the applied potential. There are three different situations to be considered [1]:

- a) At a certain potential, the Fermi energy lies at the same energy as the solution redox potential Figure A1(c,d). There is no net transfer of charge, and hence there is no band bending. This potential is therefore referred to as the flat-band potential, E_{FB} .
- b) Depletion regions arise at potentials positive of the flat-band potential for an n -type semiconductor and at potentials negative of the flat-band potential for a p -type semiconductor Figure A1(a, f).
- c) At potentials negative of the flat-band potential for an n -type semiconductor, there is now an excess of the majority charge carrier (electrons) in this space charge region, which is referred to as an accumulation region (Figure A1(e)). An accumulation region arises in a p -type semiconductor at potentials more positive than the flat-band potential (Figure A1(b)).

Using the model of a parallel-plate capacitor, the Mott-Schottky relation can be obtained from [1-4]:

$$\frac{1}{C_{SC}^2} = \frac{2}{\epsilon_0 \epsilon_r e N_D} \left(E - E_{FB} - \frac{kT}{e} \right) \quad (A1)$$

The interface double layer capacitances C_{SC} and C_H (representing the capacitance of the space-charge layer, the capacitance of the Helmholtz double layer at the semiconductor-electrolyte interface) can be treated as two capacitors connected in series. The overall capacitance C is then given by

$$\frac{1}{C} = \frac{1}{C_{SC}} + \frac{1}{C_H} \quad (A2)$$

It can be assumed that the width of the space-charge layer is much larger than the width of the Helmholtz layer and $C_{SC} \approx C$.

From the resulting Mott-Schottky plot the flat band potential E_{FB} and the donor density N_D can be now obtained as the intercept with the x -axis and from the slope of the linear part. In particular:

$$N_D = \frac{2}{\epsilon_0 \epsilon_r e (dC_{SC}^{-2}/dE)} \quad (A3)$$

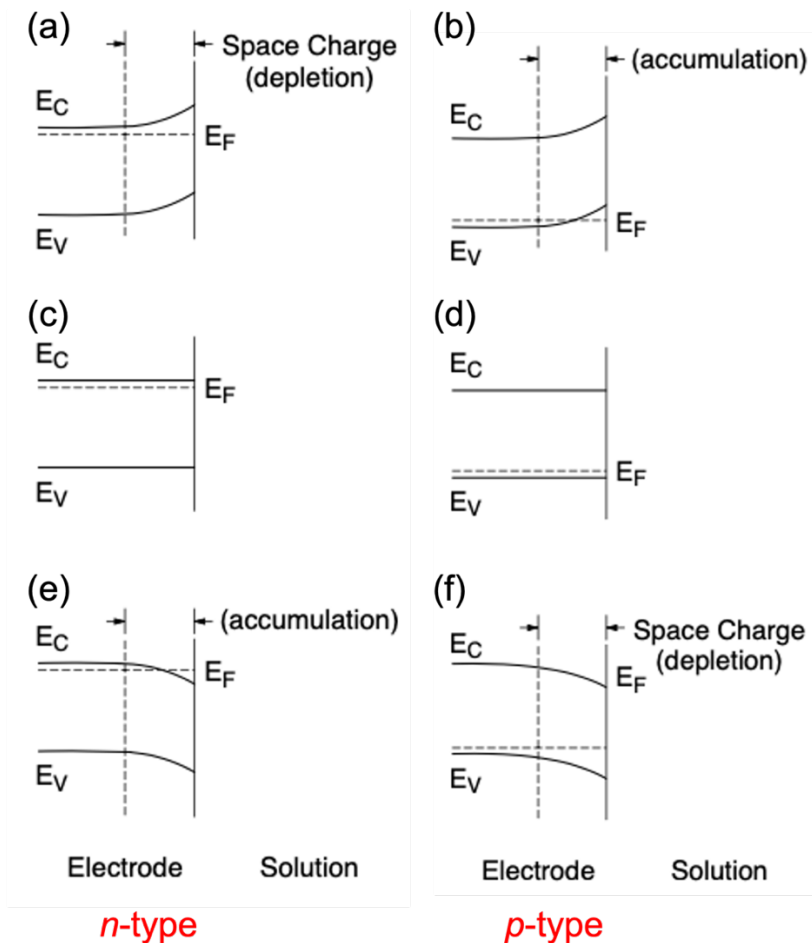


Figure A1: Effect of varying the applied potential (E) on the band edges in the interior of a p-type semiconductor. (a,b) $E > E_{fb}$, (c,d) $E = E_{FB}$, (d,e) $E < E_{FB}$.

It should be noted that the theory just described was developed in the case of flat semiconductors. In the case of nanostructured semiconductors, a careful evaluation of the structure and electrical properties should be carried out. In particular, the effect of the structure and morphology of the material on the generated electric field is of fundamental importance [10]. Despite this, by comparing the same nanostructure under different conditions (for example following decoration with metal NPs), it is possible to have a first indication on the changes in the energy levels of the material following the interaction of the semiconductor with an electrolyte.

References

- [1] A.W. Bott, *Electrochemistry of Electrochemistry of Semiconductors*, Curr. Sep. (1998).
- [2] R. Beranek, (Photo)electrochemical methods for the determination of the band edge positions of TiO₂-based nanomaterials, *Adv. Phys. Chem.* (2011). <https://doi.org/10.1155/2011/786759>.
- [3] F. Fabregat-Santiago, G. Garcia-Belmonte, J. Bisquert, P. Bogdanoff, A. Zaban, Mott-Schottky Analysis of Nanoporous Semiconductor Electrodes in Dielectric State Deposited on SnO₂F Conducting Substrates, *J. Electrochem. Soc.* (2003). <https://doi.org/10.1149/1.1568741>.
- [4] A. Hankin, F.E. Bedoya-Lora, J.C. Alexander, A. Regoutz, G.H. Kelsall, Flat band potential determination: Avoiding the pitfalls, *J. Mater. Chem. A.* (2019). <https://doi.org/10.1039/c9ta09569a>.
- [5] Y. Gao, Z.L. Wang, Equilibrium potential of free charge carriers in a bent piezoelectric semiconductive nanowire, *Nano Lett.* (2009). <https://doi.org/10.1021/nl803547f>.
- [6] C.F. Klingshirn, ZnO: Material, physics and applications, *ChemPhysChem.* (2007). <https://doi.org/10.1002/cphc.200700002>.
- [7] C. Jagadish, S. Pearton, Zinc Oxide Bulk, Thin Films and Nanostructures, (2006). <https://doi.org/10.1016/B978-0-08-044722-3.X5000-3>.
- [8] S.M. Sze, K.K. Ng, *Physics of Semiconductor Devices*, (2006). <https://doi.org/10.1002/0470068329>.
- [9] M. Henry and H. Fanet, *Physique des semiconducteurs et des composants électroniques.* (2019).
- [10] Mora-Seró, I., Fabregat-Santiago, F., Denier, B., Bisquert, J., Tena-Zaera, R., Elias, J., & Lévy-Clément, C. Determination of carrier density of ZnO nanowires by electrochemical techniques. *Applied Physics Letters* (2006). doi:10.1063/1.2390667

Appendix B

Synthesis of Ni oxide nanostructures

In this appendix, a brief description of the synthesis procedures of Ni-based nanostructured used in our works is presented. In particular, we will focus our attention on Ni nanofoam and NiO microflowers.

Ni nanofoam (NF) (Figure 2.5(a-b)) is obtained by a two-step synthesis.

1. First, a substrate (conductive or not) is immersed in a solution, through a bain-marie configuration containing the chemical precursors. Solution for CBD was prepared by mixing 0.42 M $\text{NiSO}_4 \cdot 6\text{H}_2\text{O}$ (Merck, Darmstadt, Germany, 98%), 0.07 M $\text{K}_2\text{S}_2\text{O}_8$ (Alfa Aesar, Kandel, Germany 97%) and 3.5 wt% ammonia (Merck, Darmstadt, Germany, 30–33 wt% NH_3 in H_2O). This process is known as Chemical Bath Deposition. The bath temperature is kept constant at 50 °C for 20 minutes. After their extraction, the substrates show a uniform dark film made of a $\text{Ni}(\text{OH})_2$ nanowalls structure with thin interconnected sheets perpendicular to substrate [1-3].
2. Finally, a reducing thermal process at 350°C (for 1 hour in Ar and 1h in Forming Gas, FG) leads to a structural and chemical transformation in which nanowalls are converted into chain-like clusters of metallic 20 nm large Ni NPs (Figure 4.2(b)) [4].

Ni NF is characterized by an open nanoporous structure formed by interconnected sheets, each with a thickness of 10-20 nm. The nanostructured film is about 0.5 μm tall on the substrate and shows porous features, with open volume as large as 200-400 nm. Further details on Chapter 4.

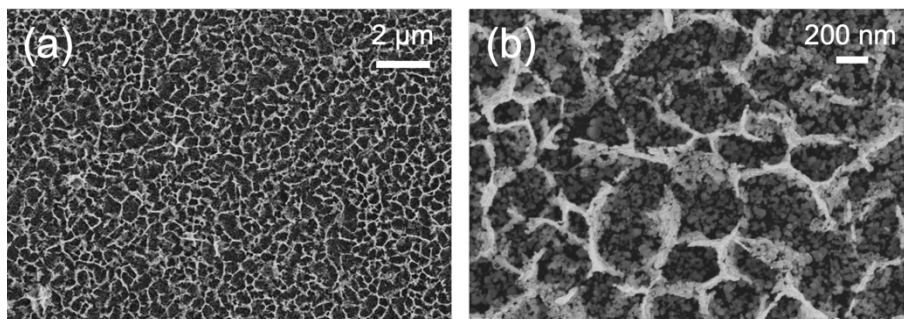


Figure A1: (a) Low- and (b) High-magnification SEM images of Ni NF.

The same solution used for the synthesis of Ni NF, can be used to extract Ni-based nanostructures (microflowers, μ Fs) resulted from the homogeneous nucleation of reagents. NiO microflowers (Figure 2.5(c-d)) are obtained starting from the previously described CBD method through the following steps [5,6]:

1. After the extraction of the substrates from the chemical bath, the solution was centrifugated and washed several times with a mixture of deionized water and ethanol (1:1) until a dark blue precipitate (made of $\text{Ni}(\text{OH})_2$ μ Fs) are totally separated from solution.
2. The $\text{Ni}(\text{OH})_2$ μ Fs were then dried in air in an oven for 24 hours and then annealed at 350 °C for 60 min in Ar leading to the conversion of $\text{Ni}(\text{OH})_2$ into NiO [1,7].
3. A μ Fs solution was then prepared by mixing the obtained powder with deionized water and ethanol (15 mg of μ Fs in 8 mL 1:1 of water and ethanol) followed by sonication for 15 minutes at room temperature in order to avoid nanostructures agglomeration.

Each NiO μ F appears as a porous sphere (with a diameter spanning in the 0.8-1.2 μm range), made of 2D interconnected nanosheets (with thickness of 20 nm, Figure 2.5(d)) pointing toward a common center. A detailed characterization of NiO μ Fs is given in Chapter 5.

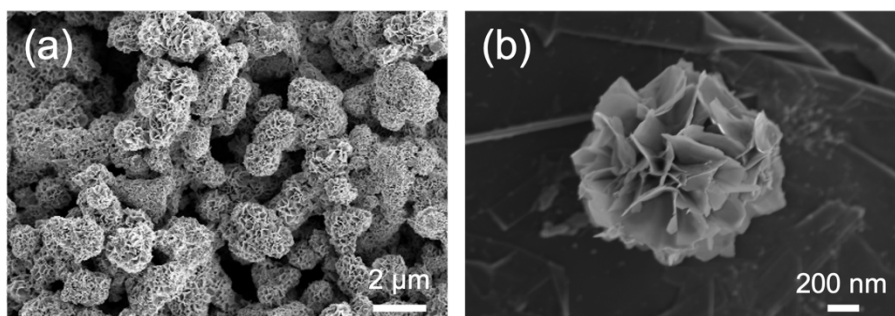


Figure A2: (a) Low- and (b) High-magnification SEM images of NiO μ Fs.

References

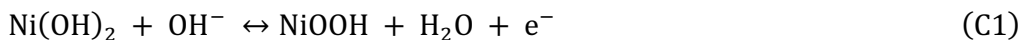
- [1] Iwu, K.O.; Lombardo, A.; Sanz, R.; Scirè, S.; Mirabella, S. Facile synthesis of Ni nanofoam for flexible and low-cost non-enzymatic glucose sensing. *Sensors Actuators, B Chem.* 2016, doi:10.1016/j.snb.2015.10.109.
- [2] Bruno, L.; Urso, M.; Shacham-Diamand, Y.; Priolo, F.; Mirabella, S. Role of Substrate in Au Nanoparticle Decoration by Electroless Deposition. *Nanomaterials* 2020. <https://doi.org/10.3390/nano10112180>.
- [3] Bruno, L.; Scuderi, M.; Priolo, F.; Falciola, L.; Mirabella, S. Enlightening the Bimetallic Effect of Au@Pd Nanoparticles on Ni Oxide Nanostructures with Enhanced Catalytic Activity. *Scientific Reports* 2022, *accepted for publication*.
- [4] Urso, M.; Torrisi, G.; Boninelli, S.; Bongiorno, C.; Priolo, F.; Mirabella, S. Ni(OH)₂@Ni core-shell nanochains as low-cost high-rate performance electrode for energy storage applications. *Sci. Rep.* 2019, doi:10.1038/s41598-019-44285-1.
- [5] Bruno, L.; Battiato, S.; Scuderi, M.; Priolo, Terrasi, A.; Mirabella, S. Physical Insights into Alkaline overall water splitting with NiO Microflowers Electrodes with ultra-low amount of Pt catalyst. *Int. J. of Hydr. En.* 2022, doi:10.1016/j.ijhydene.2022.08.005.
- [6] Bruno, L.; Scuderi, M.; Priolo, F.; Mirabella, S. Enhanced Electrocatalytic Activity of low-cost NiO Microflowers on Graphene Paper for Oxygen Evolution Reaction. *Sustain. Energy Fuels* 2022, doi: 10.1039/D2SE00829G.
- [7] Urso, M. *et al.* Enhanced sensitivity in non-enzymatic glucose detection by improved growth kinetics of Ni-based nanostructures. *Nanotechnology* 29, 165601 (2018) doi:10.1088/1361-6528/aaac6.

This Page Intentionally Left Blank

Appendix C

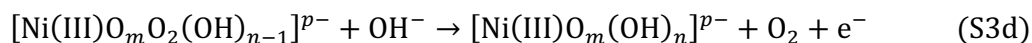
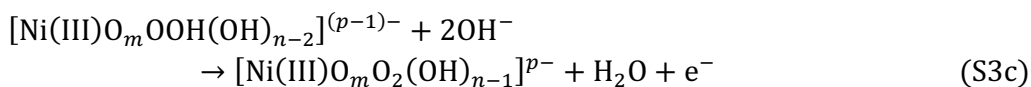
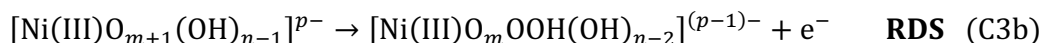
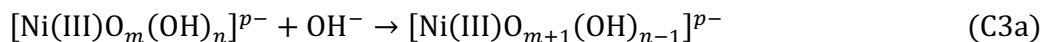
OER Mechanism at Nickel-based Electrodes

Nickel-based materials are considered some of the most promising transition metal catalysts for the Oxygen Evolution Reaction (OER) in alkaline media [1,2]. Subsequently to the immersion of NiO electrodes in an aqueous solution a layer of Ni(OH)₂ is spontaneously formed at open circuit potential². During the oxidation/reduction cycling the Ni hydroxide layer grows after the conversion of Ni(II) to Ni(III) and the formation of NiOOH during the charge step and the re-formation of Ni(OH)₂ during the discharge step of the cyclic voltammetry [3]. The charge/discharge process of the NiO/ Ni(OH)₂ electrode can be described as follows [4]:



Upon the growth of the Ni(OH)₂ layer, a significant increase in the OER activity is generally observed for a hydrous nickel oxide electrode [5]. Besides the formation of a stable and optimal Ni(OH)₂ layer and the formation of different charge/discharge phases [6] after potential cycling, an increase of roughness and of the number of electrochemically active sites on surface is observed [1].

In terms of a mechanistic analysis of the OER, the major difficulty is represented by the fact that the OER is a complex process involving the transfer of four electrons. Since electrons are transferred one by one, the process will be multistep [7]. Among different proposed mechanisms present in literature, Lyons *et al.* [2,7,8] suggested a mechanistic pathway which involves intermediate species in the Ni(III) valence state. For the case of anodic oxide covered Ni anodes such a pathway might be written as follows [9]:



According to this mechanism the rate determining step (RDS) for the OER is represented by the formation of a superoxy-(OOH) species by the addition of an OH^- ion on top of an adsorbed oxygen atom with a Tafel slope of around 40 mV dec^{-1} .

References

- [1] E. Fabbri, A. Habereeder, K. Waltar, R. Kötz and T. J. Schmidt, *Catal. Sci. Technol.*, 2014, DOI:10.1039/c4cy00669k.
- [2] M. E. G. Lyons and M. P. Brandon, *Int. J. Electrochem. Sci.*, 2008, 3, 1425-1462.
- [3] D. S. Hall, D. J. Lockwood, C. Bock and B. R. MacDougall, *Proc. R. Soc. A Math. Phys. Eng. Sci.*, 2015, DOI:10.1098/rspa.2014.0792.
- [4] S. Cosentino, M. Urso, G. Torrisi, S. Battiato, F. Priolo, A. Terrasi and S. Mirabella, *Mater. Adv.*, 2020, DOI:10.1039/d0ma00467g.
- [5] I. J. Godwin and M. E. G. Lyons, *Electrochem. commun.*, 2013, DOI:10.1016/j.elecom.2013.03.040.
- [6] H. Bode, K. Dehmelt and J. Witte, *Electrochim. Acta*, 1966, DOI:10.1016/0013-4686(66)80045-2.
- [7] R. L. Doyle and M. E. G. Lyons, in *Photoelectrochemical Solar Fuel Production: From Basic Principles to Advanced Devices*, 2016.
- [8] R. L. Doyle, I. J. Godwin, M. P. Brandon and M. E. G. Lyons, *Phys. Chem. Chem. Phys.*, 2013, DOI:10.1039/c3cp51213d.
- [9] M. E. G. Lyons and M. P. Brandon, *J. Electroanal. Chem.*, 2010, DOI:10.1016/j.jelechem.2009.11.024.

This Page Intentionally Left Blank

Curriculum Vitae

Luca Bruno was born in Catania (Italy) on June 15th, 1994.

Education

PhD in Materials Science & Nanotechnologies

University of Catania (October 2019 - October 2022)

Thesis title: **Metal nanoparticle decoration of nanostructures**

Supervisors: Prof. F. Priolo, Prof. S. Mirabella

2019 **Master Degree in Physics** [110/110] cum laude

University of Catania

Thesis title: **Synthesis and decoration of Nickel Oxide nanostructures for sensing applications**

Supervisors: Prof. F. Priolo, Prof. S. Mirabella

2017 **Bachelor Degree in Physics** [110/110]

University of Catania

Thesis title: **L'effetto Hall quantistico nel grafene**

Supervisors: Prof. G.G.N. Angilella

Collaborations

- CNR-IMM, Catania, Italy
- University of Catania, Department of Chemical Sciences, Catania, Italy
- University of Milan, Department of Chemistry, Italy
- Tel Aviv University, Department of Physical Electronics, Tel Aviv, Israel

Oral presentations

- 1. EMRS Spring Meeting 2021, May 31-June 3.**
L. Bruno, V. Strano, G. Franzò, F. Priolo, S. Mirabella.
Electron energy band modification by Au nanoparticles decoration of ZnO nanorods.
- 2. EMRS Fall Meeting 2021, May 31-June 3.**
L. Bruno, V. Strano, M. Scuderi, G. Franzò, F. Priolo, S. Mirabella.
Effect on radiative emission mechanism of surface modification of ZnO nanorods through Au nanoparticle decoration.
- 3. EMRS Fall Meeting 2021, September 20-23.**
L. Bruno, M. Scuderi, F. Priolo, S. Mirabella.
AuPd nanoparticles synthesis and decoration of Ni-based nanostructures for electrochemical applications.
- 4. AIV XXV conference 2022, May 10-12**
L. Bruno, V. Strano, G. Franzò, F. Priolo, S. Mirabella.
Enhanced Electrocatalytic Intrinsic Activity of NiO Microflowers on Graphene Paper for Oxygen Evolution Reaction
- 5. EMRS Spring Meeting 2022, May 30-June 3.**
L. Bruno, V. Strano, G. Franzò, F. Priolo, S. Mirabella.
Effect on radiative emission mechanism of surface modification of ZnO nanorods through Au nanoparticle decoration.

6. EMRS Spring Meeting 2022, May 30-June 3.

L. Bruno, M. Scuderi, L. Falcicola, F. Priolo, S. Mirabella.

Enlightening the Bimetallic Effect of Au@Pd Nanoparticles on Ni Oxide nanostructured films with Enhanced Catalytic Activity

Poster presentations

1. EMRS Spring Meeting 2022, May 30-June 3.

L. Bruno, M. Scuderi, F. Priolo, S. Mirabella.

Enhanced Electrocatalytic Intrinsic Activity of NiO Microflowers on Graphene Paper for Oxygen Evolution Reaction

Schools

1. Aldo Armigliato" Scanning Electron Microscopy School in Materials Science

CNR-IMM Bologna

9-13 November 2020

2. IEEE CAS Seasonal school - "Technology and Agribusiness: how technology is impacting agribusiness"

online

16-20 November 2020

List of publications

This thesis is based on the following publications:

1. Role of substrate in Au nanoparticle decoration by electroless deposition

Bruno, L., Urso, M., Shacham-Diamand, Y., Priolo, F., Mirabella, S.
Nanomaterials, 2020, 10(11), pp. 1–12, 2180
DOI: <https://doi.org/10.3390/nano10112180>

2. Localized energy band bending in ZnO nanorods decorated with Au nanoparticles

Bruno, L., Strano, V., Scuderi, M., Franzò, G., Priolo, F., Mirabella, S.
Nanomaterials, 2021, 11(10), 2718
DOI: <https://doi.org/10.3390/nano11102718>

3. Superior performances of Electroless-Deposited Ni-P films decorated with an ultralow content of Pt for Water-Splitting Reactions

Battiato, S., Bruno, L., Terrasi, A., Mirabella, S.
ACS Applied Energy Materials, 2022, 5(2), pp. 2391–2399
DOI: <https://doi.org/10.1021/acsaem.1c03880>

4. Physical insights into alkaline overall water splitting with NiO microflowers electrodes with ultra-low amount of Pt catalyst

Bruno, L., Battiato, S., Scuderi, M., Priolo, F., Terrasi, A., Mirabella, S.
International Journal of Hydrogen Energy, 2022
DOI: <https://doi.org/10.1016/j.ijhydene.2022.08.005>

5. Enhanced electrocatalytic activity of low-cost NiO microflowers on graphene paper for the oxygen evolution reaction

Bruno, L., Scuderi, M., Prolo, F., Mirabella, S.
Sustainable Energy & Fuels, 2022, 6, 4498-4505
DOI: <https://doi.org/10.1039/D2SE00829G>

6. Enlightening the Bimetallic Effect of Au@Pd Nanoparticles on Ni Oxide Nanostructures with Enhanced Catalytic Activity

Bruno, L., Scuderi, M., Prolo, F., Falciola, L., Mirabella, S.
Scientific Reports, 2023
DOI: <https://doi.org/10.1038/s41598-023-29679-6>

7. Optimized electroless deposition of NiCoP electrocatalysts for enhanced water splitting

Battiato, S., Bruno, L., Pellegino, A.L., Terrasi, A., Mirabella, S.
Catalysis today, 2022, in press
DOI: <https://doi.org/10.1016/j.cattod.2022.10.011>

8. Alkaline Overall Water Splitting with low cost and high yield Zn-based nanostars with ultra-low amount of Pt nanoparticle catalyst

Di Mari, G., Bruno, L., Spadaro, M.C., Mirabella, S., Bruno, E., Strano, V.
In preparation, 2022